Solid state precipitation of spinels in zinc oxide

A microstructure study

Jørgen Bergli

Thesis submitted for the degree of
Master in Materials, Energy and Nanotechnology
60 credits

Department of Physics
Faculty of mathematics and natural sciences

UNIVERSITY OF OSLO

Spring 2021

Solid state precipitation of spinels in zinc oxide

A microstructure study

Jørgen Bergli

Solid state precipitation of spinels in zinc oxide

http://www.duo.uio.no/

Printed: Reprosentralen, University of Oslo

Acknowledgement

I would first like to thank my supervisors Øystein Prytz, Phuong D. Nguyen and Ole Bjørn Karlsen for being outstanding teachers, role models and friends. I could not have asked for better guidance when working with this thesis. Extra thanks to Phuong for providing transmission electron microscopy training on the JEOL and operating the microscope when we had sessions on the Titan, and to Ole Bjørn for training me in the other instruments used in this work. I will really miss working with you. Øystein, you are one of the most competent persons I have met, and I am proud of having had you as my supervisor.

I would also like to thank everyone in the structure physics group at UiO, I really appreciated the inclusive and supportive environment in the group, and despite the pandemic I think we took good care of each through Zoom.

To my family and friends- Thank you for believing in me, giving me motivation and pretending to be interested when I talk too much about things as difficulties in precipitating the cubic vanadium spinel in zinc oxide (just kidding). However, a special thanks goes to my grandfather Kjell Bjørløw-Larsen.

The work with this master project has been challenging sometimes, however even more rewarding, I have learned a lot and grown as a person. Another person that literally grew during this work is my son Lorentz, he was born this summer, and by coincidence or not, more promising experimental results were obtained after his appearance. Anyhow, I would like to thank him for always making me smile. In addition has our dog, Solan, kept me company through late hours when fishing up this thesis, which has been sincerely appreciated. Last but not least, I extend the greatest gratitude for love and patience to my fiancé Silje. I would not have managed to do this without you.

Abstract

In this work we have investigated the possibility for solid state precipitation of spinel crystals in zinc oxide by separate addition of three different dopant elements. These dopant elements were iron, antimony and vanadium, and were generally introduced as oxide powders. The dopant compounds were mixed with zinc oxide using a powder synthesis route, where the annealing temperature was mostly kept below the solidus temperature in the given system. Some experiments were also performed using a single crystal of zinc oxide embedded in iron oxide and zinc oxide powders. These samples are referred to as diffusion couples.

The characterization of samples was carried out by adopting several observation methods. That is light microscopy, x-ray diffraction, scanning electron microscopy, energy dispersive spectroscopy, transmission electron microscopy and scanning transmission electron microscopy. This variety of methods enabled complementary information to be obtained.

It was found that the zinc oxide – iron system displays the most promising features in regard to precipitating spinels crystals in the zinc oxide matrix. This property is attributed to a highly temperature dependent solid solubility of iron in zinc oxide. Observations made in this system indicate that two different spinel forming mechanisms are possible. One includes a high solute iron concentration in zinc oxide and consequently precipitation during cooling of the sample. In the other route a second annealing step is added to promote the precipitation from a somewhat low iron concentration in the zinc oxide matrix. The physical appearance of the precipitates was different depending on precipitation route, however the same orientation relationship with adjacent zinc oxide grains/matrix was found for both spinel precipitates. In addition, iron rich inversion domain boundaries were seen in the single crystal. These were explored, and it was found that the spacing between the domains matched the iron concentration profile in the same region. The transition from inversion domain boundaries to spinel grains was probed to understand nucleation mechanisms for both features.

In the two other systems, antimony and vanadium doped zinc oxide, no precipitations were found. However, it was found that zinc oxide had low and more or less constant solid solubility when temperature was varied in these systems, which is assumed to be a determining factor in limiting the possibility for precipitations. Therefore, attempts were done in the zinc oxide – vanadium system to increase the solubility. However, despite interesting synthesis development, we were not able to increase the solid solubility.

In the zinc oxide – antimony system we show that etching of surfaces could be a way to render inversion domain boundaries visible in scanning electron microscopes. We also confirm the volatility of antimony by the use of x-ray diffraction and energy dispersible spectroscopy.

Contents

Chapter 1

Motivation and introduction

Solar cells can directly transform the energy contained in sunlight into electricity, and the sun provides the Earth with energy corresponding to a total of 173 000 terawatts continuously, that is more than 10 000 times the worlds energy use [1]. Thus, solar photovoltaic technologies have the potential to meet the increasing need for clean and renewable energy. However, due to costly materials and low efficiency, the numbers don't add up economically. In this thesis, we will synthesise and investigate materials that could increase the efficiency of solar cells.

Traditional solar cells are based on p- and n-doped silicon. The p-doped silicon has an excess of holes while the n-doped region has excess of electrons. This charge carrier excess is possible by introducing dopants with different number of outer-shell electrons than silicon. Silicon has four valence electrons, while n- and p-dopants have five and three outer-shell electrons, respectively. When n- and p-doped layers are connected, a recombination of charge carriers take place at the boundary. This recombination of charge carriers generates positively charged ions on the n-doped side and negatively charged ions on the positive side. As the n- and p-type layers are initially neutral, this gives rise to an electric field. The electric field increases as more ions with oppsite charge are generated on each side, and eventually becomes too strong for the charge carriers to overcome. This results in saturation of the junction and recombination comes to a standstill. However, the electric field is preserved and maintains a depletion region between the two layers.

The energy contained in sunlight can be understood as packages of energy. The packages are called photons and have an energy:

$$E = \frac{hc}{\lambda} \tag{1.1}$$

where h is Planck's constant, c is the speed of light i vacuum and λ is photon wavelength.

When photons enter the solar cell, they can create electron-hole pairs through excitations in the depletion region. The electric field inside the depletion region drives the charge carriers in opposite directions. Metal conductors connected to the surface of the solar cell provide a circuit and current can flow. However, these metal conductors will cause a shadow on the solar cell, leading to fewer photons entering the solar cell, thereby lowering the efficiency. Another problem is that the charge carriers must travel a rather long distance to find a conductor, thereby increasing the chance of recombination and loss of efficiency.

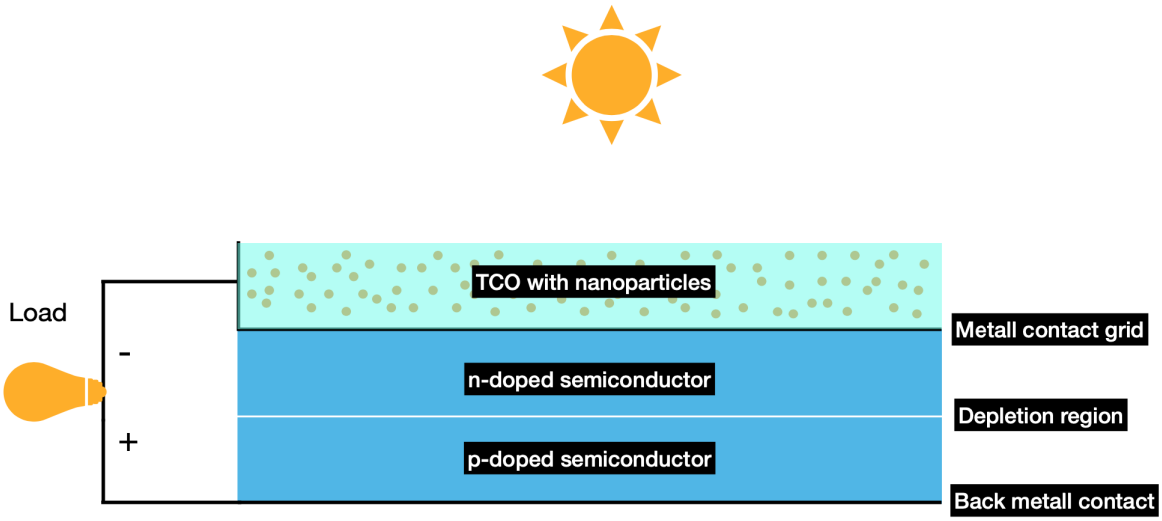

Figure 1.1: Simplified drawing of a two-layered solar cell with nanoparticles embedded in the TCO.

One solution to these problems is to use a transparent conductive oxide (TCO) as a front contact covering the entire surface of the cell. As the TCO is transparent, it does not block the incoming photons, and since it covers the entire surface, the traveling distance for the charge carriers is minimized. Zinc oxide (ZnO) is a promising TCO material as it has high transparency of light, low resistivity and a suitable bandgap [2][3].

Then, the question is raised: what if we could improve the solar cell even more?

The maximum efficiency of a single junction solar cell is theoretically given by the Shoekley-Queisser limit [4]. A significant part of the limitation is spectrum losses. This originates from the fact that one single energy bandgap (E_g) is used for absorption throughout the range of photon energies contained in the solar spectrum. If the incoming photon has too low energy, that is $E_g > \frac{hc}{\lambda}$, the photon can not be absorbed by the solar cell. In addition, when high energy photons are absorbed, that is $E_g < \frac{hc}{\lambda}$, the extra energy above the bandgap energy is lost due to relaxation to band edges. This extra energy is simply converted into heat as these "hot" charge carriers travels towards the p-n junction. For a silicon single junction solar cell, which has a bandgap of 1.1 eV, the total spectrum losses sums to about 56 % [5], clearly demonstrating a potential for improvement.

One way of exceeding the Shoekley-Queisser limit is to enable energy absorption from differnt parts of the solar spectrum by having multiple bandgaps in the solar cell, hence, splitting the solar spectrum to be absorbed. In this work we intend to introduce an energy absorbing bandgap in the TCO by creating embedded nanoparticles inside it. These particles are proposed to convert the high energy photons into electrical energy rather than dissipated heat, thus reduce the spectrum losses in the solar cell. A sketch of the system is shown in figure 1.1.

The motivation for making small (nano-)particles is that properties change as particle size approach nanoscale dimensions. One factor contributing to this is the number of surface atoms in nanoparticles relative to the number of surface atoms in bulk. As a particle decrease in size, a larger fraction of atoms are forced sit on

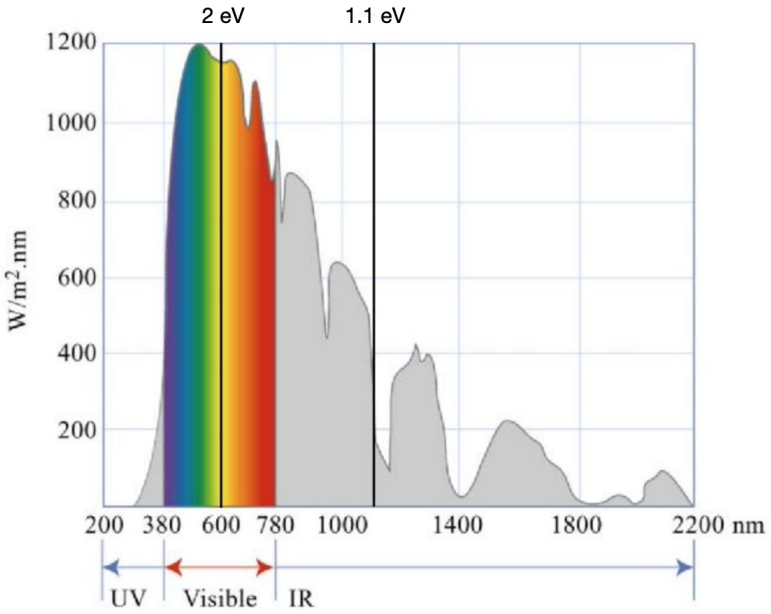

Figure 1.2: Solar irradiance spectrum adopted from [2]. Wavelengths corresponding to energies of 1.1 eV and 2 eV are outlined

the surface of the particle. These surface atoms experience a different and harsher environment than bulk atoms, causing properties of the particle itself to change. The other factor is related to quantum confinement, and enables controll of the bandgap by adjusting the particle size. This is possible since the particles eventually become smaller than the electrostatically bound electron-hole pairs, known as excitons, in the particle. This results in spatially confined charge carriers [6] because too few atomic orbitals are available to form continuous bands. This will increase the bandgap because electronic states at the edges of the valence and conduction bands become discrete. The relationship between the emission energy, the bandgap of the particle and the particle radius is described by Brus Equation [7].

$$\Delta E(r) = E_g - \frac{h^2}{8r^2}(1/m_e * + 1/m_h^*) \tag{1.2}$$

where m_e^* and m_h^* are effective mass of excited electron and hole respectively. It can be noted that $\Delta E = E$ from equation 1.1.

The 1.1 eV bandgap of silicon corresponds to a wavelength of 1110 nm as outlined in figure 1.2. By visual interpretation of figure 1.2 it was assumed that a bandgap of $\approx$ 2 eV and wavelength of 620 nm would complement the silicon bandgap of 1.1 eV successfully. Table 1.1 shows the bandgap of some ZnO based ternary oxides, all expected to form spinel-like structures. The spinel configuration has large synthetic flexibility [8] and the cubic fcc structure should be compatible with the hexagonal zincite structure of ZnO. Based on the bandgap, number of papers published and gut feeling, ternary oxides with antimony (Sb), vanadium (V) and iron (Fe) as the third element were selected as the most promising compounds.

This brings us to the goal of this thesis. That is, to investigate the Sb, V and Fe doped ZnO systems for possibilities to form nano precipitates inside a ZnO matrix, hence, expanding the function of ZnO based TCOs, and facilitate higher solar cell efficiencies. Synthesis routes will be customized to probe this concern, and

Table 1.1: Bandgap of some ZnO based ternary oxides [9]. Bandgap estimates obtained by DFT are marked (DFT calculations are known to underestimate the bandgap [10]).

Ternary oxide	**Bandgap (eV)**
Zn_2SnO_4	0.825 (DFT)
ZnV_2O_4	1.1
$ZnMn_2O_4$	1.24
Zn_2VO_4	1.601 (DFT)
$Zn_4As_2O_9$	1.62 (DFT)
$Zn_2As_2O_7$	1.763 (DFT)
$Zn_3As_2O_8$	1.897 (DFT)
$ZnFe_2O_4$	1.9
$ZnSb_2O_4$	1.92
$ZnWO_4$	2.14 (DFT)
$Zn_2V_2O_7$	2.505 (DFT)
$ZnBa_2O_3$	2.672 (DFT)
$Zn_3Ba_2O_6$	2.697 (DFT)
$ZnTiO_3$	2.88

characterization of samples will be done by different instruments and techniques. Thus, reaching for complementary and reliable results, and moreover shed ligth on an imporant field of renewable energy research.

Chapter 2

Theory

2.1 Solid state precipitation

In order to promote the precipitation of nanoparticles inside the ZnO matrix, a two-staged annealing process is intended. First step aims to dissolve a significant amount of the dopant element in the ZnO. The dopant atoms are expected to be randomly distributed and essentially incorporated inside the ZnO structure. As solubility normally is higher at higher temperatures, a subsequent annealing step at a lower temperature is added, and thereby making it energetically $unfavorable$ for the dopant atoms to remain being dissolved in the ZnO structure, thus, promoting a solid state precipitation of the dopant atoms.

Dopant atoms located close to grain boundaries or secondary phases may diffuse to these areas, but as diffusion is relatively slow in solid state, some dopant atoms are proposed to form precipitates inside the ZnO matrix instead. Size of the particles is expected to be controllable by doping concentration, as well as the annealing regime. Generally, by limiting the second stage annealing time, fewer impurity atoms have time to accumulate and thereby result in smaller particles. Also, if the temperature difference between the first and the second annealing stage is small, the difference in solubility is also generally small. This will in principle result in fewer precipitated dopant atoms in the ZnO matrix, and thus promote small precipitates. While if a highly dissolved doping concentration is obtained in the first annealing step, more atoms can be precipitated in the second annealing step, which could enable the precipitates to grow larger.

It should however be noted that these are simple predictions and have implications. High annealing temperature also promote fast diffusion, which in turn could result in larger particles by Ostwald ripening. Therefore, several variables must probably be tuned in order to exactly control the size of precipitates. In figure 2.1 the binary phase diagram of ZnO - Fe_2O_3 is provided [11]. This system has promising characteristics and is therefore used as an example. The zincite phase on the left side of the phase diagram is the most stable form of ZnO at ambient conditions, while hematite on the right side is the stable form of Fe_2O_3. Please note that composition is given as cation ratio.

We first consider point A, composition is 45 at% Fe and 55 at % Zn (black dotted line). This composition at the given temperature (1400 °C) is within a two phase region of the phase diagram, as it has single phase areas on both sides. Thus, we would expect to see two phases present when investigating a sample made in

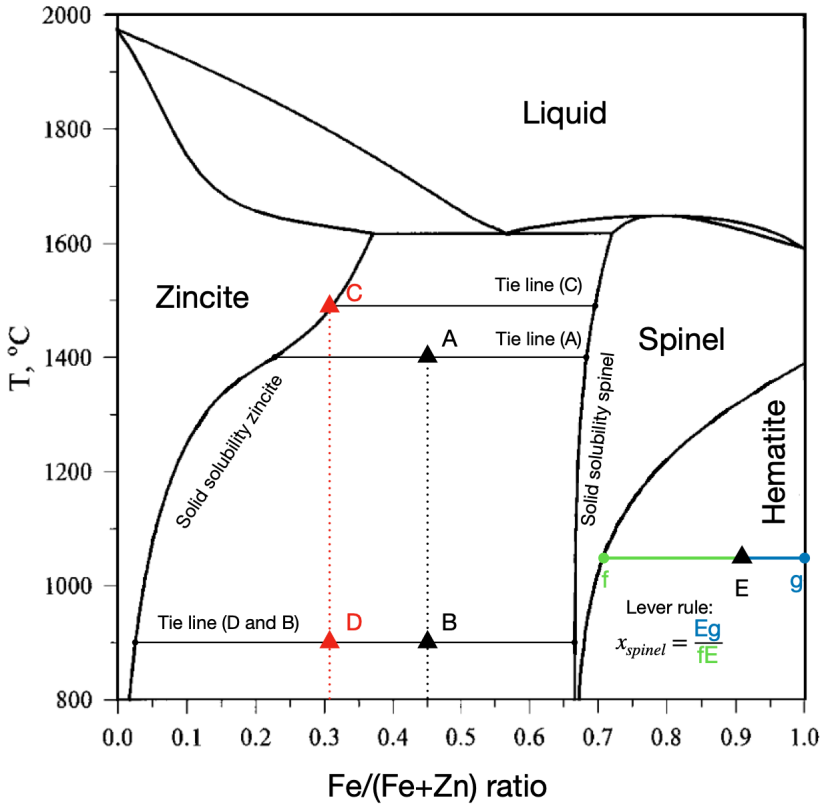

Figure 2.1: Binary phase diagram with components ZnO and Fe_2O_3 adopted from [11]. The points A,B,C and D are used for discussion in text. Tie lines and solid solubility lines are labeled. The procedure for applying the lever rule is sketched in spinel-hematite two phase region.

terms of point A. Compositions of the two phases are found by drawing a tie line, which is an isotherm through the sample composition from one phase area to the other, as shown in figure 2.1. Composition of each phase is found by reading out the composition at the intersect between isothermal line and the solid solubility line from the single phases. For point A that is zincite with ≈ 23 at% Fe, and 77 at% Zn, and a spinel phase containing ≈ 67 at% Fe and 33 at% Zn. It can be noted that, at this temperature, this is maximum solubility of Fe in zincite and Zn in spinel. The mole fraction of each phase can be found by using the lever rule. The procedure for applying the lever rule is sketched in the spinel+hematite two phase region in figure 2.1.

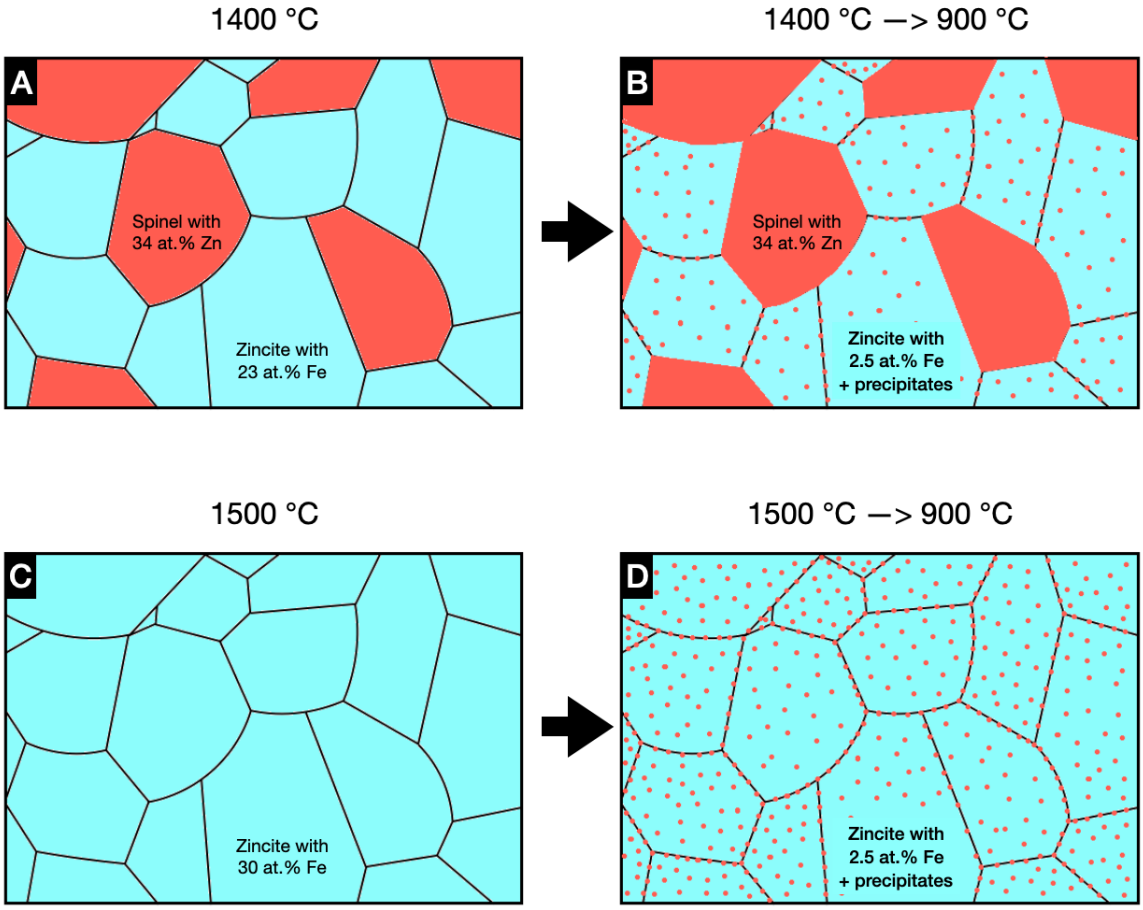

Figure 2.2: The drawings show expected microstructure with precipitates after the annealing processes A → B and C → D. The spinel grains are drawn slightly larger in B than in A to illustrate diffusion of precipitates to adjacent grains and excess of precipitates are drawn on the grain boundaries.

Let's now consider the situation in point B. Directly one can see that solubility of iron in zincite is lower at this temperature. This is also evident from the lever rule as more spinel phase is stable at this temperature. As the total amount of available Fe atoms is the same in point A and point B, a larger fraction of Fe atoms must be located in the spinel phase in point B than in point A. If a sample first is heat treated in terms of A, then subsequently cooled to point B, fewer and fewer Fe atoms can be held by the zincite structure as the temperature decreases. It is anticipated that some Fe atoms located inside zincite grains aren't able to diffuse to neighboring

spinel grains, and instead, accumulate and nucleate as precipitates inside the zincite structure. The proposed microstructure of a sample prepared in terms of point A is shown in figure 2.2A, while figure 2.2B shows the proposed microstructure of a sample first heat treated in terms of point A, then subsequently in terms of point B. The term annealing history could be used here, and one could say that sample 2.2B has an annealing history in terms of point A.

If the latter procedure is applied to a sample prepared in terms of points C and D, diffusion to neighboring spinel grains is prevented as we start off with a single phase in point C. As the solubility of iron in the zincite phase is higher in point C, we predict a higher iron concentration in the zincite structure than in point A. Therefore, when this sample is cooled to D, we would expect larger particles or alternatively a higher density of precipitates than what was seen in sample B. In figure 2.2D, a higher density of precipitates is shown.

2.2 Bulk thermodynamical stability

What phases being stable at different temperatures can be predicted by considering the Gibbs free energy of a given phase:

$$G = H - TS \tag{2.1}$$

where G is Gibbs free energy, H is enthalpy, T is temperature and S is entropy.

Nature always want to minimize G, therefore a single phase is considered thermodynamically stable if the Gibbs free energy is a global minima, while it is considered metastabile if G is a local minima. However, in both cases the derivative of G is zero:

$$\delta G = 0 \tag{2.2}$$

At a given temperature, free energy curves can be draw to illustrate the thermodynamicall stability. The curves are constructed by applying equation 2.1 to a range of compositions, and then equation 2.2 can be used to determine the most stable configuration. To show how this is done we let g_α be the molar Gibbs free energy of a pure substance α, and let X_α be the molar fraction of α. Then $g_\alpha X_\alpha$ is the Gibbs free energy of a given amount of g_α. It can be noted that the molar Gibbs free energy is also known as the molar chemical potential. However, Gibbs free energy can be found likewise for another pure substance β and by combining the two free energies we obtain [12]:

$$g = g_\alpha X_\alpha + g_\beta X_\beta \tag{2.3}$$

This is physically equivalent of having a wall separating two pure substances, and the free energy curve is a straight line going from g_α to g_β. However, if the walls are removed the atoms in substance α and β can mix, and entropy comes into play. If we assume an ideal system (approximation), enthalpy can be set to zero:

$$\Delta G = -T\Delta S \tag{2.4}$$

As entropy is a measure of disorder, this expression forms a curved line with a minima when the mixture is most random. In figure 2.3 the expressions given

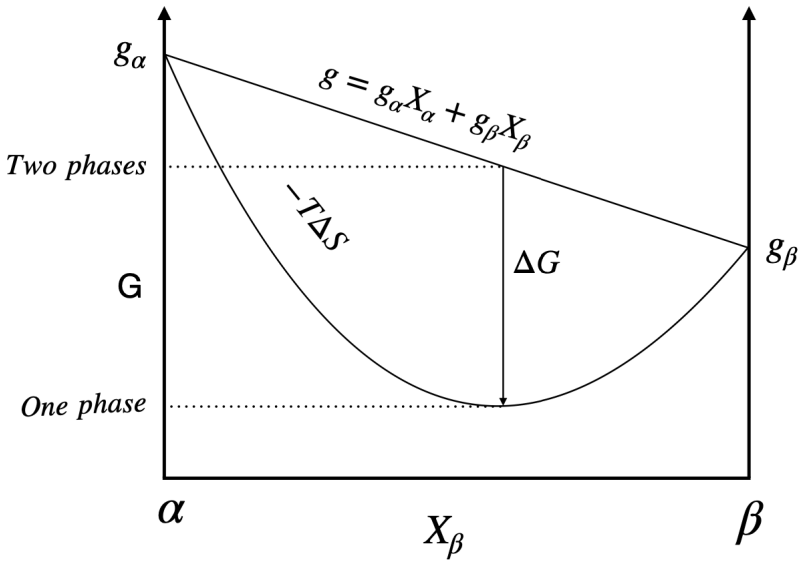

Figure 2.3: Free energy diagram of two pure substances, and the reduction in free energy resulting from mixing of the substances.

in equation 2.3 and 2.4 are sketched. We see that by mixing α and β entropy increases, and the minimum of Gibbs free energy is found where the mixing is most random. From equation 2.2 we see that this configuration will be thermodynamically favorable. Hence, the system can lower its Gibbs free energy by forming one phase rather than keeping the two substances separated. The change in Gibbs free energy for the phase transition is labeled ΔG in the free energy diagram in figure 2.3.

Such free energy curves can be used to compare stability of multiple phases. By recalling point A in figure 2.1, two phases were stable at that temperature and composition. This situation can be represented by two free energy curves having their minimums on each side of the sample composition. A line connecting the two curves through their common derivatives show the decrease in free energy associated with forming the two phases spinel and zincite rather than keeping a single phase zincite structure with high concentration of iron. This is illustrated by the black curves and the black ΔG arrow in figure 2.4. As we know the solubility of Fe in zincite is reduced at lower temperatures. The free energy curve for the spinel phase at the temperature of point B is shown as a red curve in figure 2.4. To facilitate comparison, it is assumed that the free energy curve for the zincite phase has not changed, and thus red and black curve overlap for this phase. Of course both curves are moved to higher values of G as the temperature decreases. However, the point is that the driving force (ΔG) for forming two phases (zincite+spinel) is larger when solubility is decreased. This can be seen by comparing the magnitudes of the black and red arrows showing ΔG associated with the phase transitions at 1400 °C and 900 °C respectively.

That the red curve in figure 2.4 indeed show a reduced solubility of iron in zincite can be motivated by two observations. First, the intersect of the red tangent on the zincite free energy curve is at a lower Fe concentration than black tangent. Secondly, the mole fraction of each phase can be calculated by applying the lever rule. As the intersects between tangents and curves are compositions of each phase, and the tangents drawn for each temperature can be considered tie lines. It is clear that

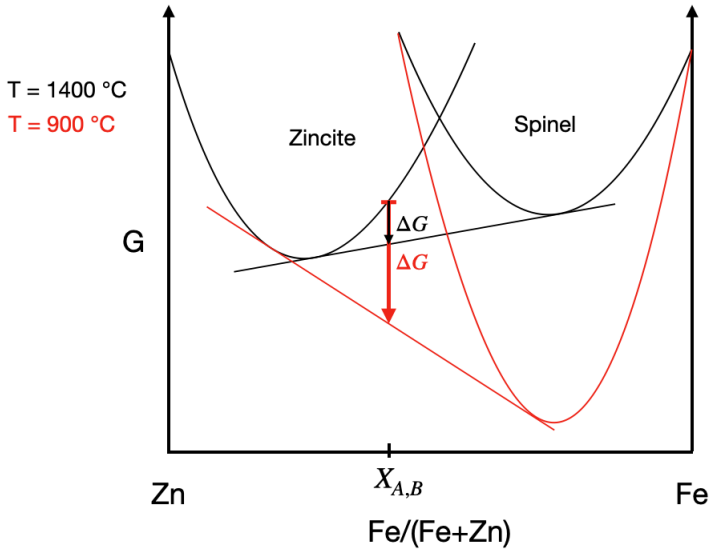

Figure 2.4: Schematic free energy curves for the zincite and spinel phase at 1400 °C and 900 °C. The black curve and the red curve illustrates the thermodynamic situation in point A and point B from figure 2.1, respectively. The black and red curve overlap for the zincite phase.

the red curve show more spinel phase being stable than the black curve, thus the solubility of iron in zincite must be reduced for the red curve.

However, a large thermodynamicall driving force for a reaction does not equal a fast reaction. In order to say something about reaction rates we must consider kinetics.

2.3 Kinetics

In the same way Gibbs free energy tells if a reaction is thermodynamically favorable, kinetics tell how fast it will go. The rate of a reaction is often described by the Arrhenius equation:

$$rate \propto exp\left(\frac{-\Delta G^{\alpha}}{RT}\right) \tag{2.5}$$

where ΔG^{α} is the activation energy and R is the universal gas constant and T is the absolute temperature (in kelvins).

From equation 2.5 we see that high temperatures give fast reactions. For solid state precipitate reactions we could assume that ΔG^{α} is the energy needed for the dopant atoms to escape from the host matrix and form a precipitate. Therefore, if the solubilty changes considerably in a small temperature range, and that change of solubilty takes place at a high temperature, this should facilitate fast precipitate reactions. Hence, systems with highly temperature dependent solid solubility in ZnO are, to some extend, assumed to be promising for the purpose of solid state precipitation.

In order to understand this, the changes in enthalpy must be considered. In the following we propose a model for the rate of precipitation by adopting a somewhat chemical approach, that is, the reaction rate diagrams. The model is based on the

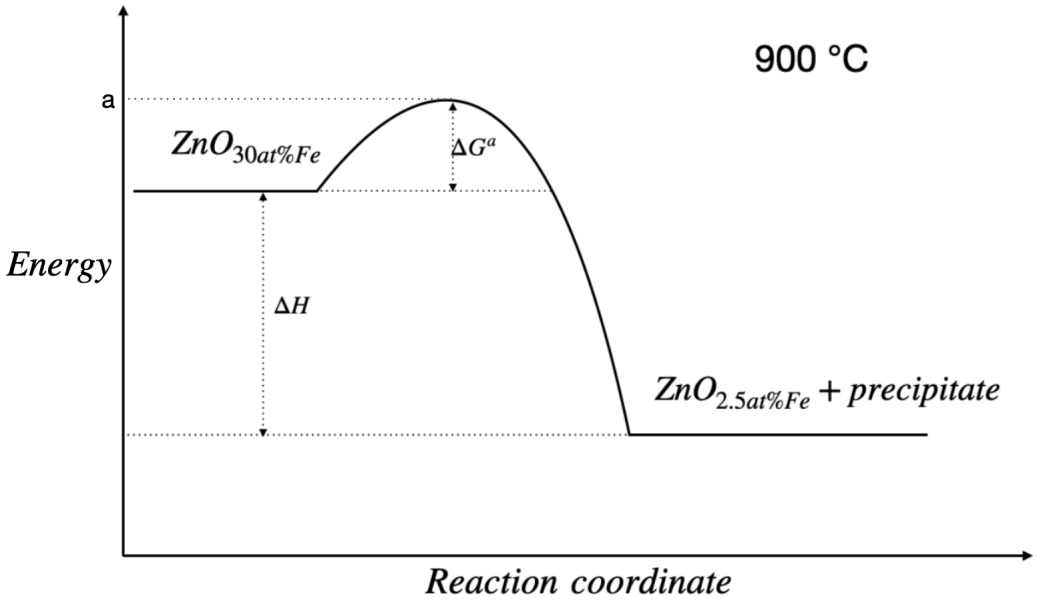

Figure 2.5: Assumed precipitation reaction rate for a sample quenched from point C to point D in figure 2.1.

properties in the ZnO – iron system, given by the phase diagram in figure 2.1, but is expected to be valid in other systems with similar properties. The activation energy can be considered the minimum energy needed in collision between species to result in a chamical reaction. Based on this we will assume that the apex (labeled "a" in figure 2.5) of the ΔG^{α} bump will not change with doping concentration in the system. However, increased doping concentration is usually related to increased enthalpy, as enthalpy is a measure of heat contained in a system. The enthalpy is often expressed as:

$$H = E + PV \tag{2.6}$$

where E is internal energy, P is pressure and V is volume.

In most cases of condensed state systems the PV term can be neglected and thus $H = E$. Further, the internal energy E can be divided into a kinetic contribution which is related to vibrations, translation and rotation, and a potential energy term which is related to bonding of atoms. As we initially needed a lot of heat to dissolve high concentrations of iron into the zincite structure, a lot of energy was transferred to the system. This will increase the enthalpy in the same system, and the bonding between zinc and iron atoms will have high potential energy. If the same structure is quenched to a lower temperature, say 900 °C, the enthalpy in the system is initially maintained, however the structure has an excess of energy compared to the stable configuration at this temperature. The excess of energy is labeled ΔH in figure 2.5, and is expected to reflect the soluted iron concentration. Thus, as the apex of ΔG^{α} is not changing with concentration, it is proposed that the rate of the reaction is determined by iron doping concentration. As a high iron doping concentration increase ΔH and consequently reduce ΔG^{α}. More qualitatively, we could easily imagine that the bonding to iron atoms is increasingly less pleasant for the zincite structure when temperature suddenly drops if the initial potential energy of the bonds was high. The reaction coordinate diagram shown in figure 2.5 illustrates

these predictions schematically for the situation where a sample is quenched from point C to point D in figure 2.1.

2.4 Nanoparticle stabilty

As nanoparticles have a significant amount of surface atoms, an extra term must be added to the Gibbs free energy equation:

$$G_{bulk} + G_{surface} = H - TS + A\gamma \tag{2.7}$$

where γ is the energy required to form one unit area of surface, and A is the magnitude of the unit area.

Equation 2.7 show that bulk phase stability is different from nano phase stability, as the surface to volume ratio is negligible for bulk, but is significant for nano materials. This essentially reduces the stability of the nanoparticles, however it also shows that other polymorph phases than what is predicted from the phase diagram can become stable when particles get really small [13].

Chapter 3

Materials and structures

3.1 Spinels

Spinels have traditionally been utilized as red and blue precious stones, and are found naturally in minerals all around the world. In fact, most main group elements and transition metals can be incorporated in stable spinel structures.Owing to the abundance, large synthetic flexibility and a wide range of atomic and electronic configurations, the spinel structure properties are of great scientific interests, and a useful material within many technological applications [8].

A spinel unit cell contain eight face centered cubic (fcc) unit cells with oxygen atoms at each lattice point. This gives a cubic close-packed array of 32 oxygen atoms. Cations occupy one-half of the 32 octahedral voids and one-eighth of the 64 tetrahedral voids. This gives the typical site distribution ratio in spinels: (8:16:32=1:2:4). The site distribution of cations may vary, however a general formula for a ternary oxide spinel may be expressed as:

$$(A_{1-x}B_x)^{tet}(A_xB_{2-x})^{oct}O_4 \tag{3.1}$$

with $0 \leq x \leq 1$, being the inversion degree parameter. Divalent cations (+II) are shown as A and B are trivalent cations (+III).

Normal spinels have x=0, but if trivalent cations occupy tetrahedral voids, the degree of inversion raises, and at x=1, the spinel adopts an inverse structure [14]. A completely random distribution is characterized by inversion parameter of x=2/3. The zinc spinel ferrite ($ZnFe_2O_4$) has an adjustable distribution, and optical properties have been claimed to change as the inversion degree increases [15]. Traditional rationalization of spinel cation distribution are based on crystal field stabilization energy (CFSE) and Madelung energies. However, as indicated in *A modern Mendelyevian approach study* by Geoffrey D. Price et. al. [16], size considerations and electronegativity could be more important factors in determining relative site preferences.

3.2 Zinc oxide

ZnO is an abundant material with great potential in technological applications due to its optical/electronic/biocompatible/chemical properties, also making it widely studied material in several scientific fields. Still, in large-scale industry only a small

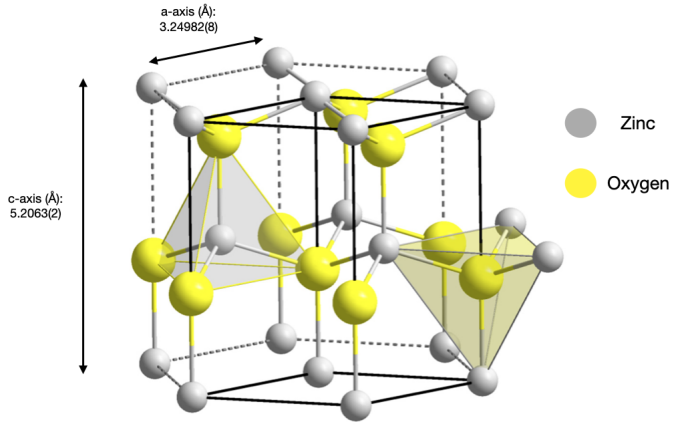

Figure 3.1: Unit cell of hexagonal ZnO (Wurtzite). The a- and c-axis lengths shown are obtained in this study. Adopted from public domain [25].

portion of usage is related to the functional properties of ZnO. Actually between 50 % and 60 % of ZnO usage is in rubber industry, followed by ceramic industry, concrete manufacturing, sunblock creams, food and pigments [17].

However, when p-doped galium nitride (GaN) was proven possible by Akasaiki, Amano and Nakamura, a finding awarded with the Nobel Price in physics in 2014, the ZnO research on optical and electronic properties also picked up speed, as both GaN and ZnO crystallizes in the wurtzite structure and have extensive similarities in electronic band structure, with a direct bandgap of 3.37 eV [18] and 3.4 eV [19] respectively. This make them suitable as TCO materials. The research leads to the discovery of other applicable TCO properties, as good optical transmittance in the visible region, ranging from $\approx$ 80 % [20][21] up 93 % [22], as well as low resistively ($\approx 10^{-4}\ \Omega\,\mathrm{cm}$ by doping with aluminum and gallium [23]). In addition can the bandgap of ZnO be tuned by additions of e.g. magnesium [24].

The wurtzite ZnO structure is hexagonal, and has a sixfold rotational symmetry when viewed down the c-axis. This symmetry property will be important when we consider the ZnO – iron system in Chapter 5. Both zinc and oxygen are tetrahedrally coordinated as shown by tetrahedrons in figure 3.1. The Zn$-$O binding is at the border line between covalent and ionic due to very strong electronegativity of oxygen compared Zn, which leads to a considerable degree of polarity [26]. Therefore, the c-axis of the unit cell also has a pronounced polar character, as the (001) plane is Zn^{+2} terminated and the (00-1) plane is O^{-2} terminated.

Despite the exciting properties, ZnO has not yet shown its full potential as a function material, mostly because of the inability to obtain stable p-type doping. The ZnO research has apparently changed direction and is now more focused on nanostructure morphologies obtained by different synthesis routes [17]. However, in the same paper[17], Michal A. Borysiewicz demanded for ZnO research to move towards device development and market presence. As TCO applications are not dependent on p-type doping, device development within this field seems conceivable.

3.3 Inversion domain boundaries

Inversion domain boundaries (IDBs) are abrupt changes in the repetitive ordering of atoms and introduces structural anisotropy in the ZnO lattice by flipping the c-axis. The inversion boundary formation in ZnO is triggered by doping of spinel forming oxides such as SnO_2, Sb_2O_3, In_2O_3 [27] and Fe_2O_3 [28]. The IDB formation in ZnO has been shown to play a key role in the growth rate of the ZnO grains. In varistor applications this is an important feature, since electrostatic barriers at the ZnO grain boundaries causes a highly non-linear current-voltage response, and thus relates IDB formation to electrical conductivity of ZnO [29][30].

Sb_2O_3 only seem to trigger basal IDBs, and only one IDB is present in each grain [27]. The ZnO domains on each side of the IDB have a so-called head-to-head orientation. That is, the c-axis in both ZnO domains are oriented with the positive direction perpendicular to the prolongation of the IDB, and thus point towards each other. Based on this, it is also intuitively fine that only one IDB is present in each grain, since there is seemingly no way of having the head-to-head orientation again in the same crystal. However, in Fe_2O_3 doped ZnO, two different IDBs can be present in the ZnO structure. That is basal IDBs and pyramidal IDBs. The pyramidal IDBs swaps the c-axis back, and thus the head-to-head orientation is again possible. This gives an alternating periodicity of the basal and pyramidal IDBs. Both types of inversion domains have a specific orientation in the ZnO structure. Basal IDBs are perpendicular to the c-axis, that is parallel to $\{0\,0\,0\,1\}$ planes, and the pyramidal IDBs are parallel to $\{2\,\bar{1}\,5\}$ planes [28].

It has been claimed by Haug [9] that a relationship between Fe doping concentration and spacing between basal IDBs was observed. It was shown that higher Fe concentrations gave shorter spacing between the basal IDBs.

Nina Daneu, Slavko Bernik and Aleksander Reč [30][27] have suggested that the formation mechanism for IDBs depends on the valency of the IDB forming dopant element and that the driving force for inversion is preservation of local charge balance. Two competing formation mechanisms were identified: (i) internal diffusion, and (ii) surface reaction and growth. The first is characteristic for +III dopants, whereas the latter holds for dopant valences higher than +III. Both nucleation mechanisms are proposed to be related to zinc-self diffusion at elevated temperatures [31]. The zinc self-diffusion generates Zn-vacancy clusters, and depending on valency of dopants these cluster are charge compensated either by (i) or (ii).

No articles were found on vanadium doped ZnO with IDBs.

Chapter 4

Method

4.1 Synthesis

In this work a powder synthesis route was followed, where constituent powders are mixed and pressed into pellets before annealing. However, in the ZnO – Fe system a single crystal of ZnO was placed in the middle of constituent powders. Samples prepared in this way are commonly referred to as diffusion couples (DCs). It was decided that the composition of the powder mixtures were to be given in atomic percent (at%). The ratio of powder to be weighted out was simply calculated by:

$$\frac{\#\ of\ moles\ A}{total\ \#\ of\ moles} = at\%\ A \tag{4.1}$$

where A is a given element. The requested at% of A is inserted, and weight needed of each constituent component (e.g. ZnO and Fe_2O_3) to obtain the given molar fraction is calculated from their molar mass.

However, in most parts of the text, compositions are given as atomic cations ratios. That is, not including the moles of oxygen in equation 4.1. This was essentially done because of difficulties in obtaining correct oxygen quantification values, as discussed in section 4.2.5. The powder used in this work are listed in table 4.1.

Table 4.1: Powder used in experiments.

Compound (powder)	**Supplier**	**Purity (%)(trace metal basis)**	**Catalog number**	**Lot number**
ZnO	Aldrich	99.99	255750	MKBV7814V
Fe_2O_3	Alfa Aesar	99.5	012375	A12U017
Sb_2O_3	Aldrich	99.99	379255	MKCF7409
V_2O_4	Aldrich	≥ 99	215821	MKCD9436
V_2O_3	Aldrich	99.99	463744	0000058171
V(metallic)	Aldrich	99.9	774065	MKCJ8207

The ZnO single crystals were hydrothermally grown and 10 mm × 10 mm × 0.5 mm in size. The c-axis of the ZnO singel crystal was perpendicular to the square surface, and the sides were terminated by $(1\,\bar{1}\,0)$, $(\bar{1}\,\bar{1}\,0)$, $(\bar{1}\,1\,0)$ and $(1\,1\,0)$ planes as

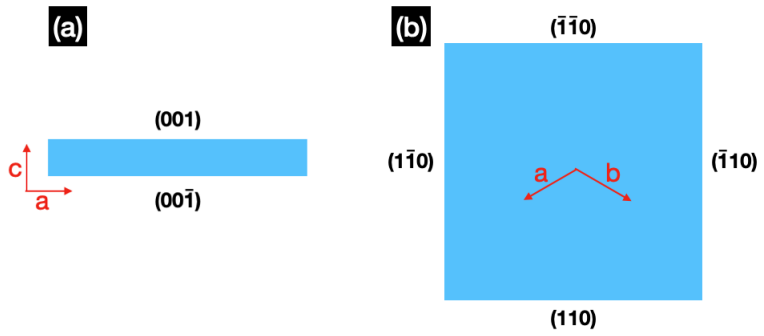

Figure 4.1: (a) Schematical illustration of the cross section of the single crystal used in this work (b) Show the square surface when the single crystal is viewed down the c-axis.

shown in figure 4.1. The ZnO single crystals are commercially available from MTI Corporation.

Prior to pelletizing, the weighted out powder was ball milled. Ball milling is a type of mechanical grinding process often used as a step in a synthesis route to homogenize and minimize particle size, or even as an independent method to create nanotubes, nanoparticles and other nanostructures [32] [33]. In this work, ball milling was performed to obtain small particle size and thoroughly mixing of the constituent powders. Small particle size is important since this also gives larger surface area and therefore higher reactivity. Thoroughly mixing is important for obtaining short diffusion lengths and form the thermodynamical stable phases as the powders are annealed. A planetary ball mill was used and driven at 300 rounds per minute (rpm) for two hours. Isopropanol was applied to give wet conditions, which have shown to increase the grinding efficiency [34]. Inside the rotating cylinder, 30 agate ceramic balls with a diameter of 10 mm performed an internal cascading motion which grinded and smashed the powder into small particles. The agate mortar had a volume of 100 cl, and isopropanol was filled until just above level of balls and powders. Considerations should be taken regarding the rotational speed, as a high energy (many rpms) mixing may also lead to unintended reactions taking place during the milling (i.e. oxidation of lower valency oxides) [33]. In addition, inconvenience with respect to risk of contamination should be considered.

After ball milling, the powders and isopropanol was separated by evaporating the isopropanol in a heating cabinet at $\approx$ 80 °C.

Then, the powders were pressed into pellets with a hydraulic pellet press, using a force of 1 ton, and 10 mm diameter dies. Pelletizing has some advantages, it gives reproducibility as density is controlled, higher reactivity since more surface is in contact and it's a convenient state regarding transport etc. A binder was added prior to the pressing to give high reactivity, this burned off at $\approx$ 600 °C as it is organic, and thus did not contaminate the sample.

The last step of synthesis was annealing of the pellets. As thermal energy is delivered to the system, new phases can become stable. The heating rate was programmed to be in the range 150 °C/h to 300 °C/h, depending on the furnace. However, it is not believed that this parameter has a large influence on the result. The dwell time was varied, depending on the system being investigated, but generally it should be long enough for reactions to occur and for the sample to homogeneously

reach thermodynamical equilibrium. The cooling rate was varied in the range 150 °C/h to 300 °C/h. Generally, kinetics were expected to be slow enough so that no phase transformations happened during cooling. However, some samples in the ZnO – Fe system did show indications of fast phase transitions during cooling, therefore a portion of these were quenched from maximum annealing temperature to ≈ room temperature, by dropping in water. By that, aiming to freeze the atomic configuration, and enable investigation of sample "as it is" at max temperature.

4.2 Characterization

The ambition is to show how different characterization methods can complement each other to achieve a thorough understanding of the material, but also the satisfaction associated with consistent results. In order to succeed with this, consciousness of the strength and weaknesses of each instrument is important. In the following a brief overview of the instruments used in this work is given. Some instruments take advantage of the repetitive atomic ordering in crystals to obtain information and are usually related to diffraction. Others are based on the photon emittance/reflectance or the non-coherent electron scattering from the sample, which offer a wide range of information to be collected. Further, the quantitative nature of atomic orbitals can render compositional and electronic band related information.

4.2.1 Optical microscope

Light microscopes are composed of optical lenses, and bend light to produce magnified images. Because of the difference in the refractive index between glass and air, light will travel at different speeds in the two mediums. In convex lenses, the portion of rays closest to the optical axis enter the slow medium (glass) first and thus bends towards the optical axis after passing through the lens. In concave lenses ligth will be bent away from the optical axis. The rays that enter a convex lens at equal angles will intersect in the back focal plane of the lens, and the rays that originate from the same point source on the object will intersect in the image plane. From the lens makers formula (4.2) and from the magnification (4.3), it is clear that the object placement relative to the focal length of the lens determine the magnification. In the formula (4.2), D_1 and D_2 are the distance from the object to the objective lens, and the objective lens to the image plane, respectively, and f_0 is the focal length of the lens.

$$\frac{1}{f_0} = \frac{1}{D_1}\frac{1}{D_2} \tag{4.2}$$

$$M = -\frac{D_2}{D_1} \tag{4.3}$$

In figure 4.2 a compound light microscope and the corresponding ray diagram are sketched. The total magnification is the product:

$$M_{objective} * M_{eyepiece} \tag{4.4}$$

In the process of characterization, the easiness and time-saving benefits of light microscopes was appreciated. As the morphology and colors show up nicely, light

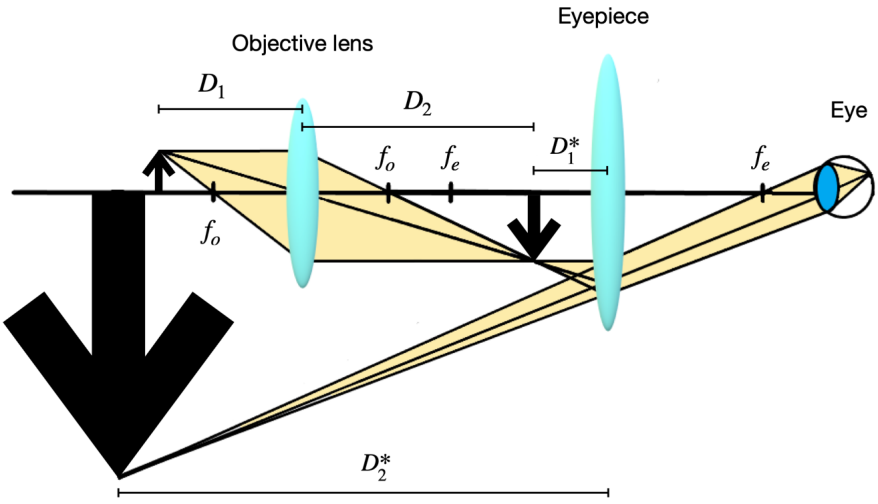

Figure 4.2: Ray diagram and lens placement in a compound light microscope. This lens placement produce a virtual image.

microscope served as a tool to get an overview of the specimen. In addition, transmission light microscopes were used to check the grinding marks when preparing samples for the scanning electron microscope. By grinding in only one direction for each grinding paper, one can check if each grinding step removes the previous grinding marks. This was a good way of ensuring a good surface quality on the samples.

Because the wavelengths used for imaging are in the visible region of the electromagnetic spectrum, contrast by colors is obtained. In several cases this proved to be a prominent asset, as this type of information is lost in other instruments. By inserting polarized filters only selected polarizations of the ligth are used for imaging. This can give information related to the orientation of the observed crystals.

Both spherical and chromatic aberrations decrease the resolution in light microscopes. However, the same feature that makes the light microscope powerful, that is the possibilty to see colors, also cause a fundamental resolution limit. This is known as the Abbe resolution (equation 4.5), and states that the resolution is limited by the wavelength of the waves (λ), and the numerical aperture ($NA = n \sin\theta$) of the microscope.

$$Abbe\ resolution_{x,y} = \lambda/2NA \tag{4.5}$$

This limitation arises from the diffraction of light. When light passes through a circular aperture, a circular diffraction pattern occurs in the image plane. This is known as an Airy disk, and the separation between these disks render what's possible to resolve.

Optical microscope images in this work were acquired using an Olympus BX50 microscope.

4.2.2 X-ray diffraction (XRD)

X-ray diffraction is a technique where x-rays are elastically scattered by electrons in the specimen. The periodic arrangement of atoms cause diffraction of x-rays, this is possible since the wavelengths of x-rays typically are compareable to interatomic

spacing in magnitude. The diffraction may result in constructively or destructively interference depending on the plane distances in the crystal, the incident angle and the x-ray wavelength. This relationship is known as Bragg´s law (equation 4.6).

Given a wavelength (λ), the incoming x-ray angle (θ) can be varied, and Bragg´s law will be satisfied at different angles for different planar spacings (d-values) in the crystal. When Bragg‘s law is satisfied, the interference of scattered x-rays is constructive. This show up as peaks in the diffractogram where the peak intensities are usually plotted as a function of (2θ). From the diffractogram, the d-values can easily be calculated using Bragg‘s law.

$$2d \sin\theta = n\lambda \tag{4.6}$$

Non-periodic arrangement of atoms also cause diffraction. However as there are no repeating plane spacings, the intensity obtained by Bragg´s law will appear continuous and with no sharp peaks.

XRD was used to determine phases present in samples and structural properties such as unit cell parameters and specific d-values. The software DIFFRAC.EVA version 4.3.0.1 with PDF-2 Release 2014 RDB database integrated was used to analyze the diffractograms. For refinement of unit cells, the software UnitCell version 0.95 was used. The relative peak intensities provided information about relative amount of phases and peak broadening was considered in regards of grain size and deformation.

The XRD samples were prepared by crushing the material to be analyzed to powders with mortar and pesle. The crushed powders were applied on glass or silicon holders, were the latter gives a lower background and is thus favorable when small amounts of material are available. The powders are essentially many small crystals with a random orientation on the sample holder, ensuring all d-values are detected. For calibration purposes, silicon 640d from the NIST standard was added.

The XRD analyzes in this work were carried out using a Rigaku MiniFlex600 diffractometer with a copper target.

4.2.3 Scanning electron microscope (SEM)

As highly accelerated electrons have much smaller wavelength than photons, this will enable higher resolution. Figure 4.3 show the difference in wavelength for highly accelerated electrons vs photons in the visible region of the electromagnetic spectrum. From the plotts we see that much shorter wavelengths are obtained by the highly accelerated electrons.

In SEMs an electron beam is focused to a probe by a set of electromagnetic lenses and raster over the specimen. Electrons are generated by an electron gun and the resolution of the microscope is related to the energy spread of the electrons created. If the electron energies are fluctuating, this will limit the ability to form a focused probe in the lens system.

In figure 4.4 some signals generated when a high energy electron beam enters a specimen are shown. Inelastic electron interactions in the material generate secondary electrons (SE). These electrons are scattered by the electron beam and leave a vacant hole in the structure. When electrons from higher energy levels recombine with the hole, some energy must be released, and the emittace of x-rays is one way

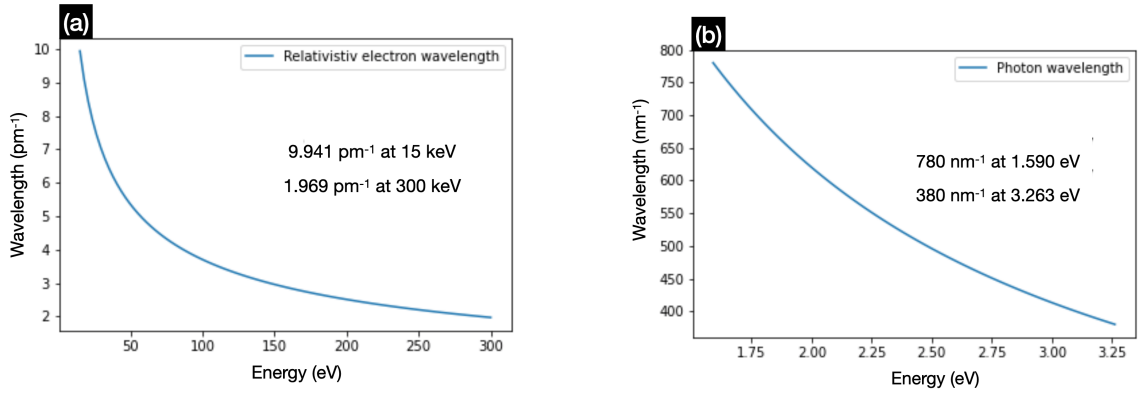

Figure 4.3: (a)Electron wavelength as a function of energies typically used in SEMs and TEMs. (b) Photon wavelength as a function of energy in the visible part of electromagnetic spectrum.

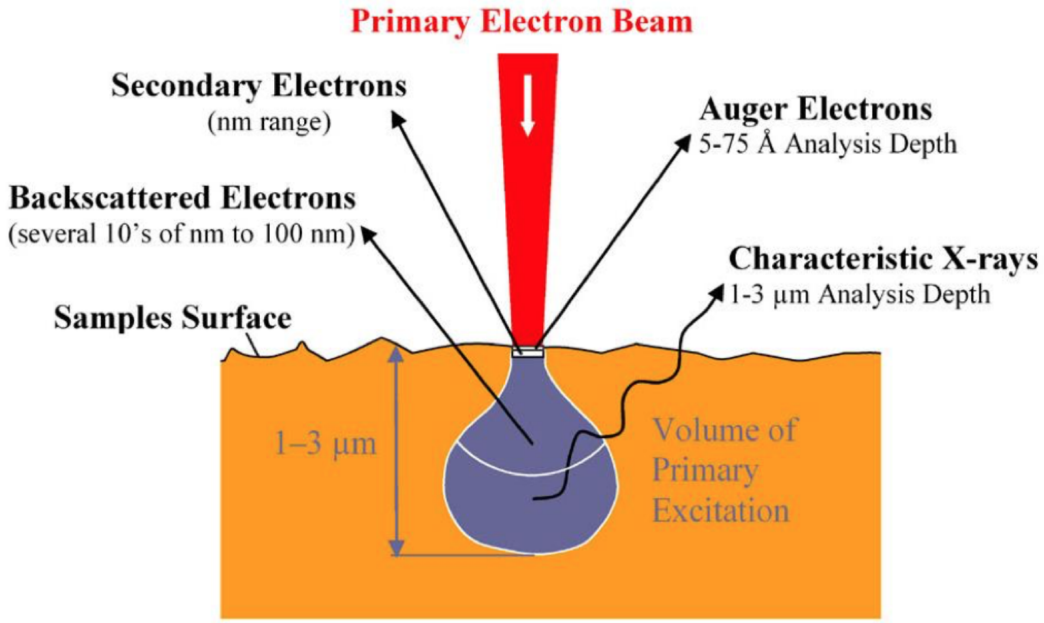

Figure 4.4: Signals generated when electron beam interact specimen. Taken from lecture notes in UiO course MENA3100 [35].

of doing this. It can be noted that this is how x-rays are generated for energy dispersive spectroscopy (EDS), and in a XRD diffractometer. One other way of releasing the energy is by emitting an auger electron. In this work we used the backscattered electrons (BSE) for SEM imaging, even though SE images generally provide better resolution than BSE images due to the small region where electrons are generated from. However, the low energy of the SE require detectors with an applied voltage to be efficiently detected, and the SEM used in this work was not equipped with this detector. The BSE are elastically scattered by nucleuses in the specimen, and the emission is highly dependent on the atomic number of the probed region. The emisson rate changes most for the atoms with an atomic number up to 40, and even as small changes as 0.2 in average atomic mass can be detected in this range

[36]. The contrast in SEM BSE images is well suited for compositional analysis, as different elements and phases show up with different contrast on the images. The BSE detector is annular and placed directly above the specimen.

Prior to investigation, most samples were embedded in an epoxy resin named Demotec 33. This made the samples more convenient to work with. Then most samples were cut in cross sections using a Allied TechCut 4 low speed saw with a 0.38 mm thick blade. The cross sections were grinded with diamond foils having progressively smaller diamond grain size. Starting from 30 µm and ending up at 0.5 µm grain size. If SEM samples were to be investigated in XRD or transmission electron microscope, the epoxy resin was removed by dissolving it in acetone.

The SEM used in this work was a Hitachi TM3000 Tabletop microscope.

4.2.4 Transmission electron microscope (TEM)

In TEM the electron beam is accelerated to even higher energies (200 keV to 300 keV), empower higher resolution. The beam travels through the sample, and intensity results from diffraction contrast, mass/thickness contrast or phase contrast, depending on the technique. A fluorescent screen or cameras placed below the specimen are used for viewing. Both imaging and diffraction are commonly used TEM techniques and switching between the modes is done by strength adjustments in the electromagnetic lens system, projecting either diffraction plane or imaging plane down onto the screen, see figure 4.5. The electromagnetic lenses produce a magnetic field, changing the electron path by Lorentz forces.

Within TEM diffraction and imaging there are also several sub techniques frequently used in this work. As illustrated in figure 4.5, apertures can be inserted into the microscope column, making it possible to select specific parts for the rays. Selected area diffraction (SAD) aperture is used in diffraction mode and gives a diffraction pattern from a specific area of the specimen. Objective aperture is used in imaging mode and can be inserted to select rays scattered at specific angels for imaging. Generally, an image is referred to as bright field image if the central beam is selected for imaging, and dark field image if only scattered rays are used for imaging. Weak-beam dark field microscopy is a technique rendering defects more visible. It also proved to be good way of imaging inversion domain boundaries.

High resolution TEM (HRTEM) is an imaging technique based on phase contrast produced by interference in the electron wave in the imaging plane. This technique enables high resolution images, but requires simulation to interpret and separate contrast from atoms and empty space, as the image is influenced by aberrations of the imaging lenses in the microscope. Samples need to be tilted to zone axis in order to obtain clear lattice fringes. Fast Fourier Transforms (FFT) can be applied to HRTEM images giving a power spectrum based on the repeating features seen on the HRTEM image. Scanning transmission electron microscopy (STEM) is a technique where electron beam is focused and scanned over the specimen. High angle annular dark field detector, medium annular dark field detector and bright field detector have different radii, detecting electrons scattered at different angles. As detector collection angles increase, more high-angle scattered electrons are detected by the detector. The high scattering angels results from interaction with nucleuses in the specimen, hence giving Z-contrast. While smaller collection angles give more diffraction contrast.

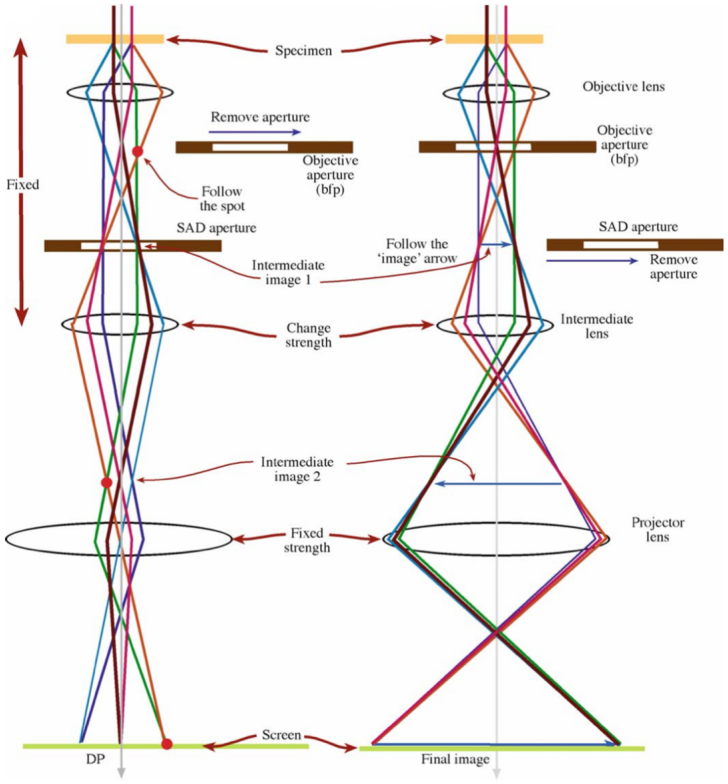

Figure 4.5: Ray diagram for a TEM microscope in diffraction mode to the left and image mode to the right. This illustration is taken from [37].

As the specimen must be electron transparent, thickness of TEM samples is usually 100 nm or less. Two different routes were followed to obtain this: drop casting powders on holey carbon films and mechanically grinding bulk samples using a MultiPrep and final thinning by a precision ion polishing system (PIPS). The latter route provides samples having their original microstructure intact, which can make interpretation easier. Whereas the first route is a timesaving alternative.

The TEMs used in this work were JEOL 2100F and FEI Titan 60-300.

4.2.5 Energy dispersive spectroscopy (EDS)

In SEM, TEM and STEM, energy dispersive spectroscopy (EDS) is an analytical technique used to obtain quantitative and qualitative data of elemental composition. The EDS detector is usually integrated in the microscope and detects x-ray energies produced as the electron beam interact with electron clouds from various elements in the specimen. A software constructs a plot of x-ray counts vs energy, and peaks in the plot can be assigned to an element because each element produce characteristic x-ray energies. Usually the K and L energy-level shell are used for characterization. Peaks from different elements may overlap, and require careful interpretation. Contribution from sample support, sample holder or column in microscope may result in artifacts. Lighter elements (below Na) are somewhat difficult to detect because the probability of generating an x-ray is proportional to atomic number, and risk of x-ray being absorbed is greater for low energy x-ray produced by low atomic number elements. In SEM EDS one must also consider the large excitation volume resulting from using bulk samples. X-rays have the highest excitation volume compared

to BSE and SE. The volume can be estimated by a Monte Carlo simulation and gives a light bulb shaped volume being $\approx 1\,\mu m$ to $3\,\mu m$ deep and wide, depending on accelerating voltage and sample material. This is schematically shown in figure 4.4.

Chapter 5

The zinc oxide – iron system

5.1 Previous work

In previous work, Haug [9] has claimed that precipitation of zinc ferrite spinels in Fe doped ZnO is possible by performing two separate heat treatments on samples prepared by the powder synthesis route. It was also shown that IDBs are present in samples that are heat treated at 1400 °C. In the second, spinel forming heat treatment, the temperature was set to 1000 °C. The spinels had a orientation relationship to the ZnO grains where the diagonal plane {1 1 1} of the spinel grains were perpendicular to the c-axis direction [0 0 1] in the ZnO grains.

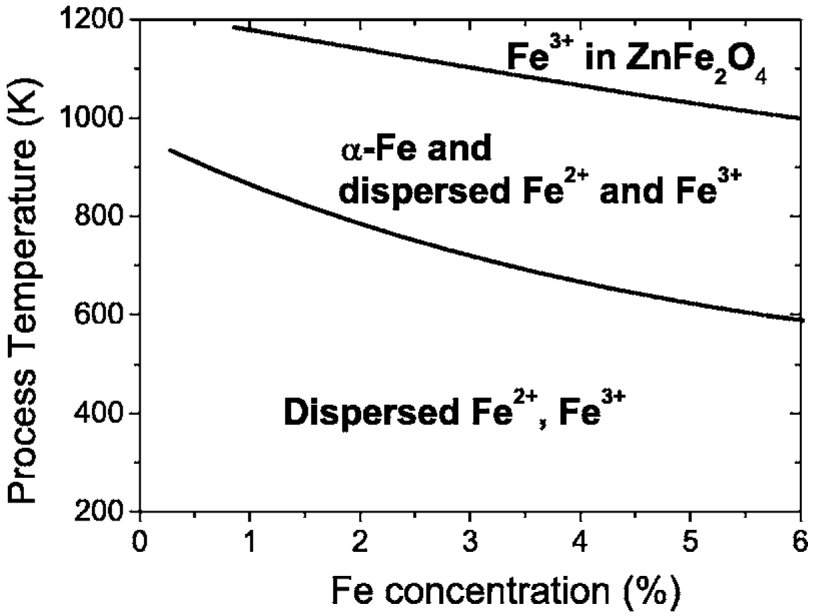

Figure 5.1: Phase diagram showing the formation temperature of zinc ferrite spinel as a function of iron concentration in a matrix of ZnO. The concentration is given as at% with oxygen included. The phase diagram is adopted from [38].

In work done by Degterov et al. [11], a binary phase diagram of ZnO - Fe_2O_3 was provided. In this thesis, the phase diagram was used as an example when explaining the concept of solid state precipitation, and can be found in a modified version in figure 2.1 in the Theory chapter. Furthermore, the phase diagram was appreciated

when choosing the annealing temperatures and when samples were interpreted. The properties of the phase diagram were cross-checked with results from another paper and found to be in agreement [39].

In another study, Fe ions were implanted in a ZnO single crystal with varying temperatures and fluences [38]. Based on the results from the study, a phase diagram of iron dissolved in ZnO bulk crystals was obtained, this phase diagram is shown in figure 5.1. From this we see that the spinel structure is stable above 1200 K In the concentration range shown. However, at higher concentrations the spinel structure can form at temperatures of about 1000 K. Below the spinel forming temperature, it is clamied that Fe ions and iron nanocrystals (α- Fe) are dispersed in the single crystal. In another study, by the same authors, it was shown that the precipitates have the same crystallographically orientation to the ZnO crystal as in Haug's [9] samples. The spinels were found in excess near and on the surface of the ZnO crystal. This was explained by iron diffusion towards the surfaces of the single crystal at elevated temperatures [40].

5.2 Experimental

Samples in this study were prepared by cutting the 10 mm × 10 mm × 0.5 mm single crystal into four 5 mm × 5 mm × 0.5 mm ZnO single crystals. The cutting was performed on a microsaw from Technoorg-Linda. Subsequently, the single crystals were embedded in oxide powders containing iron and zinc, using one 5 mm × 5 mm × 0.5 mm single crystal per sample. The precursor powder and single crystal are utterly described in the method chapter 4.1.

Diffusion couple samples with ZnO single crystals give a slightly different microstructure than what is depicted in figure 2.2 in the Theory chapter as we initially don't have grain boundaries inside the single crystal, and the single crystal is large relative to typical diffusion length. However, the single crystal could be considered a large ZnO grain, and the same working principle for formation of precipitates is expected to apply. In addition, the diffusion couple synthesis route has some advantages compared to mixing of powders. Since the crystal is large relative to the typical diffusion length, thermodynamic equlibrium may not be reached throughout the system. This will result in a concentration gradient, thereby allowing the study of differnt compositions in one sample.

In all samples, except DC 7 and DC 8, the cation ratio of the surrounding powders was the same as in the $ZnFe_2O_4$ (ZFO) spinel phase, that is 2/3 iron and 1/3 zinc. All the samples prepared in this system are listed in table 5.1 and illustrated schematically in figure 5.2. The powders and single crystal were pressed into pellets, and annealed at 1400 °C. This facilitates the diffusion of Fe from the surrounding powders into the embedded ZnO single crystal, and Zn diffusion out of the single crystal.

In this chapter all compositions are given as cation ratios. That is:

$$C_{Fe} = \frac{N_{Fe}}{N_{Fe} + N_{Zn}} \tag{5.1}$$

$$C_{Zn} = \frac{N_{Zn}}{N_{Fe} + N_{Zn}} \tag{5.2}$$

where C is molar fraction, and N is number of moles. The ratios are multiplied by 100 to obtain cation ratio in percent.

Table 5.1: Showing samples prepared in this system and the respective variables.(Sample DC 1 was an inherited sample and is not included in the discussions in this work.)

Sample	**Heating rate (°C/hour)**	**Annealing time (Hours at 1400 °C)**	**Cool down rate (°C/hour)**	**Cation rato of iron in powders (%)**	**Remarks**
DC 2	150	8	150	66.7	Most investigated sample.
DC 3	150	8	Quenched	66.7	Made to investigate structure at 1400 °C.
DC 4	150	14	150	66.7	Added Pt marker to keep track of original surface.
DC 5	300	8	300	66.7	Annealed under pressure to avoid cracking.
DC 6	200	24	Quenched	66.7	Excess of spinel powders surround the single crystal.
DC 7	200	26	200	20	Made to probe diffusion related challenges.
DC 8	150	48 (at 1000 °C)	150	≈ 5 (in the single crystal)	Re-heat treatment of DC 2.

As seen from table 5.1, DC 2, DC 4, DC 5 and DC 7 were slowly cooled in the furnace, whereas DC 3 and DC 6 were quenched by dropping in water. When a sample is quenched the temperature drops fast and phase transitions are inhibited. Thus, the atomic configuration is somewhat frozen at the temperature the sample was quenched from. This allows for investigation of the sample as it was at 1400 °C. The quenched samples were made because there were features in the slowly cooled samples that would have been difficult to interpret if processes were not going on during the cooling.

In DC 2, the surrounding powders were a mixture of hematite and zincite. During the annealing, this powders transformed to the ZFO phase. For samples DC 3, DC 4, DC 5 and DC 6, pre-made ZFO powders were used as surrounding powders. The ZFO powders were made by adopting a synthesis route described by Haubacks et al. [41]. The motivation for pre-making ZFO powders was to make the high temperature processes simpler, in the sense that, when the starting powders consist

of hematite and zincite, the formation of the ZFO phase in the surrounding powders will happen in addition to diffusion processes including the single crystal.

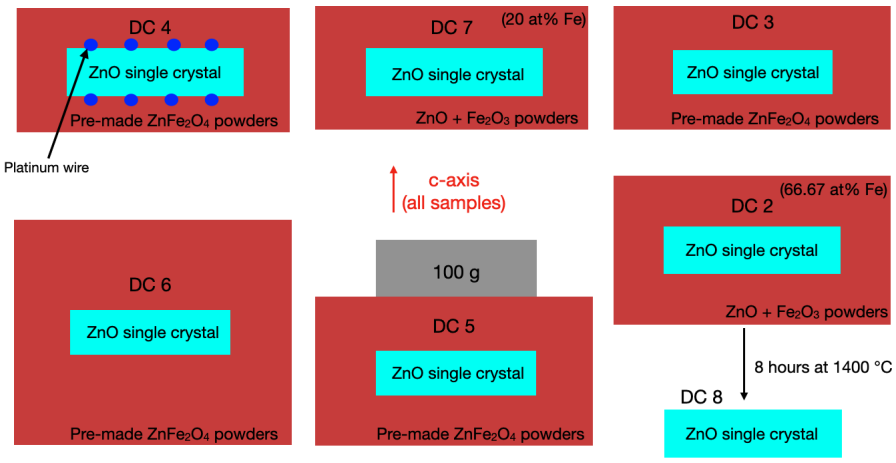

Figure 5.2: Schematic cross section drawings of the prepared samples. The c-axis in the single crystals is directed upwards for all samples as illustrated by the red arrow.

Sample DC 4 was purpose-made to expose the original single crystal surface after annealing. This was done by placing platinum wires on a pre-pressed bed of ZFO powders, and planting the single crystal on these wires. Platinum wires were placed on the top surface of the single crystal prior to addition of more ZFO powders. Then the sample was pressed to a pellet and annealed.

Sample DC 8 was prepared by extracting a piece of the single crystal from sample DC 2 after it was annealed at 1400 °C. Then, this single crystal piece was annealed in solitary condition for another 48 hours at 1000 °C. That is, without any iron source, except for the iron soluted in the single crystal.

5.3 Results and discussions

The results in this work are mostly of qualitative nature. This makes condensation of the results into tables and curves difficult. The system is also quite complex with many features that have to be presented and discussed to get the full picture. Unfortunately, this contribution is far from sufficient for such a full picture to be drawn. To make the presentation somewhat clear and comprehensible, the interpretation of the experimental results is given right after the main observations have been presented. An attempt has been made to split the findings into sections that can be treated more or less independent of each other. The division is schematically shown in the overview sketch in figure 5.3, and as the quenched samples were different from the slowly cooled samples in some regions, both cooling rates are sketched. Terminologies and sample area names are included on the figure.

The outer dark red rectangles in the overview sketch in figure 5.3 illustrate the surrounding ZFO phase and the bright and dark needle-like features embedded in the region symbolize ZnO grains being partly evaporated (dark tail). This whole area is referred to as Area 1. The region located between Area 1 and the single crystal is Area 2. This region is formed during the annealing of the samples, and

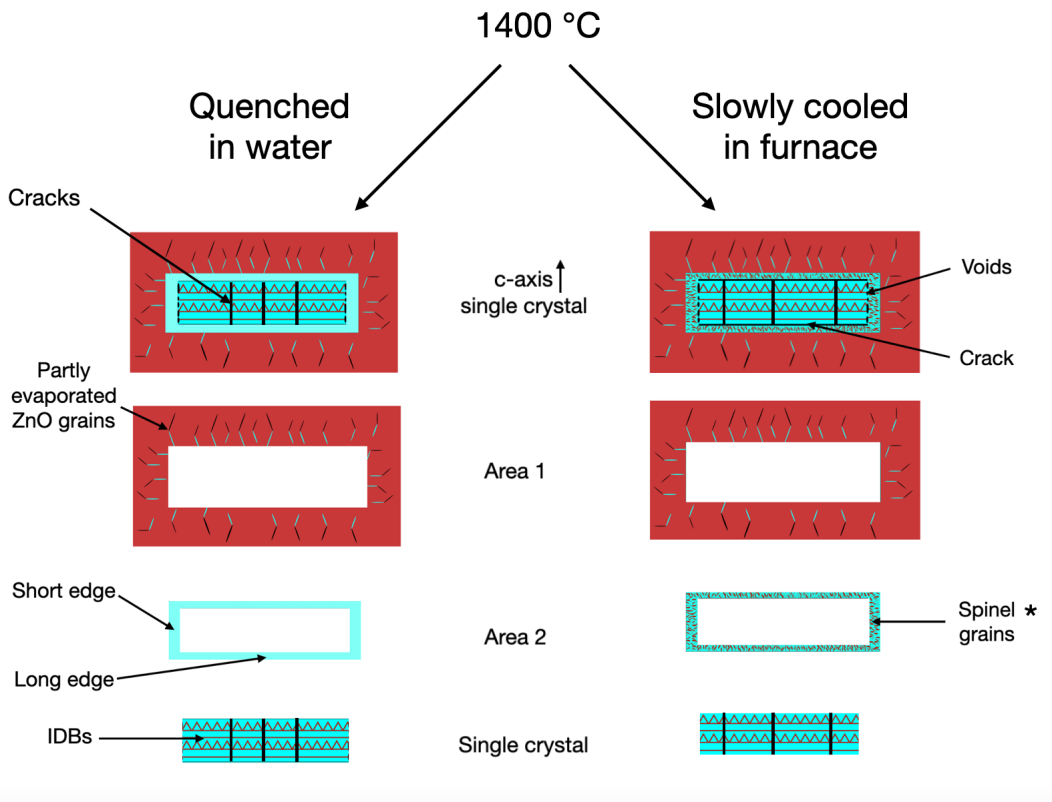

Figure 5.3: Show the division of samples into regions named Area 1, Area 2 and single crystal. The difference between quenched sample vs slowly cooled is illustrated schematically. "Spinel grains" is marked with an asterisk as this feature was exclusively seen in slowly cooled samples. The other labelings are valid for both cooling rates.

is some kind of crystallization zone that grow outwards from the single crystal. We can say this because the platinum markers in sample DC 4 were located within, and embedded by Area 2. The platinum markers are chemically inert with respect to the reactants and doesn't move due to the lack of chemical potential, thus the direction of the crystallization growth must extent out from the single crystal. In the slowly cooled samples, ZFO precipitates were seen embedded in a matrix of ZnO in Area 2. The precipitates are depicted as red elongated dots in figure 5.3. However, in the thin quenched sample DC 2 a single phase iron-rich ZnO phase was present in Area 2. Between Area 2 and the single crystal, black dots are drawn on the short edge, and black lines are drawn on the long edge. The dots illustrate voids, and the lines illustrate cracks. In the single crystal, a red zig-zag pattern is drawn to symbolize pyramidal IDBs, and red lines to depict basal IDBs. Cracks observed in the single crystal are drawn as black lines. The synthesis results, the transition from Area 2 to the single crystal and Sample DC 8 will be explicitly discussed in separate sections.

We will also make one assumption that is adhered to throughout this chapter, that is: *The assumption: DC 3 represents the structure in DC 2 before the cooling starts, and DC 2 represents the microstructure in DC 3 if it was cooled down slowly.*

The assumtion is justified by the successful quenching of DC 3, and that the annealing dwell time at 1400 °C is the same for both samples. Additionally, no difference was found between samples prepared with the pre-made spinel powders

versus ZnO and Fe_2O_3 as surronding powders. Therefore all samples, except DC 7 and DC 8, are considered equal in terms of composition.

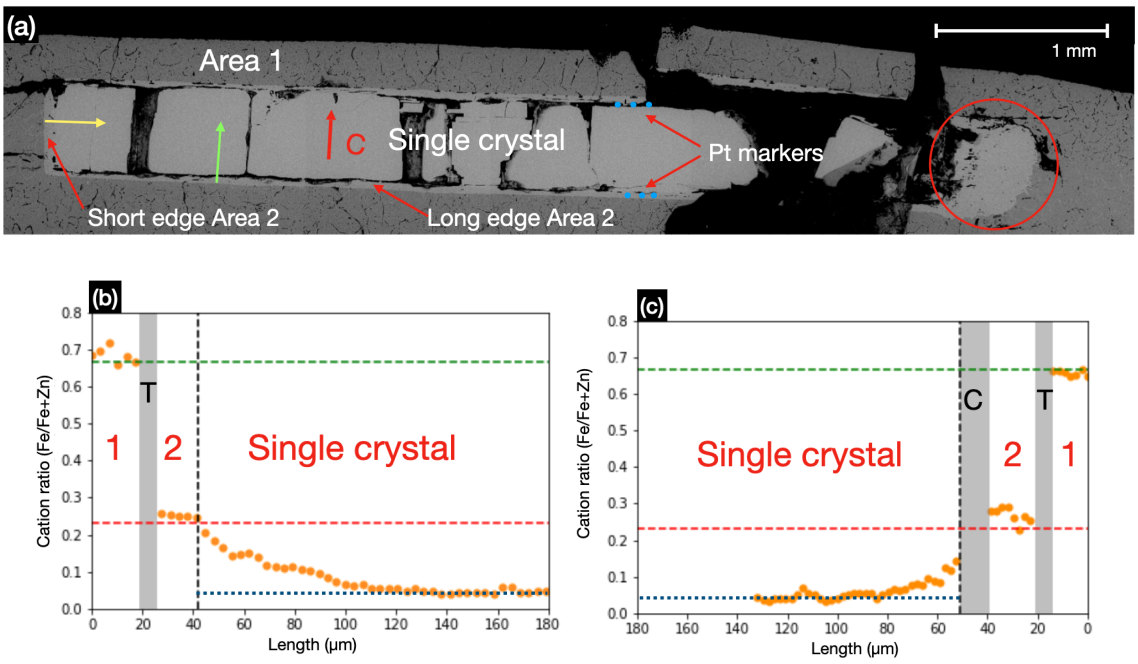

Figure 5.4: (a) Overview SEM BSE image of sample DC 2. Same terminologies are used here as in figure 5.3. (b) Line scan acquired from sample DC 3 in the direction corresponding to yellow arrow. (c) Line scan acquired from sample DC 3 in the direction corresponding to green arrow. The green dotted line is the spinel cation ratio, the red dotted line is the solubility limit of Fe in zincite, and the blue dotted line is 4 at % Fe, where both gradients flattens. "T" depicts phase transitions and "C" depicts cracks.

Figure 5.4 show an SEM BSE overview image of sample DC 2 labled with the same terminologies as in figure 5.3. The green and the yellow arrows mark two directions frequently referred to in the following discussions, that is, normal to the c-axis direction (yellow) and parallel to the c-axis direction (green). In addition, readers are cindly asked to notice the naming of the two edges. That is, long edges which corresponds to the $(0\,0\,1)$ and $(0\,0\,\bar{1})$ surfaces of the single crystal, and the short edges which corresponds to $(1\,1\,0)$, $(1\,\bar{1}\,0)$, $(\bar{1}\,\bar{1}\,0)$ and $(\bar{1}\,1\,0)$ surfaces of the single crystal. No attempt was done to mutually separate between the directions and surfaces within each of these two sets of planes. Thus, we will only separate between the long edges, which is perpendicular to the green arrow and the short edges which is perpendicular to the yellow arrow. The location of the platinum markers in DC 4 are schematically transferred to the SEM BSE image of DC 2, this is also assumed to be the original surface of the single crystal on the long edges. No markers were placed on the short edges of DC 4. The separated sample piece marked with a red circle had extensive growth of Area 2 type of microstructure. A possible explanation for this observation is discussed in the Area 2 section 5.3.2, and an SEM BSE image serie from this piece is given in the appendix figure 9.1. The dark/black contrast seen in figure 5.4a is vacuum, clearly showing cracks inside the single crystal.

The two line scans shown in figure 5.4b and 5.4c are acquired from sample DC 3. Based on The assumption are these compositions equivalent to the compositions in DC 2 before the cooling. The directions of the line scans corresponds to the yellow arrow for figure 5.4b and to the green arrow for figure 5.4c. The scans were obtained by taking several EDS quantitive measurements along a straight line with the same spot size and spacing between measurements. The labeling "1" and "2" corresponds to Area 1 and Area 2 respectively. The spinel ratio is labeled as a green horizontal dotted line, and we see that Area 1 has this composition on both edges. The grey shading indicate regions with phase transitions and cracks, measurements from these regions were considered highly uncertain and were removed. "T" depicts phase transitions and "C" depicts cracks. The plateau in Area 2 show a Fe concentration that is somewhat above the solubility limit of Fe in ZnO at 1400 °C reported in literature for the line scan in figure 5.4c. The reported maxium solubility of iron in zincite is shown as a red horizontal dotted line. The quantifications from the single crystal render a Fe concentration gradient spanning from the end of Area 2 and into the single crystal. It can noticed that the concentration gradient in the single crystal is continuous with the solubility limit of iron in zincite in the normal to c-axis direction (figure 5.4b). As opposed to the concentration gradient parallel to the c-axis (figure 5.4c), we see that this gradient is clearly not continuous with the red dotted line. At 4 at % Fe, a blue dotted line is drawn, at this Fe concentration both gradients flattens.

In the middle of the single crystal the average iron composition in DC 3 was 2.9 at% Fe. This value was obtained by taking 20 EDS quantifications along a straight line in the middle of the sample. The standard deviation in the measurements was 0.6 at% Fe.

The black dotted line in figure 5.4c represent the assumed original surface of the single crystal, based on observations in sample DC 4. However, as no markers were placed on the short edges of the samples, the black dotted line in figure 5.4b must be considered an educated at the position of the original surface of the single crystal on this edge. We assumed that the original single crystal surface is the end of the plateau in Area 2. However, as we will see later, it is not straight forward to determine the exact interface between Area 2 and the single crystal in this region.

Figure 5.4 will be frequently referred to in the following discussions.

5.3.1 Synthesis

Before we interpret the observations from the regions shown in figure 5.3 and 5.4 we will take a small step back and briefly discuss the results of the synthesis. Some samples can already be checked out, and this will hopefully make the the following discussions somewhat clearer.

Sample DC 5 was considered to be unsuccessful in regard to reducing crack formation, and was not investigated further. Sample DC 4 successfully showed that Area 2 extend out from the single crystal and revealed the original single crystal surface. However, DC 5 was not further investigated.

Sample DC 7 was prepared with 20 at% Fe. The excess of Zn in the surrounding powder was intended to inhibit Zn from diffusing to fast out of the single crystal, as this was suspected of causing Kirkendall voids [42] and thus hinder the diffusion of iron into the single crystal. However, this route led to severe crack formation in

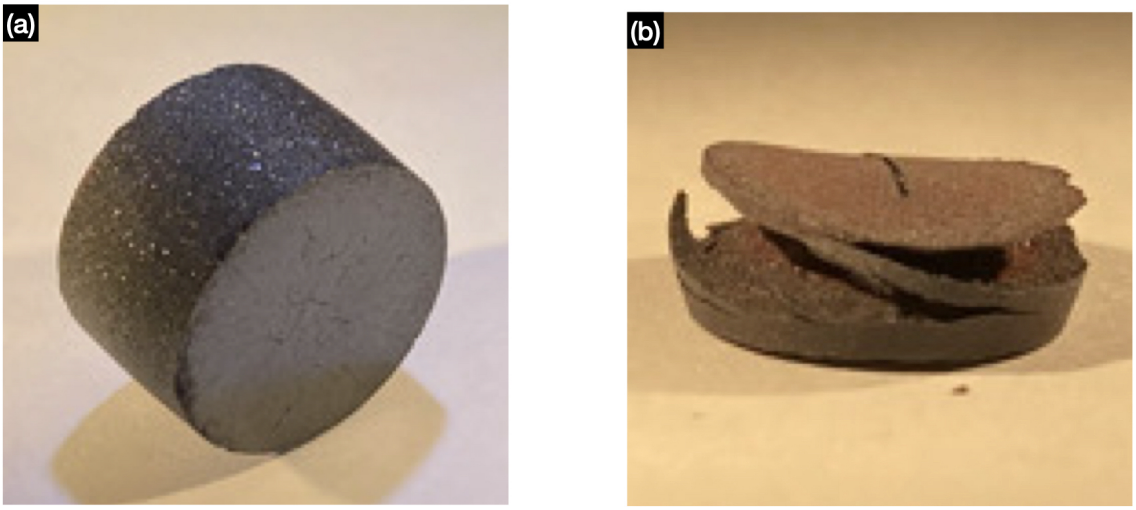

Figure 5.5: Comparison of DC 6 (a) and DC 7 (b) shows a preference for single phase ZFO surroundings of the single crystal for obtaining compact samples as displayed for DC 6.

Area 1 and poor adhesion to the single crystal, resulting in the single crystal being detached from Area 1 after annealing. This consequently gave low iron concentration in the single crystal. The optical micrograps of DC 6 and DC 7 shown in figure 5.5 cleary demonstrate a preference for single phase ZFO surroundings for obtaining compact samples. However, DC 7 had eye-catching round features on the surface of the single crystal which will be used in the argumentation when we later consider preferential zinc-self diffusion paths and vacancy cluster formation in the single crystal.

5.3.2 Area 1

The purpose of this region is to provide Fe to diffuse into the ZnO single crystal. As the initial precursors in this region were hematite and ZnO powders in the spinel ratio, it is no great surprise that this area mostly consists of the ZFO phase. However some ZnO grains are also present, as shown by the SEM BSE image in figure 5.6a. These grains were not expected, but could be explained by the reduced solubility of Zn in the spinel phase as temperature increases. The needle-like shape could then be the result of Zn precipitating and diffusing to grain boundaries of the ZFO phase. As these ZnO grains were found in all samples, errors in weighing out powders seems less likely. However, we can not exclude the possibility of precursor powders having absorbed water, and therefore having a composition slightly off the spinel ratio. If so we would also expect a needle-like shape as the excess Zn would end up in-between the growing ZFO grains. Finally and most likely, the diffusion process when zinc is diffusing from the single crystal and into Area 1, whereas iron is diffusing from Area 1 and into the ZnO single crystal, could give excess of zinc in Area 1 after the annealing compared to before the annealing.

In the SEM BSE in figure 5.6a, ZnO grains appear bright due to mass contrast, while the black tails are empty space. The empty space tails are seemingly a results of Zn evaporation in regions near the surface of the pellet, and we found by compar-

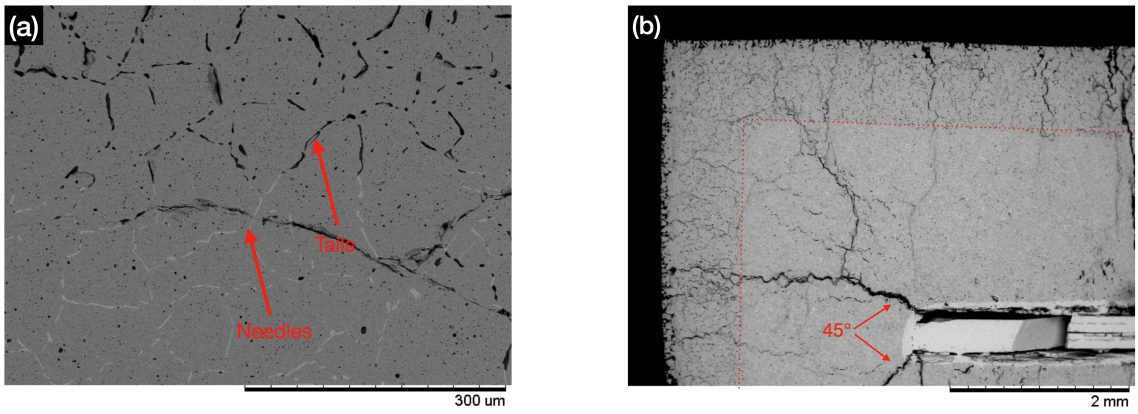

Figure 5.6: (a) SEM BSE image of the needle-shaped ZnO grains. The image is taken from Area 1 in sample DC 2. (b) Overview SEM BSE image of DC 6 showing evaporation of Zn and 45 °cracks.

ing DC 2 and DC 6 that the extend of evaporation increases as the annealing time is increased. The evaporated region in sample DC 6 is outlined with a red line in figure 5.6b.

Some cracking was also seen in this area, with the most prominent at 45° reaching out from where the short and the long edges meet. The cracks are marked with red arrows in figure 5.5b. In literature one finds that such cracks often are related to shear stress. For reasons that will become clear in the next chapter, this may very well explain our observations as well.

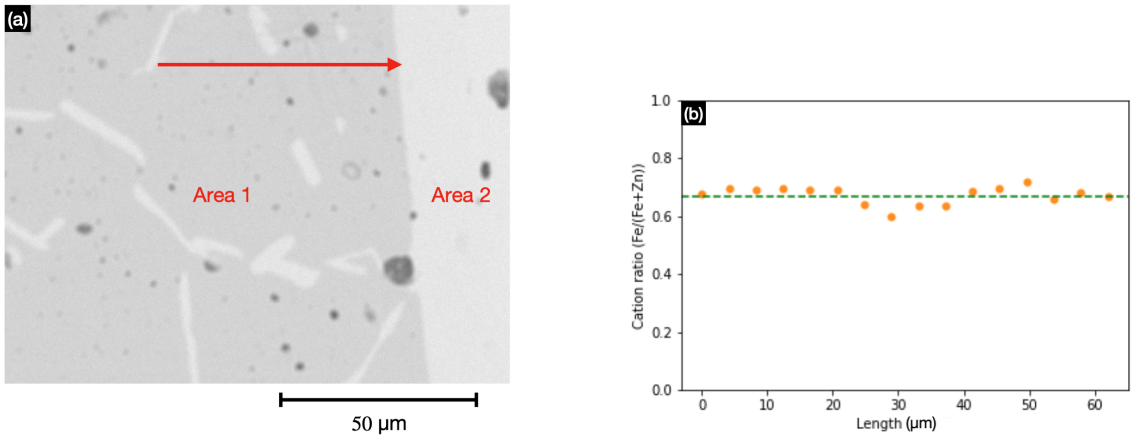

Figure 5.7: (a) SEM BSE image of Area 1 in the quenched sample DC3. The transition from Area 1 to Area 2 can be seen on the right side in the image. The red arrow illustrate where line scan in figure (b) is acquired. (b) Iron concentrations acquired by EDS along the red line. The green dotted line is the theoretical cation ratio in the ZFO phase.

In figure 5.7a an SEM BSE image from the quenched sample DC 3 is shown, and a corresponding compositional line scan is shown in figure 5.7b following the red arrow depicted in figure 5.7a. The line scan was obtained as described for the line scans in figure 5.4b and 5.4c. The image and line scan were acquired close to the

transition between Area 1 and Area 2 on the short edge, and would therefore show if there is any diffusion gradient. As seen from the line scan plot, no concentration gradient was present. This is no surprise, as the ZFO phase in this region is already saturated by zinc. One can notice the dip in the middle of the curve in figure 5.7b. This is probably caused by contributions from the ZnO grain close to the red line in figure 5.7a. This emphasizes the importance of accounting for the large volume where EDS x-rays are generated, when analyzing EDS data quantitatively.

5.3.3 Area 2

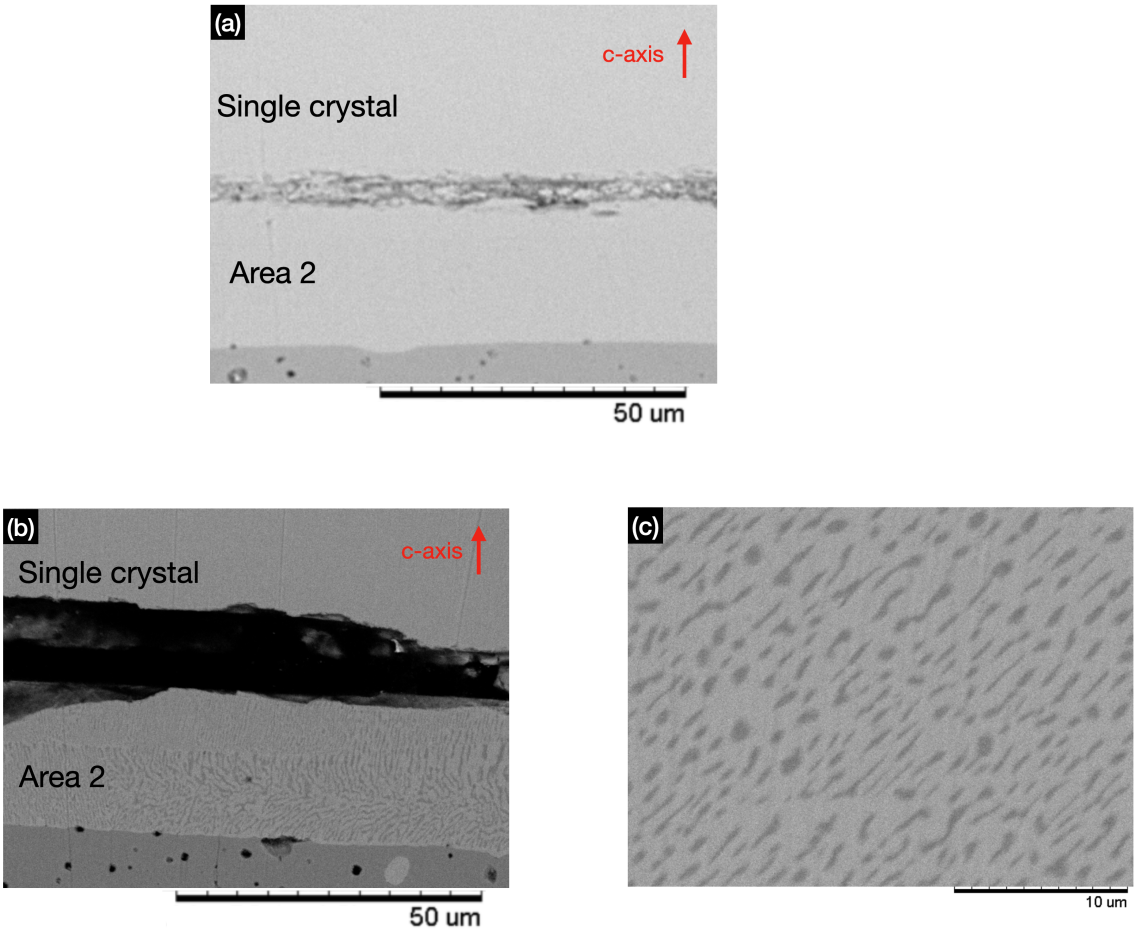

Figure 5.8: SEM BSE images comparing Area 2 in DC 2 and DC 3. (a) Show the transition between all three regions (Area 1, Area 1 and single crystal) in DC 3, however focus should be placed on Area 2 where a single phase ZnO structure with high soluted Fe concentration is observed. (b) Show a similar region in the slowly cooled sample DC 3. We see from the image that precipitates are present in Area 2. (c) Magnified image of the precipitates in Area 2 of the slowly cooled sample DC 2.

In this section, sample DC 3 and sample DC 2 are considered and compared. We will first consider Area 2 in the quenched sample DC 3 which is labeled Area 2 in figure 5.8a. In this region a single phase structure was observed, and quantitative EDS measurements gave Fe and Zn in the ratio 27 at% and 73 at% respectively. The Fe concentration is somewhat higher than what we expected to find, as the phase

diagram (cf. figure 2.1) give a solubilty limit of ≈ 23 at% Fe in ZnO at 1400 °C. However, we have already seen that Zn tend to evaporate at high temperatures, and from the SEM BSE image in figure 5.8a, we see that a small crack has developed between Area 2 and the single crystal. It is therefore assumed that Zn could evaporate from the surface of the crack, and thus skew the Fe quantification. This hypothesis is strengthen by considering the shape of the EDS line scan in figure 5.4c, as the Fe concentration is closer to the predicted value of ≈ 23 at% Fe when measurements are acquired close to the transition region between Area 1 and Area 2. The crack seen in figure 5.8a causes the highly uncertain measurements between Area 2 and single crystal in figure 5.4c, whereas the other highly uncertain measurements from figure 5.4c stems from the transition between Area 2 and Area 1 that can be seen in the lower part of figure 5.8a.

However, we can notice that this structure is similar to what is sketched in figure 2.2C in the Theory chapter as we have ZnO with maximum Fe doping concentration, and as the sample is quenched. If we now "slowly cool" DC 3, which we can do based on The assumption, by investigating DC 2, we see that Fe-rich precipitates are covering this entire region as shown the SEM BSE image in figure 5.8b. This type of structure is similar to what is sketched in figure 2.2D, and XRD analysis showed that these grains indeed were spinels. In figure 5.8c an SEM BSE image show the shape of the ZFO precipitates, and the continuous matrix of ZnO embedding the ZFO precipitates. TEM EDS quantification gave a Fe concentration of ≈ 4 at% in the ZnO matrix, whereas the precipitated spinel phase had the expected spinel ratio of ≈ 66 at% Fe.

Based on this, we concluded that the following reaction takes place during cooling:

$$\mathrm{ZnO}_{27\mathrm{at\%Fe}} \rightarrow \mathrm{ZnO}_{4\mathrm{at\%Fe}} + \text{ZFO precipitates} \tag{5.3}$$

and moreover that the system obeys the predicted model from figure 2.2. We can also say that this is a fast reaction, as it is taking place during cooling of the samples. Actually, even in the thick quenched sample DC 6, some Fe-rich particles were found in Area 2. The thickness makes the quenching less effective towards the inner parts of the sample, and therefore some Fe atoms manage to precipitate before the sample is throughly cooled, thus indicating that this is a very rapid reaction.

Figure 5.9a and 5.9b shows HAADF STEM and TEM dark-field image from Area 2 in sample DC2, respectively. Due to Z-contrast in HAADF STEM images, the spinel precipitates appear to be darker grains, and the ZnO grains are the brighter areas. The average ZFO particle size in this region was ≈ 1 µm in length, and ≈ 100 nm in width, however with large variations. The dark-field TEM image was acquired in the same region as the HAADF STEM image and by using the marked reflections in the diffraction pattern in figure 5.9c. More diffraction contrast is expected from the dark-field TEM image and thus information related to grain orientations can be obtained. We see that little Z-contrast is left as we can no longer distinguish between ZFO and ZnO grains. However, there seems to be an orientation relationship between grains in this region, as the Bragg conditions shown in figure 5.9c, are satisfied for more or less the whole region.

In order to further investigate the orientation relationship between ZnO and spinel grains, diffraction patterns were acquired from adjacent grains at the same sample tilt. The TEM bright-field image in figure 5.10a shows the investigated

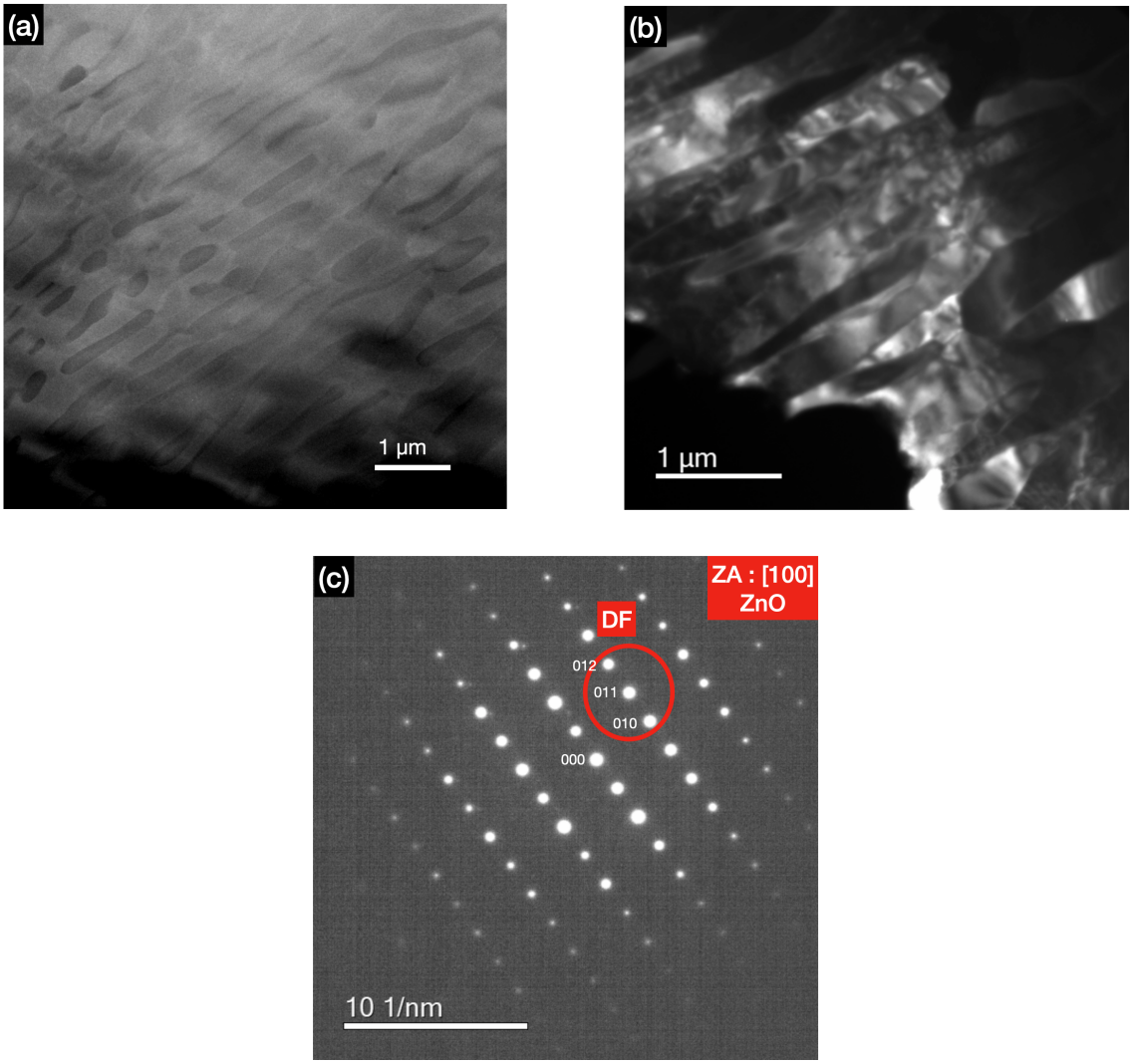

Figure 5.9: (a)HAADF STEM image of Area 2. Spinel particles are dark due to Z-contrast. (b) DF TEM image of Area 2 with more diffraction contrast. (c) Diffraction pattern showing reflections chosen for imaging in figure 5.7 (b)

grains and circles are drawn where the selected area diffraction aperture was placed. The diffraction pattern from the spinel grain was indexed and found to be a [110] projection. This means that diagonal of the cubic spinel unit cell has a direction as depict by the white arrow in figure 5.10b. The projection of the adjacent ZnO grain was found to be [100], and the c-axis is therefore oriented as shown by the white arrow in figure 5.10d. In the overlapping diffraction pattern in figure 5.10c the relationship is evident and one can clearly see how the diagonal of the spinel grain lines up with the c-axis of the ZnO grain, giving the orientation relationship:

$$[1\,0\,0](0\,0\,1)\mathrm{ZnO} \;||\; [1\,1\,0](1\,1\,1)\mathrm{ZFO} \tag{5.4}$$

however with a slight mismatch that is most clearly seen by following the ZnO c-axis marked by red arrows in figure 5.10c.

One may argue that this orientation relationship is expected, as the [111] projection in the cubic ZFO unit cell has a three-fold rotation symmetry, and the [001]

projection in the hexagonal ZnO unit cell has a six-fold rotation symmetry. These symmetries are closely related as three symmetry points are common, and therefore a preferential growth of spinel grains in the given orientation relative to ZnO is anticipated. The same relationship was observed in all investigated grains. Also in previous work done by Haug [9] and Zhou et al. [38], the same orientation relationship was found.

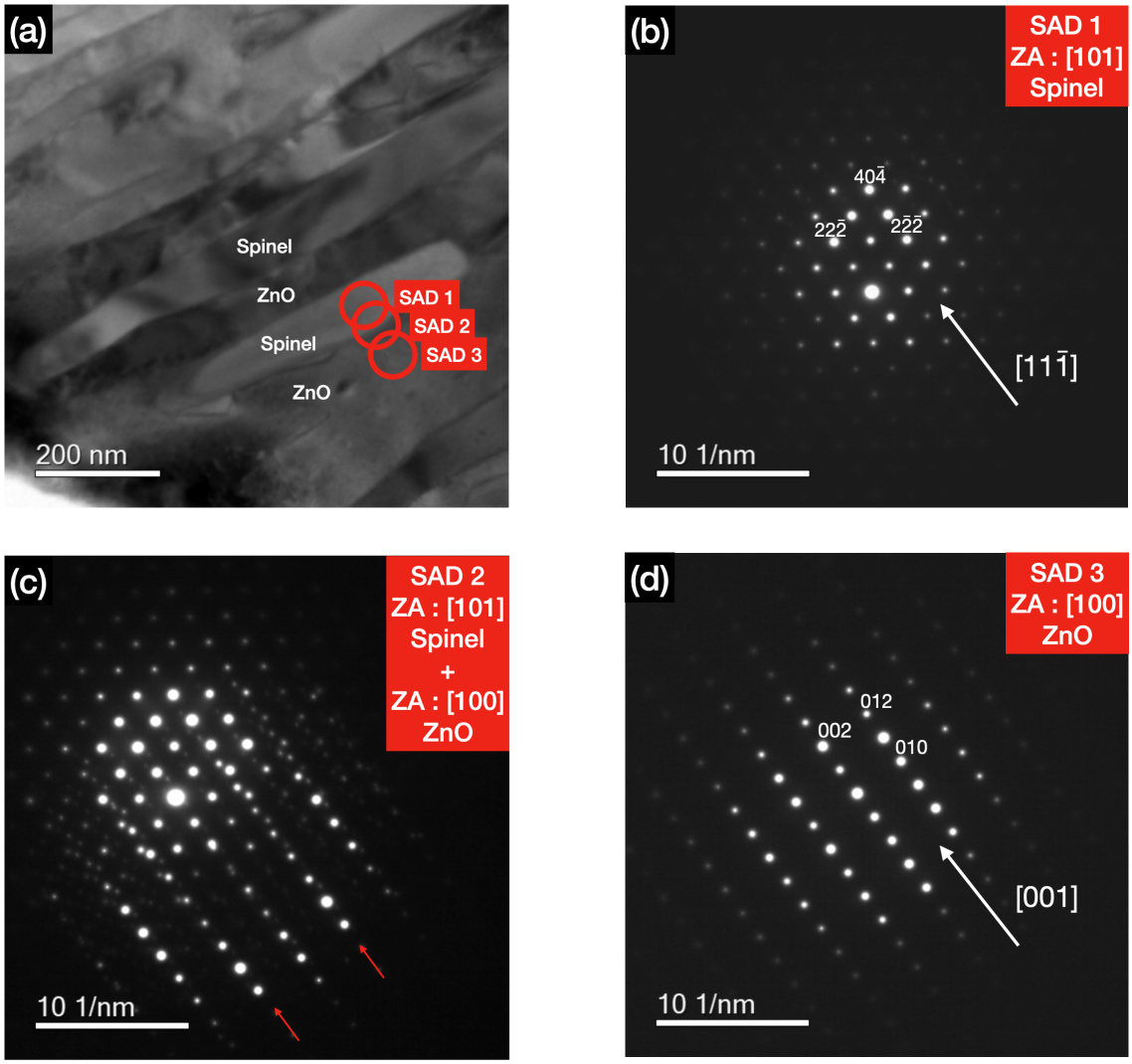

Figure 5.10: (a) Overview of region where diffraction patterns are aquired from. (b) Diffraction pattern from the spinel grain, the zone axis is [110]. (c) Overlapping diffraction pattern, catching both the spinel and the ZnO grain. (d) Diffraction pattern from the ZnO grain, the zone axis is [100].

By examining convergent electron beam diffraction (CBED) patterns, small variations in the orientation of ZnO grains within the same region were found. These variations can be explained by structural adjustments when a precipitated particle grows in a host matrix, and possibly related to the slight mismatch in alignment between the c-axis of ZnO and the diagonal of the spinel.

Another observation is that the extent of Area 2 is considerably wider on the short edge than on the long edge of DC 2. In addition, the short edges of Area 2

were always coherent with the single crystal, whereas the long edges of Area 2 and the single crystal were more or less always separated by cracks. These observations are presumably related to the Zn self-diffusion in the single crystal, and preferential diffusion paths for Zn and vacancies. However, in literature, it is often claimed that the zinc self-diffusion is isotropic [31].

This thesis is not a dedicated diffusion study, but in the following we will attempt to interpret the microstructure observations by means of zinc-self diffusion and vacancy-cluster formation in the single crystal.

The fact that Area 2 is considerably wider on the short edges than the longs edges suggests that Zn self-diffusion is somewhat more successful in the direction towards the short edges. If more Zn atoms are provided to the short edges than the long edges, growth and crystallization should be more efficient there. In addition, lined-up voids were always seen on the short edges of Area 2 as shown in figure 5.11a. These voids are believed to arise from the Kirkendall effect [42], which indeed is a result of one species diffusing faster than the other across a boundary. This result in accumulation of vacancies and eventually voids on the side having the fastest diffusing species. Therefore, it is proposed that Zn is diffusing faster out of the single crystal than Fe is diffusing into the single crystal in the normal to c-axis direction. Such voids were never seen in the long edges, which strengthen the hypothesis. The location of the presumed to be Kirkendall voids relative to the spinel precipitates, indicate that Area 2 type of structure can be found in regions initially being a part of the single crystal. The explicit transition indicated by a green circle in figure 5.11a is probed in section 5.3.5.

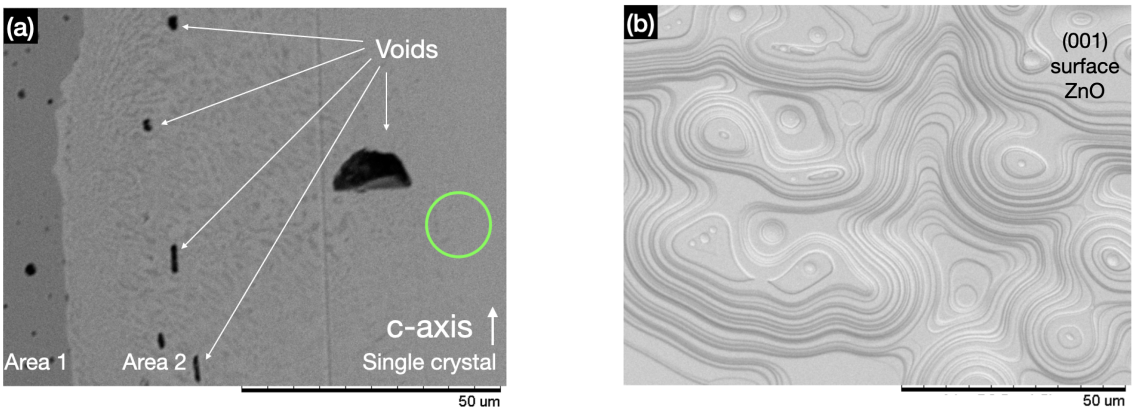

Figure 5.11: (a) SEM BSE image showing that the short edge on sample DC 2 is coherent with the single crystal and have lined up voids. The green circle indicate the location of the region being probed in chapter 5.3.5. (b) SEM BSE image assumed to show evaporation of Zn from the (001) surface of DC 7.

However, it is known that vacancy clusters form at elevated temperatures in ZnO. These clusters are more stable than vacancies, and form in excess at the (001) surface of ZnO [30], which correspond to the long edges in our terminology. In sample DC 7 irregular circles were seen on the (001) single crystal surface and are assumed to be related to this effect. The features are shown in the SEM BSE image in figue 5.11b. By examining this image we could easily imagine that these features could eventually result in open cracks and as a consequence stop the diffusion of iron into the single crystal. If the vacancy clusters are responsible for stopping the

diffusion in this direction, the zinc-self diffusion may still be isotropic as claimed in literature.

By revisiting the EDS line scans from figure 5.4b and 5.4c, we see that these observations are in agreement with Fe concentration gradient being continuous with the red dotted line (showing maximum solubility of Fe in zincite) in the normal to c-axis direction (yellow arrow) and discontinuous in the parallel to c-axis direction (green arrow). These observations indicate that the crack on the long edge opened up while diffusion was still going on. One can notice that the gradient extends further into the single crystal in the normal to c-axis direction. This is as expected since the short edge was coherent with the high iron reservoir in Area 1 throughout the full heat treatment.

According to these observations, samples should be prepared with ZnO single crystals having the a-axis perpendicular to the large square surface of the single crystal plate (cf. figure 4.1), as opposed to c-axis in our single crystals, in order to form much of the structure seen in Area 2. Said differently, short edges must be large compared to long edges, to obtain large regions of Area 2, as growth of this structure is more efficient from the short edges. This is emphasized by the separated sample piece marked with a red circle in the overview SEM BSE image in figure 5.4. As this piece ended up having a geometry as described, and essentially consisted of only Area 2 type of structure. In the appendix figure 9.1, an SEM BSE image series from this piece is shown.

It was also found that cracks on the long edges were more opened up in the slowly cooled sample DC 2 than the quenched sample DC 3. This can be verified by revising figure 5.8a and 5.8b. As both samples are expected to experience the same thermal contraction, the volume change related to forming the ZFO precipitates inside the matrix of ZnO was suspected of causing the cracks to open. The difference in volume per cation for pure ZnO vs pure $ZnFe_2O_4$ was calculated to be < 1 %, thus this explanation seems less likely. However, a significant change in c-axis length is expected when Fe is incorporated into the ZnO matrix [43], and presumably, a contraction of c-axis when Fe leaves the ZnO matrix. This shrinking is suggested as an explanation for the cracks being open in the slowly cooled sample and not open in the quenched sample, as we expect the Fe atoms to essentially remain dissolved when samples are quenched. In addition the contraction may cause shear stress in the entire Area 2 region, and thus suspect of causing the 45 °cracks seen in figure 5.6b.

Figure 5.12 shows the result of powder XRD from Area 2 and the single crystal in the quenched sample DC 3. We see that the 002 peak of ZnO is a doublet with broadening towards lower angles. This corresponds to a increase in spacing. Since the position of this peak is only dependent on the c-axis, this result indicates that the length of the c-axis increases with Fe concentration in ZnO, and thus supports what is claimed in litterature [43]. The discussion regarding why this extension can be present despite that tetrahedral 4-coordinated Zn(II) and tetrahedral 4-coordinated Fe(II) have approximately the same ionic radii, and tetrahedral 4-coordinated Fe(III) has a lower ionic radii than tetrahedral 4-coordinated Zn(II) [44] was not considered in this work. In addition, as Area 2 is small (20-25 µm) it proved to be difficult to precisely separate out powders from Area 2 for XRD analysis.

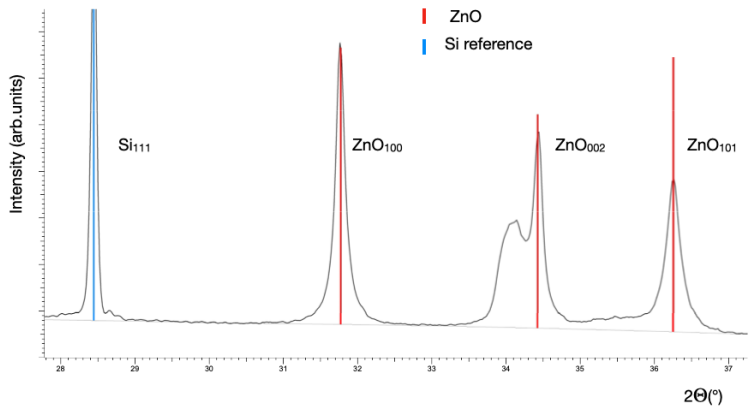

Figure 5.12: Diffractogram from the single crystal showing variations in c-axis presumed to corresponding to Fe doping concentration.

5.3.4 Single crystal

In this section we will discuss the results from the single crystal in sample DC 2. As shown in the concentration plots in figure 5.4b and 5.4c a Fe concentration gradient is present about 55 µm into the single crystal in the direction parallel to the c-axis (green arrow) and about 95 µm in the direction normal to the c-axis (yellow arrow). The gradient seems to flatten out at a concentration of ≈ 4 at% Fe in both directions. In this section we probe the Fe concentration gradient in the single crystal in the parallel to c-axis direction.

As seen from the TEM weak-beam bright-field images in figure 5.13, the heat treatment at 1400 °C resulted in formation of IDBs in the single crystal. Both pyramidal and basal inversion domains were present, and the spacings between domains changed as we probed deeper regions towards the middle of the single crystal in the parallel to the c-axis direction. This clearly indicate a correlation between Fe concentration and spacing between IDBs. In figure 5.14a the measured spacings are plotted against the distance into the single crystal, and in figure 5.14b focus is placed on the Fe concentration gradient from the line scan in figure 5.4c. By comparing figure 5.14a and 5.14b it is clear that spacing between the basal IDBs increase when the Fe concentration decrease, and when the Fe concentration gradient flattens, the changes in IDB spacing also flatten. The black dotted lines in figure 5.14 are drawn to indicate apparent start and stop of the gradient. It should be noted that the concentration gradient is acquired from DC 3 while the TEM weak-beam bright-field images are acquired from DC 2. However, the Fe concentrations in the single crystal are not expected to change much during cooling. In addition will additional Fe diffusion presumably result in an even better match with figure 5.14a as the Fe concentration then would be somewhat higher deeper inside the single crystal.

In figure 5.15a a diffraction pattern acquired from a region with a dense distribution of IDBs in sample DC 2 is shown. In this image, focus should be placed on the streaking of the diffraction spots. These features are real and assumed to arise from the repeating IDBs, this can be motivated by revisiting the diffraction pattern figure 5.10d. As this diffraction pattern is acquired from Area 2 where no IDBs were present, and no streaking of diffraction spots can be seen in this diffraction pattern. IDBs are large features compared to atomic planes, and large spacings in real space

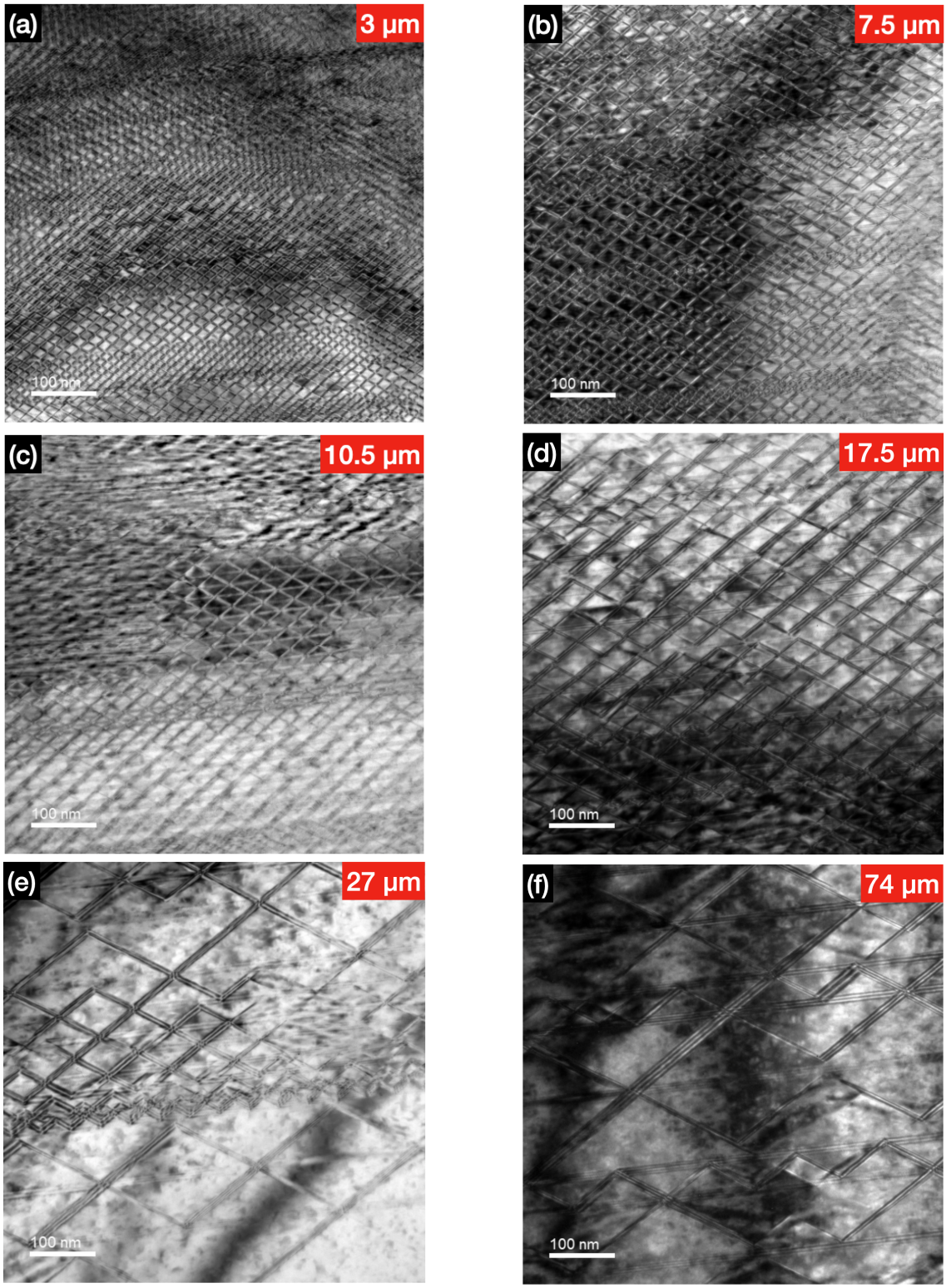

Figure 5.13: TEM weak-beam bright-field images of IDBs in increasing depth of the single crystal in DC 2. Depth is given in rigth corner of images. Please note that all images are taken with same magnification.

become small in reciprocal space. Therefore, if the spacing between domains was fixed we would expect to see many spots with a short and constant spacing in the diffraction pattern. However, since the IDB spacings are continuously changing as

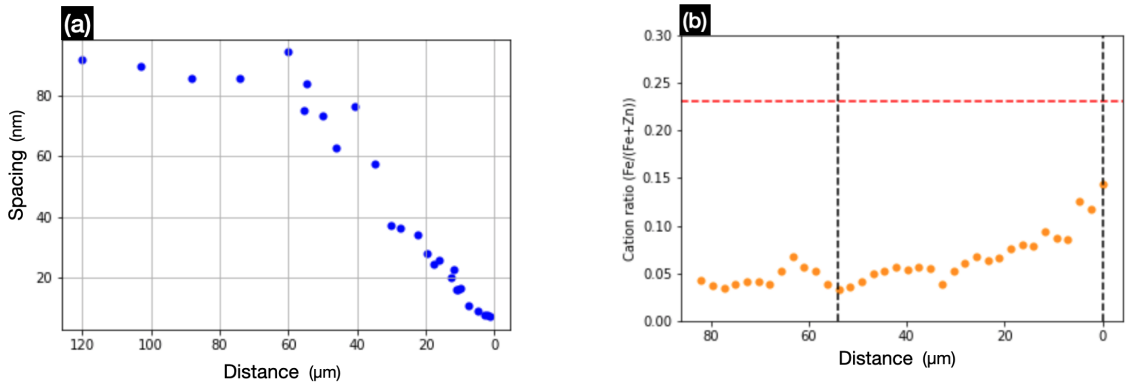

Figure 5.14: (a) Spacing between basal inversion domains as a function of depth into single crystal. (b) Fe concentration gradient of Fe in the corresponding direction.

we move deeper into the single crystal, streaking is as expected.

The direction of streaking is consistent with inversion domains being perpendicular to the c-axis of the single crystal. One can easily confirm this by considering the reciprocal lattice vector from the central spot to the 001 reflection as shown in figure 5.15a. The 001 reflection originates from the (0 0 1) plane in ZnO, which indeed is perpendicular to the c-axis. As the reciprocal lattice vector G_{001} and streaking of the spots is in the same direction, the features that give streaking must also be perpendicular to the c-axis.

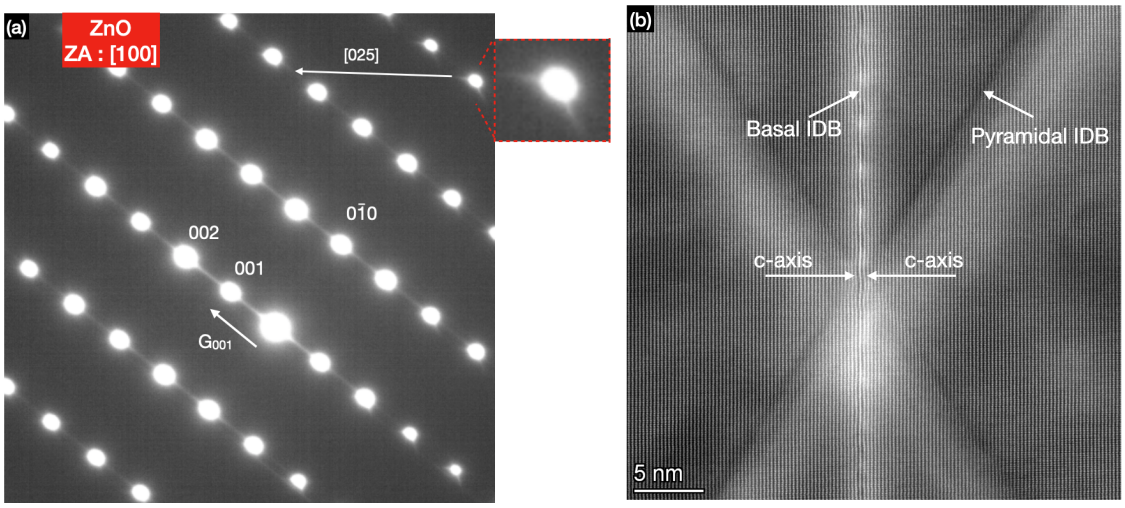

Figure 5.15: (a) Shows the streaking of diffraction pattern spots in an area having a dense distribution of IDBs in sample DC 2. The arrows indicate the directions of the streaking. (b) High resolution ADF STEM image of pyramidal and basal IDBs. The ZnO crystal is oriented along [010] zone axis.

By conscientiously searching over the diffraction pattern some streaking that could origin from the pyramidal IDBs was found. In litterature it is claimed that pyramidal IDBs are parallel to the $\{2\,\bar{1}\,5\}$ planes [28]. One of the equivalent planes to $(2\,\bar{1}\,5)$ is $(\bar{1}\,2\,5)$, and by adopting the same argumentation as for the basal IDBs this would correspond to streaking in the $[\bar{1}\,2\,5]$ direction. We should typically not be able to see such periodicity as we are in the [1 0 0] zone axis, however we migth catch a glimpse of the pyramidal IDB streaking in the top right corner of the diffraction

pattern before it escape in the [1 0 0] direction. As seen from the inset and the [0 2 5] arrow labeled in figure 5.15a the streaking direction in this projection appears to be consistent with the litterature claims. In figure 5.15b a high resolution annular dark-field (ADF) STEM image of the basal and pyramidal IDBs is shown. The direction of the c-axis is labeled, as well as the position of the basal IDB and the pyramidal IDB. One can notice the difference in contrast between the basal and pyramidal IDBs. As strain gives much contrast in this image, it is suggested that the basal IDBs introduces more strain and structural changes in the ZnO lattice than the pyramidal IDBs.

5.3.5 Transition area between Area 2 and the single crystal

We have seen that Area 2 contains ZnO with spinel precipitates and that the single crystal contains IDBs. Therefore it was of great interest to see if the transition from IDBs to spinel precipitates could be found. The transition from Area 2 to the single crystal was continuous on the short edges, as seen in figure 5.11a. It was therefore assumed that the transition from IDBs to spinel grains was most likely to be found in this region. Accordingly, all images in this section are aquired from the short edge transition between Area 2 and single crystal in sample DC 2. The approximate region being probed is shown with a green circle in figure 5.11a.

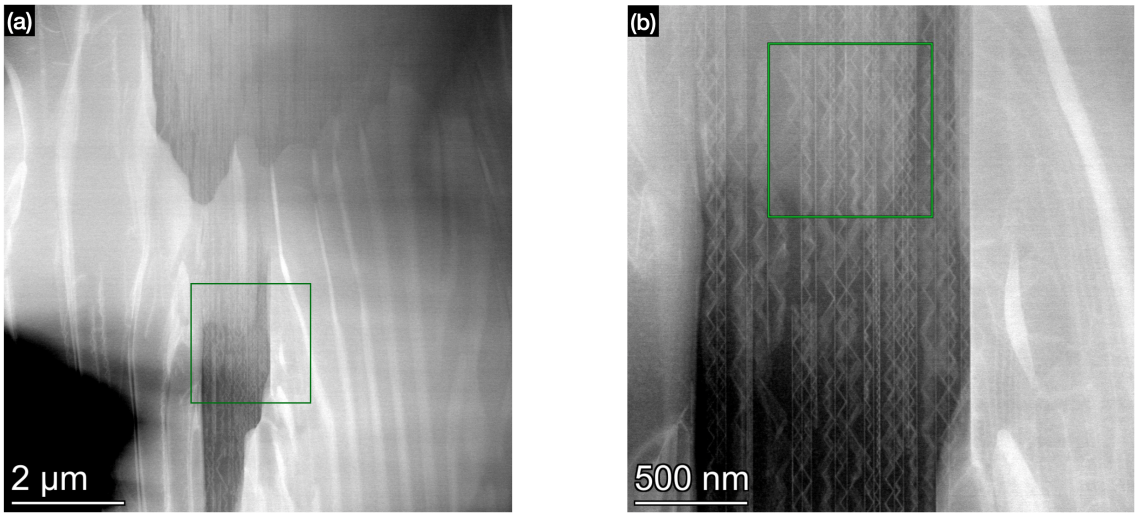

Figure 5.16: (a) ADF STEM image showing the interface between single crystal and Area 2. It can be noted that spinel grains are bright due to strain contrast. (b) ADF STEM image of the region outlined in 5.16a.

An overview ADF STEM image of the interface region and its close-up are shown in figure 5.16a and 5.16b, respectively. These ADF STEM images provide strong diffraction contrast, e.g. strained areas such as defects and coherent or semi-coherent precipitates are standing out as bright features. The strain could result from mismatch between the ZnO and spinel grain lattice. The spinel precipitates and IDBs stand out as bright features, while the ZnO grains and ZnO single crystal appear to be darker. This is confirmed by EDS mapping in STEM later.

In figure 5.16a, one could also notice the irregular shape of the boundary between Area 2 and the single crystal in this region. This made it difficult to identify the

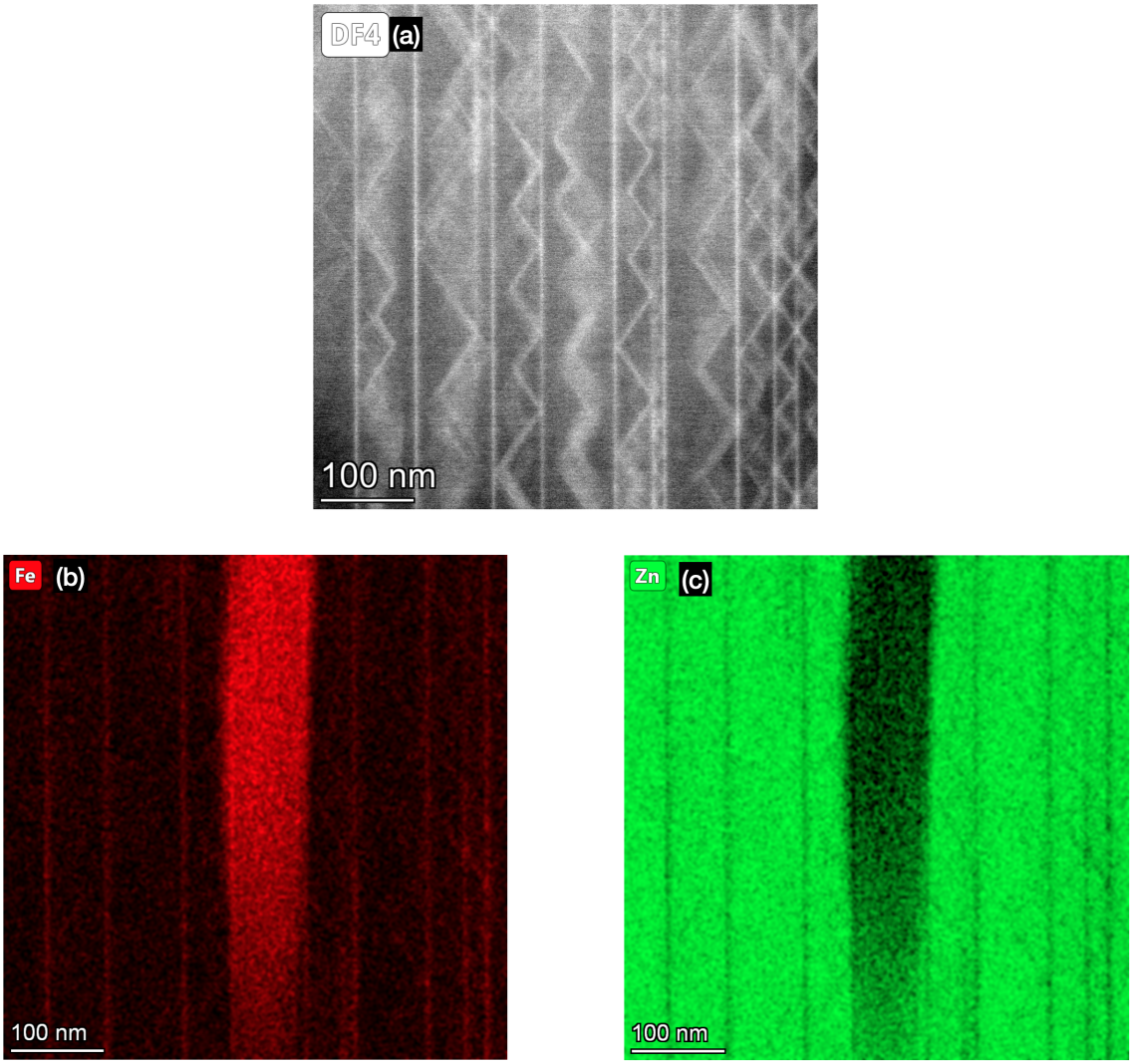

Figure 5.17: (a) ADF STEM image show the outlined region figure 5.16b. (b) Iron EDS elemental map clearly demonstrates the presence of iron in the spinel precipitate and IDBs. (c) Zn EDS elemental map clearly demonstrates the depletion of Zn in the spinel precipitate and IDBs compared to the surrounding matrix.

boundary, and determine which region is growing into which.

In figure 5.16b the outlined region in 5.16a is magnified and one can see an indication of a spinel particle being seemingly embedded in the ZnO single crystal with IDBs. However, one could also consider the possibility of spinel and IDBs being at slightly different depth of the sample, and thus misinterpreted to be embedded. EDS quantification of the precipitate showed low Fe concentration, compared to what is expected for the spinel. However, if the spinel precipitate is thin, x-rays generated from the ZnO matrix below could contribute to the spectrum, and thus skew the quantification. To understand if the spinel precipitate is embedded or overlaps with the ZnO single crystal the image focus condition was varied while probing a spinel particle with surrounding IDBs as shown in figure 5.16b. Features will be sharp at different focus if they are in different depth/height. However, both spinel particle and IDBs seemed to be sharp within the focus depth of 5 nm.

A close-up ADF STEM image of the region outlined in figure 5.16b is given in figure 5.17a. The IDBs show up clearly as bright features on the dark ZnO single crystal matrix. We can by considering the propagating direction of the IDBs conclude that the c-axis of the single crystal is perpendicular to the long axis of the spinel precipitate.

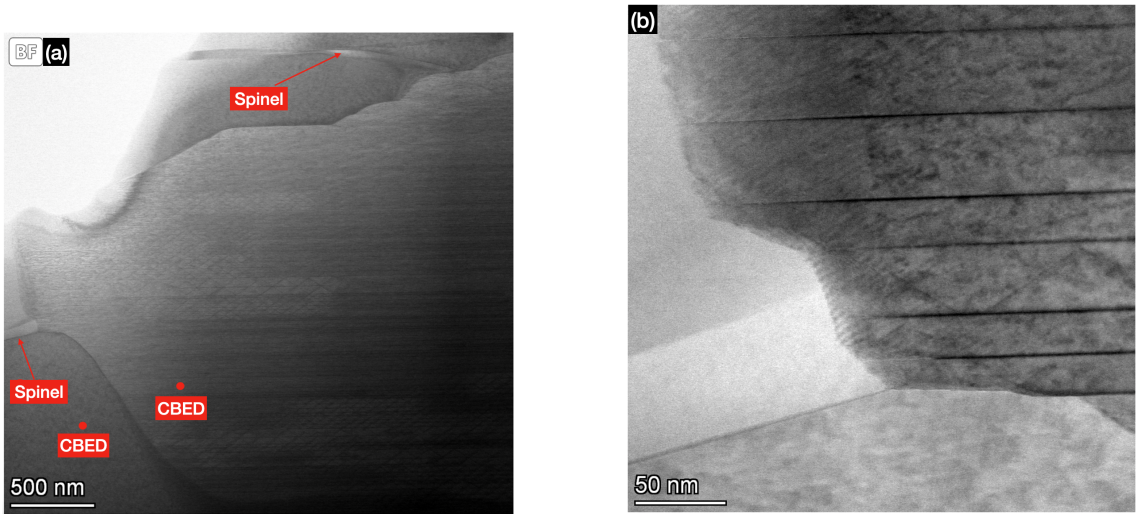

Figure 5.18: (a) STEM BF show "The pig", consisting of a single crystal piece with IDBs, surrounded by ZnO grains without IDBs and spinel grains. The orientation of surrounding ZnO grains is not the same as orientation of the ZnO single crystal. (b) Magnified STEM BF image of the transition between the single crystal and the left spinel precipitate in figure 5.18a.

The composition of the precipitate was also resolved in EDS maps as shown in figure 5.17b and 5.17c. We see that both the Fe-rich spinel precipitate and Fe-rich IDBs are resolved and located adjacent to each other. This was somewhat puzzling as we could expect the precipitate to aquire Fe from the surrounding regions in order to grow. However, even the IDBs located closest to the spinel precipitate are seemingly unaffected by the growth of the spinel. This doesn't prove that the spinel precipitate and IDBs can't be embedded, as the spinel could still be take iron from the surrounding ZnO grains, while leaving the IDBs intact.

Similar observations were made on other precipitates, and are shown in the appendix figure 9.2.

The STEM bright-field (BF) image shown in figure 5.18a was named "The pig". It shows a piece of the single crystal containing IDBs. Outside this "The pig" a matrix of ZnO with precipitated spinel grains can be seen and are marked by red arrows. No IDBs were found in the ZnO grains outside the single crystal. CBED patterns from the single crystal and the surrounding ZnO grains were checked as shown by markers in the image. By examining the CBED patterns it was found that the orientation of "The pig" was different from the orientation in the surrounding ZnO grains. A magnified STEM BF image of the transition between the left spinel grain and single crystal from figure 5.18a is shown in figure 5.18b. By careful investigation one can see Moiré fringes at the transition from spinel to single crystal, this is indicating an overlap between single crystal and the spinel particle. An important observation that can be made here is that the direction and spacing of the Moire'

fringes remains the same in the overlapping region of spinel and ZnO grain and the single crystal. First, this indicates that the ZnO grain and spinel grain has a very close orientation, and probably the same kind of orientation relationship that has been stated previously. Second, such Moire' fringes have never been observed in the ovelapping region of spinel and ZnO single crystal. This implies that the spinel grain shown in figure 5.16b and figure 5.17 is embedded in the ZnO single crystal and they are not overlapping. However more concrete evidence needs to be made.

5.3.6 DC 8

In previous work IDBs are suggested to be metastable configurations, and by adding a second annealing step, growth of spinel particles are promoted [9]. Therefore, a piece of the single crystal was extracted from sample DC 2 after the 1400 °C heat treatment, and subsequently annealed for another 48 hours in solitary condition at 1000 °C. As shown in figure 5.13, the single crystal in DC 2 was known to have IDBs, and based on the concentration gradients in figure 5.4b and 5.4c and that the single crystal is 0.5 mm thick. We estimated the initial average iron concentration in DC 8 to be approxamtly 5 at% Fe, however, this value must be considered higly uncertain as we lost control of which region of DC 2 that the piece DC 8 was extracted from. In this section, the (001) surface of DC 8 is probed, and all images shown in this section are acquired from this surface.

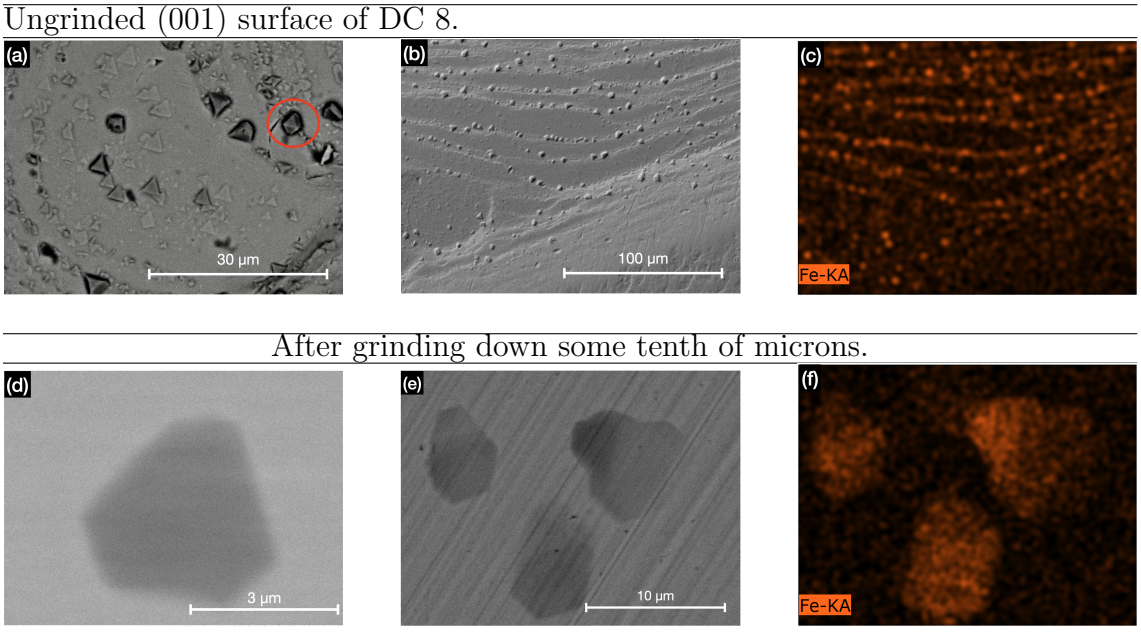

Figure 5.19: (a) SEM BSE image showing Fe-rich precipitates seemingly freely grown. An octahedral shaped precipitate is marked with a red circle. (b) SEM BSE image showing terraces with precipitates concentrated along the steps. (c) Fe resolved EDS map of the area with terraces. (d) SEM BSE image showing faceted Fe-rich grain. (e) SEM BSE image showing faceted grains with a contrast gradient. (f) Fe resolved EDS map show the correlation between contrast gradient and iron concentration.

First the ungrinded (001) surface of DC 8 was investigated in SEM, and was

clearly showing Fe-rich precipitates. Some of the precipitates were seen freely grow and extend above the surface level. The shape of the particles were mostly triangular, but some, as the one marked with a red circle in figure 5.19a, had an octahedral shape, which is the crystal form of spinels [45]. Near the edges of the sample terraces formed and the Fe-rich precipitates were concentrated along the steps of these terraces. In figure 5.19b an SEM BSE image of the terraces is acquired with the topographic settings on the microscope. One should be careful when interpreting what is up and down in images acquired with the topographic settings, however in this image it is fairly convincing that the Fe-rich precipitates are extending up and above the sample surface. The SEM EDS map in figure 5.19c clearly demonstrates the presence of iron-rich precipitates located along the steps in the terraces.

To check that presence of Fe-rich precipitates deeper into the single crystal, the (0 0 1) surface of DC 8 was grinded down some tenths of microns in the [0 0 1] direction. This lead to the observation of faceted precipitates as demonstrated by the grain in figure 5.19d. It can be noted that this shape resembles a submerged slice of a octahedron viewed down the four-fold symmetry axis. However, nearly all precipitates had a distinct contrast gradient and EDS mapping of the precipitates showed that the iron concentration correlates with the contrast gradient as seen in figure 5.19e and 5.19f. Since the vast majority of precipitates had a contrast gradient, the precipitates are proposed to be thin, at least in comparison to lateral dimensions.

Next, the sample was prepared for TEM investigation by grinding it down from both sides and subsequently ion mill. The grinding was again preformed in the [0 0 1], thus aiming to keeping the (001) surface. Before the TEM session DC 8 was investigated in the light microscope. Interestingly, the Fe-rich particles showed up clearly, as shown in figure 5.20a. By using the cross polarized filter, the optical anisotropic c-direction in ZnO was either transparent to light or totally blocking the light. In this way we were able to confirm that the precipitates were truly embedded in the ZnO single crystal. Characteristic red spots in the middle of each particles were observed in the optical microscope. Such spots were also seen in a few of the precipitates in the SEM. The fact that this was only seen in a few of the precipitates in SEM indicates that the spots are located in the middle depth of the precipitates since images acquired in SEM aren't transparent in the same way as optical microscope images. Therefore a perfectly grinded down particle is needed for the spot to become visible in SEM. An SEM BSE image showing spots in the middle of the precipitates is provided in figure 5.20b.

Another observation is that the precipitates are found in excess close to or at the surfaces of the single crystal piece. However, we are forced to rule out the initial concentration gradients from figure 5.4a and 5.4b as controll was lost on exactly which region of DC 2 the DC 8 piece was extracted from. However, in previous work it is claimed that Fe ions diffuse towards the surfaces of the ZnO single crystal at elevated temperatures, and that the spinel formation correlates with the iron concentration [38]. This is also seen from the phase diagram in figure 5.1. By adding the claimed Zn-vacancy clusters [30] to these observations it is tempting to suggest that the vacancy clusters could be traps for the Fe ions and nucleation sites for the precipitates seen in DC 8. This model would offer a neat explanation for the spots seen in the middle of the precipitates. However, more concrete evidence must be made.

In the search for evidence striking features were seen on the (001) single crystal surface of DC 8 when probing it with STEM. No good explanation could be found for these observations, however, due to their fascinating mosaic shapes the interested reader could have a look at them in the appendix figure 9.3.

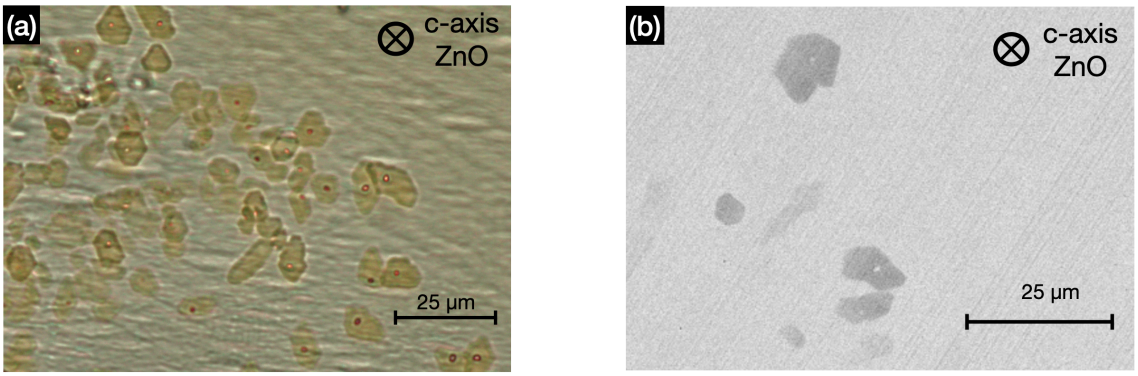

Figure 5.20: (a) Optical micrograph of DC 8 prepared for TEM investigation shows precipitates embedded in the single crystal and with a characteristic red spots in the middle. (b) SEM BSE image shows precipitates with spots in the middle.

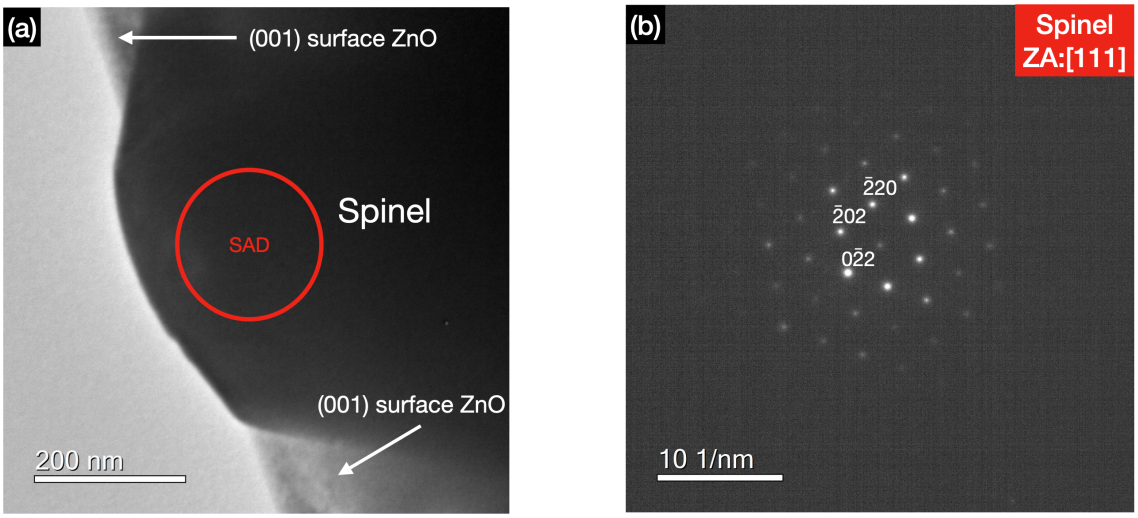

Figure 5.21: (a) TEM image showing one of the precipitates. The red circle shows where the selected area aperture was placed. (b) Diffraction pattern from the region outlined in figure 5.21a. The pattern matches a spinel structure in the [1 1 1] projection.

Figure 5.21a shows a TEM BF image of one of the precipitates, and figure 5.21b shows a diffraction pattern acquired by placing the SAD aperture as shown by the red circle in figure 5.21a. The diffraction pattern matches a spinel structure in the [1 1 1] projection. Since the surface of the single crystal is expected to be (001), these observations indicate the same orientation relationship as found between ZnO and spinel grains in Area 2, and it is assumed that the precipitates are ZFO spinels. However, SAD pattern at the same tilt should be acquired from the ZnO matrix to confirm this.

5.4 Conclusion

In this chapter the iron doped ZnO system is investigated by adopting the diffusion couple synthesis route. It was found that samples having a cation ratio of 66.7 at% iron and 33.3 at% zinc in the surrounding powders produced more compact samples than having 20 at% iron and 80 at% zinc in the surrounding powders. The cation ratio of 66.7 at% iron and 33.3 at% zinc in precursor powders gave a ZFO single phase in the area surrounding the single crystal after annealing. This region was referred to as Area 1 in the results and discussion part.

In the region between the single crystal and the surrounding ZFO phase, a crystallization zone formed during annealing. This region was referred to as Area 2 in the results and discussion sections. At 1400 °C this region consisted of ZnO with a high iron doping concentration. However when the samples were slowly cooled, ZFO grains precipitated in the ZnO matrix. The ZFO grains were found to have a preferred growing orientation relative to the ZnO grains.

As this reaction took place during cooling of the samples, the reaction is believed to be rapid.

These findings confirm that precipitation of spinels is possible in this system, and the crystallization zone could be a candidate for TCO material. However, the size of the embedded spinel particles were generally too large to have nano features. It is expected, though, that the size could be controllable by adjusting the variables in the annealing scheme.

Indications of more successful growth of the crystallization zone from the $\{1\,0\,0\}$ surfaces of ZnO single crystal was found. In this work, the inhibited growth in the $\langle 0\,0\,1\rangle$ directions is proposed to be related with Zn-vacancy cluster formation on the $\{0\,0\,1\}$ surfaces of the single crystal. These observations could be important in regard to further investigation of the crystallization zone.

EDS quantitative measurements showed a Fe concentration gradient in the single crystal. By resolving the single crystal microstructure in a TEM using the weak-beam bright-field technique, IDBs were clearly seen and the spacing between the basal inversion domains correlated with the Fe concentration gradient. The latter observations indicate that the diffusion couple synthesis route is a good choice for inducing iron inversion domain boundaries throughout bigger regions of a ZnO single crystal. This could be valuable information regarding device development based on IDBs.

The transition between the spinel grains and IDBs was probed, and IDBs and spinel grains were clearly seen in the same regions, seemingly embedded. However, due to an unsharp interface between the single crystal and the crystallization region, question was raised if the IDBs and spinel grains seen in the transition region could be overlapping. Hence, further investigations were made to resolve this. The investigations mostly pointed to features being embedded in the same ZnO matrix, however, no clear conclusion was drawn and the discussion is left open.

A second annealing step was preformed on a piece of the single crystal from a previously heat treated sample (DC 2). It was known that the single crystal contained IDBs prior to the second annealing step. Investigation of this sample showed triangular and octahedral spinel precipitates on the $(0\,0\,1)$ surface of the single crystal, and thin faceted spinel precipitates throughout regions near the surfaces of the sample. It is assumed that these precipitates formed during the second annealing

step, and thus show that a second annealing step can be added to promote the nucleation of spinel precipitates inside the single crystal. The necessity for a second annealing step to form the precipitates can be neatly explained by the lower iron concentration in the single crystal compared to the crystallization zone. However, the ambient conditions may also be different in the two regions which could influence the nucleation and growth rate.

The precipitates had a characteristic spot in the middle depth that was not observed before. This observation may be of scientific interest, as the spots appear to be small. A humble suggestion is made that small Zn-vacancy clusters could be nucleation sites for the spinel precipitates. The same apparent orientation relationship as in the crystallization zone between the ZnO matrix and the spinels precipitates was observed in this sample.

Chapter 6

The zinc oxide – antimony system

6.1 Previous work

Previous work done in this system is mainly focused on the grain size control of ZnO by Sb doping. Grain size seems to be controlled by Sb doping via the formation of spinel grains and IDBs. The ZnO grains that are infected by an IDB shows an exaggerated growth, but when infected grains collide, the growth is pinned [29]. While the formation of spinel grains have shown to inhibit the growth of ZnO grains [46]. Rečnik, Daneu and Bernik [30] proposed that the IDB nucleation mechanism in Sb_2O_3 doped ZnO is chemisorption of Sb at Zn-vacancy clusters on the (0 0 1) surface of ZnO. This nucleation mechanism is expected to give one IDB per ZnO grain, and is the preposed mechanism for dopants with a higher valency than +III, thus implying a change of oxidation state for Sb_2O_3 at elevated temperatures (1200 °C). Generally, studies probing the inversion domain formation have all been using annealing temperature of 1200 °C and small doping concentrations of Sb (< 0.1 at%) [30, 47, 48].

Annealing temperature of 1289 °C and Sb doping concentration of 0.68 at% have been claimed to give formation of a secondary phase with the formula $Zn_7Sb_2O_{12}$[46]. Miles and West [49] confirmed by Rietveld refinement that the structure is an inverse spinel ($[Sb_2/_3Zn_3/_4]O_4$), with tetrahedral sites occupied by Zn and octahedral sites containing a random mixture of Sb and Zn. The bandgap is $\approx$ 2.6 eV for pure $Zn_7Sb_2O_{12}$, but is claimed to be adjustable by addition of cobalt. As the amount of Co substitution increase the bandgap drops down to about 2 eV [50].

From the Motivation chapter of this thesis, we recall that $ZnSb_2O_4$ had a bandgap close to the proposed optimum of 2 eV (1.92 eV (DFT)). This spinel structure was claimed synthesized by Puebla, Monge and Rasines [51], by mixing ZnO powder with large excess of Sb_2O_3 powder, and annealed the mixture in a closed evacuated quarts ampoule. The temperature was kept at 750 °C for 24 hours, and then slowly decreased to 600 °C over a period of two days.

6.2 Experimental

The sample was made by mixing powders of ZnO with powders of Sb_2O_3, by that stoichiometrically facilitate the growth of the $ZnSb_2O_4$ spinel. The powders were mixed in a ratio so that the sample cointained 8 at% Sb (oxygen included). As no suitable phase diagram was found for this system, we chose a relatively high

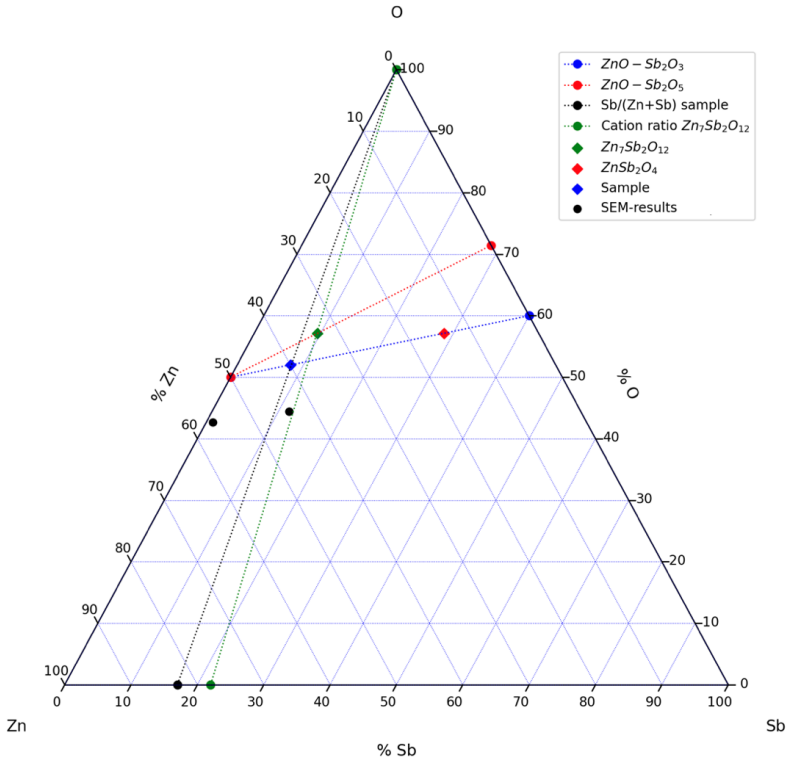

Figure 6.1: Gibbs trangle showing nominal sample composition (blue diamond), EDS results for ZnSb1 (black circles), precursors (red and blue circles) and relevant spinel phases (green and red diamonds). Dotted lines show cation ratios (black and green) and binary isothermal lines for relevant precursors(red and blue).

doping concentration compared to doping concentrations used in previous work. This was partly motivated by the intention of finding the maximum solubility of Sb in ZnO and partly to form a proper amount of the secondary phase. By that enable characterization of both phases, and get an impression of the phase stability in the system. The mixed powder was ball milled and pressed to a pellet as explained in the Method chapter. The annealing temperature was adjusted up from the temperatures used in previous work and set to 1400 °C. By that reaching for higher solubilities than what is reported for samples annealed at 1200 °C. The dwell time was set to 12 hours and cooling rate was 100 °C per hour. After a first investigation, the sample was re-heat treated at 900 °C for 12 hours in order to promote precipitation. Results from the sample heat treated at 1400 °C is referred to as ZnSb1, while the re-heat treated sample is referred to as ZnSb2.

6.3 Results and discussions

A convenient way to visualize sample compositions is by plotting it in a triangular plot (a Gibbs triangle), as shown in figure 6.1. The nominal composition of the sample made by mixing ZnO and Sb_2O_3 must lay on the blue dotted line. The antimony content of the synthesized sample is 8 at%, and is depict by the blue diamond in figure 6.1. The composition of the reactants are given by the red and blue circles and relevant spinel phases are shown as diamonds.

Figure 6.2 shows the X-ray diffractogram of both samples. The lattice constants

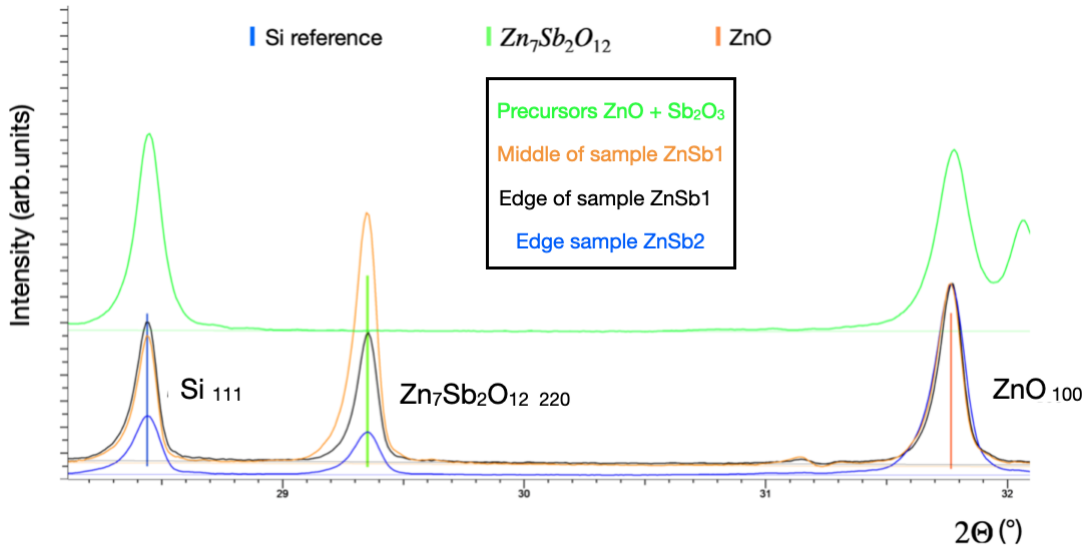

Figure 6.2: XRD diffractogram ZnSb1 and ZnSb2 show precence of $Zn_7Sb_2O_{12}$ and ZnO, and indications of Sb evaporation from surface near regions. The silicon 111 peak was used for calibration. The color coding in the inset matches the diffractograms.

of ZnO are not significantly different from that reported for pure ZnO. Since lattice constants tend to change when impurity atoms with different radii are incorporated into the structure, this observation could indicate low solubility of Sb in ZnO. The Sb-rich phase cannot be indexed with the tetragonal lattice of $ZnSb_2O_4$, but fits excellently to the cubic lattice of the inverse spinel $Zn_7Sb_2O_{12}$.

The results from EDS-analyzes of ZnSb1 are shown with black circles in figure 6.1, two black circles are shown as two phases were present in the sample. We see that the oxygen concentration measured by EDS is clearly underestimated. This was however not surprising, and are commonly explained by the low atomic number of oxygen, giving an increased absorption of generated x-rays, as discussed in the Method chapter. No attempt was done to improve the accuracy of oxygen measurements, but instead, focus was placed on the atomic ratio of the cations, Sb/(Zn + Sb). This ratio can easily be read out from a Gibbs triangle. Two examples are given in figure 6.1. By extrapolating the line between the oxygen corner and the nominal sample composition down to the line joining Zn and Sb (black dotted line), this ratio can be read directly. The same can be done for the spinel composition $Zn_7Sb_2O_{12}$ (green diamond). We see that the green dotted extrapolated line in figure 6.1 almost intersect with the EDS measurements for the Sb-rich phase, indicating good accuracy for the cation ratio in SEM EDS. The correct sample composition after annealing is expected to be at the intersect between black and red dotted line, implying that Sb_2O_3 has changed oxidation state from III to V.

Figure 6.3a shows the microstructure on the surface of sample ZnSb1, and we can clearly see that two phases are present. As this is an SEM BSE image, the difference in contrast is related to composition of the phases. Since we know from XRD that the phases present in the sample are ZnO and $Zn_7Sb_2O_{12}$, we understand that ZnO is the phase with dark contrast and $Zn_7Sb_2O_{12}$ has bright contrast as it has higher average atomic number pr. volume than ZnO. From the Materials and

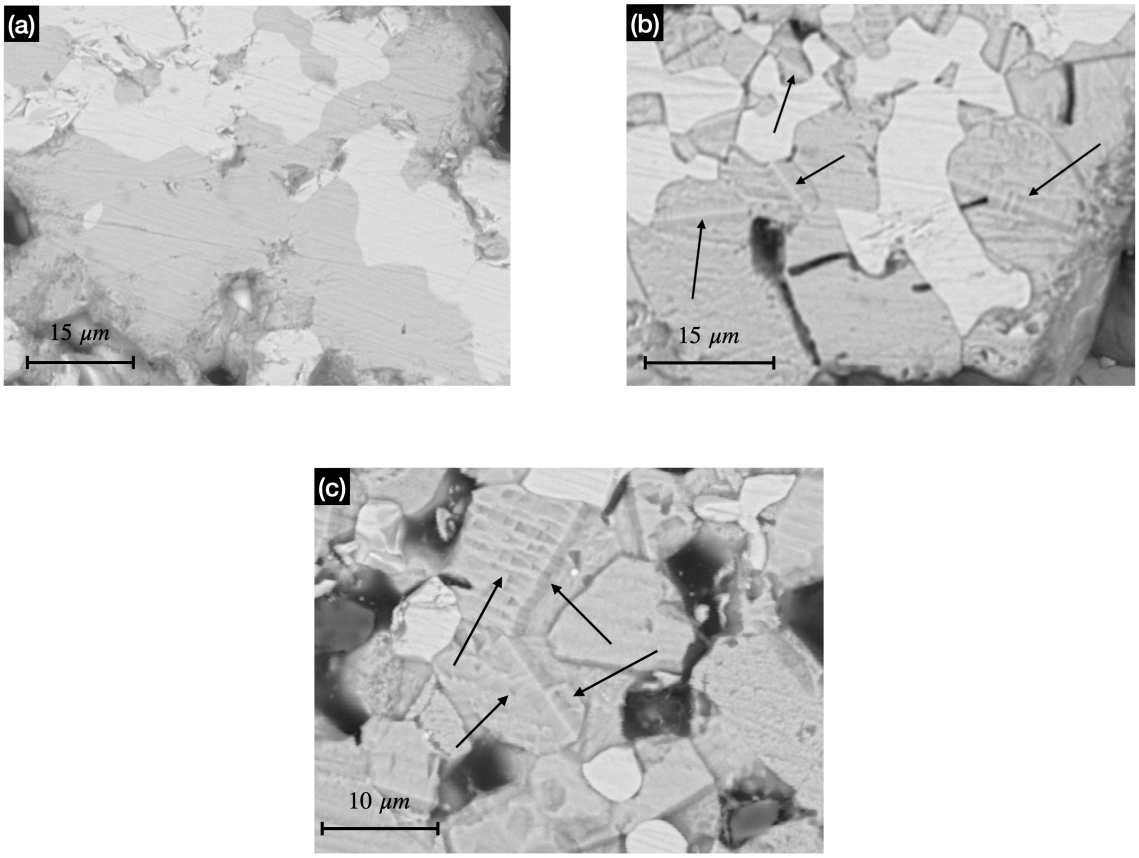

Figure 6.3: SEM BSE images of sample ZnSb1 (a) Show unetched surface with two phases present. ZnO has dark contrast, due to lower average atomic number than $Zn_7Sb_2O_{12}$. (b) Show the etched surface with linear features. (c) Show the etched surface with etch-pits in ZnO oriented head-to-head at the linear features. The etch pits are presumed to indicate the direction of the c-axis in ZnO.

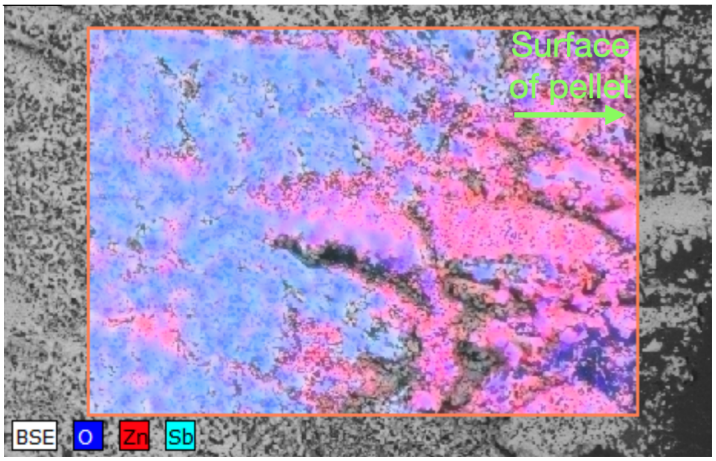

Figure 6.4: SEM EDS mapping of a region close to the surface of ZnSb1. Green arrow points in the direction of the surface of pellet.

structures chapter we saw that Sb_2O_3 doped ZnO develops one IDB per ZnO grain upon annealing. The thickness of an IDB is so small that one would expect that a TEM would be needed to observe them. It has, however, been claimed that they can be rendered visible in an SEM with the aid of etching [30]. To test this, ZnSb1 was grinded and etched with 1/20 diluted HCl for 20 seconds. The acid attacks inhomogeneities at the surface, such as IDBs and grain boundaries, and thereby render them visible. This did indeed give rise to linear features when the sample subsequently was observed in the SEM. These are marked with black arrows in figure 6.3b, and as predicted by literature, no more than one of these were observed in each grain. The features were not confirmed to be IDBs as they were not found in TEM investigations of the sample. However, the triangular etch-pits marked with black arrows in figure 6.3c were also seen in the article suggesting that this works [30]. The pits are assumed to indicate the direction of the c-axis, and if so clearly demonstrate the head-to-head orientation of the ZnO domains on each side of the IDB.

Porosity is to be expected in sintered samples due to the difficulties of removing all voids originally present in the starting powders sample. For this samples it was, however, observed a marked increase in porosity towards the surface of the sample. The increase in porosity correlates with a decrease in the Sb concentration as shown in the SEM EDS mapping of an area close to the surface of the ZnSb1 pellet in figure 6.4, and the same can be shown by XRD. In figure 6.2 the black diffractogram is acquired with powder taken from a region near the surface of ZnSb1 and the orange diffractogram is acquired by taken powder from the middle regions of the same sample. To facilitate comparison, the diffractograms have been normalized for the 100 peak from ZnO. It is clearly seen that the peak from the $Zn_7Sb_2O_{12}$ phase is smaller in the diffractogram obtained from the part closer to the surface. This effect is even more pronounced when powder from sample ZnSb2 is analyzed as seen from the blue curve in figure 6.2. Thus it seems evident that Sb is evaporated from regions near the surface of samples.

The TEM was used in the search for IDBs and spinel precipitates in the ZnO grains in both ZnSb1 and ZnSb2. This was done by locating ZnO grains by EDS, and carefully scan for irregularities in the matrix of the ZnO grains. However, only

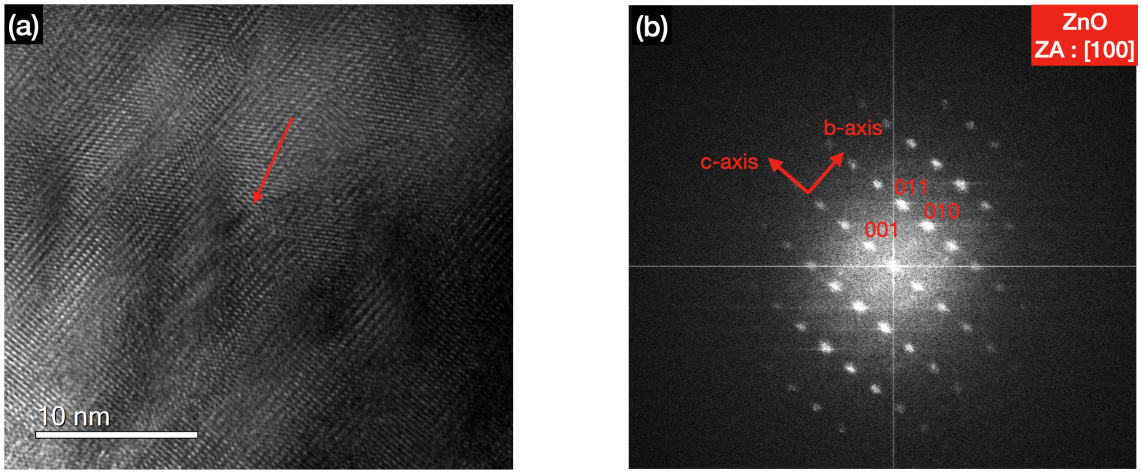

Figure 6.5: (a) High resolution TEM image showing a dislocation in the ZnO matrix. (b) FTT from (a) giving a projection perpendicular to c-axis.

intrinsic defects in the ZnO lattice were found, such as the dislocation shown in the high resolution TEM image in figure 6.5a. Such defects are ordinary also in pure ZnO [52], and therefore assumed to not be related to Sb doping. In figure 6.5b the corresponding Fast Fourier Transform (FFT) shows that this is a projection perpendicular to the ZnO c-axis. All the spinel grains investigated in TEM in ZnSb1 and ZnSb2 were assumed to be a result of regular phase transitions, this gives secondary phases, and not precipitations in the ZnO matrix. Therefore these spinel grain were not given much attention. It could be an indication of precipitates if the Sb concentration is lower in ZnO for ZnSb2 compared to ZnSb1, as this could imply that some Sb atoms have left the ZnO matrix in ZnSb1. However, TEM EDS quantifications showed that the Sb concentration in ZnO was $< 1\%$ for both ZnSb1 and ZnSb2.

6.4 Conclusion

Since the Sb solubility in ZnO was low and seemingly not changing with temperature, and the fact that no sign of precipitates was detected, a conclusion was drawn that the ZnO-Sb system didn't show promising properties in regard to the goal of this thesis. Also, the fact that the spinel formed was not the $ZnSb_2O_4$ as aimed for, sustained this conclusion. Of course, if precipitations were to happen, the surroundings for the precipitates could be different than surroundings for the secondary phase. Thus, it's not obvious that the structure of a precipitated phase is the same as the secondary phase. Nevertheless, the results were although quite consents with literature, except for that no IDBs were seen in the TEM investigations. However, this could be explained by the few ZnO grains available for investigation in the samples, and by considering the fact that only one IDB is expected to be precent in each ZnO grain. As the $Zn_7Sb_2O_{12}$ phase is consuming Zn efficiently, another experimental set up with a lower Sb doping concentration would facilitate investigation of IDBs. However, as this work probes the solid state precipitate reaction, no such IDB specific sample was made.

Chapter 7

The zinc oxide – vanadium system

7.1 Previous work

An Ellingham diagram based on vanadium oxides was provided by Bergerud [13] and is shown in figure 7.1a. To find the most stable configuration, a line is drawn from the "O" point to the oxygen partial pressure in ambient sample conditions, listed on the right y-axis. The region the line passes through at a given temperature is the most stable state at the given temperature and oxygen partial pressure. From the Ellingham diagram we see that V_2O_5 is predicted to be thermodynamically stable in air throughout the temperature range shown. That is vanadium having an oxidation state of V. Therefore, a binary phase diagram with ZnO and V_2O_5 as components, provided by Kurzawa et al. [53], is used for the discussion regarding choice of annealing temperatures. The phase diagram is shown in figure 7.1b.

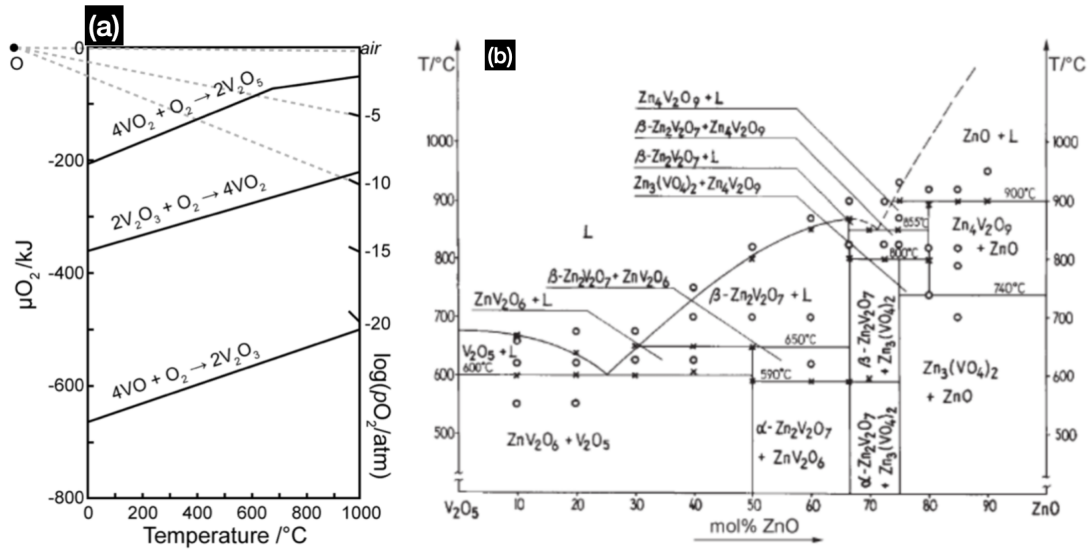

Figure 7.1: (a) An Ellingham diagram showing thermodynmical stable vanadium oxides as a function of temperature and oxygen partial pressure [13]. (b) Binary phase diagram with components ZnO and V_2O_5 [53].

7.2 Experimental

Different vandium oxides were tried as precursor powders together with the ZnO powders. All samples prepared in this system are listed in table 7.1 and all compositions are given as cation ratios.

As seen from the phase diagram in figure 7.1b, samples containing ZnO will be partly melted at temperatures above 900 °C. A partly melted sample may still be useful, but we chose 875 °C as the annealing temperature for the first samples. For the compositions in Sample 1 and Sample 2, the phase diagram predicts $Zn_4V_2O_9$ and ZnO as the expected phases. If the reaction rates are fast enough, the samples could contain $Zn_3(VO_4)_2$ and ZnO after cooling to room temperature. The phase diagram shows that V_2O_5 melts above 675 °C and together with ZnV_2O_6, goes through a eutectic reaction at 600 °C. For samples made of ZnO and V_2O_5, one can easily think that this will lead to partial melting of the sample. Therefore, Sample 3, Sample 4, Sample 5 and Sample 6 were prepared by a two-stage heating-scheme, with an isothermal annealing at 650 °C for 24 hours prior to the high temperature annealing.The first two samples were prepared with high vanadium content, making sure that the ZnO phase would have maximum vanadium doping concentration. Based on observations in Sample 1 and Sample 2, the doping concentration was adjusted down in subsequently prepared samples. This was essentially done to form more of the vanadium doped ZnO phase.

After a first heat treatment, both Sample 1 and Sample 2 were split in two. One of the halfs were investigated as they were and the other halfs were re-heat treated at 450 °C. The re-heat treated samples are reffered to as Sample 7 and Sample 8, and thus have an annealing history in terms of Sample 1 and Sample 2, respectively.

Table 7.1: Show the samples prepared in this system.

Sample	**Vandium content (%)**	**Vandium oxide(cation ratio (%))**	**Annealing temperature (°C)**	**Annealing time (hours)**	**Crucible**
1	16	V_2O_3	875	24	Alumina
2	16	V_2O_4	875	24	Alumina
3	6	V_2O_4	950	48	Alumina
4	6	V_2O_4	950	48	Quartz ampule
5	6	V_2O_4	950	48	Platinum
6	6	Metallic V	950	48	Closed evacuated quartz ampule
7	16	V_2O_3	450	48	Alumina
8	16	V_2O_4	450	48	Alumina

7.3 Results and discussions

SEM EDS measurements in Sample 1 and 2 gave initially promising results as the vanadium concentration in ZnO grains seemingly was as high as 4.5 at%. This solubility could possibly be so high that a subsequent annealing at lower temperature would give precipitates inside the ZnO grains.

Sample 1 and Sample 2 were prepared for TEM investigation by drop casting powders on holey carbon films. The main purpose for the investigation was to obtain EDS quantification in the TEM, and search for structural irregularities inside ZnO grains which could be related to vanadium doping such as IDBs or even precipitates if reactions goes during cooling. The EDS quantification gave varying results and no clear conclusion on the vanadium concentration in the ZnO grains could be drawn. However, it was found that Sample 1 and Sample 2 contained many small crystallites. The crystallites could complicate the EDS results, as many grains are contributing to the signal. In figure 7.2a a TEM bright-field image shows typical microstructure in Sample 2, while figure 7.2b shows the selected area diffraction pattern acquired from the outlined region in 7.2a. We see from the scale bar in figure 7.2a that this is a small grain, and the tendency to form rings in the diffraction pattern indicate polycrystallinity and thus that the grain consist of even smaller crystallites. However, as this was not the main goal of this thesis, the crystallites were not investigated any further.

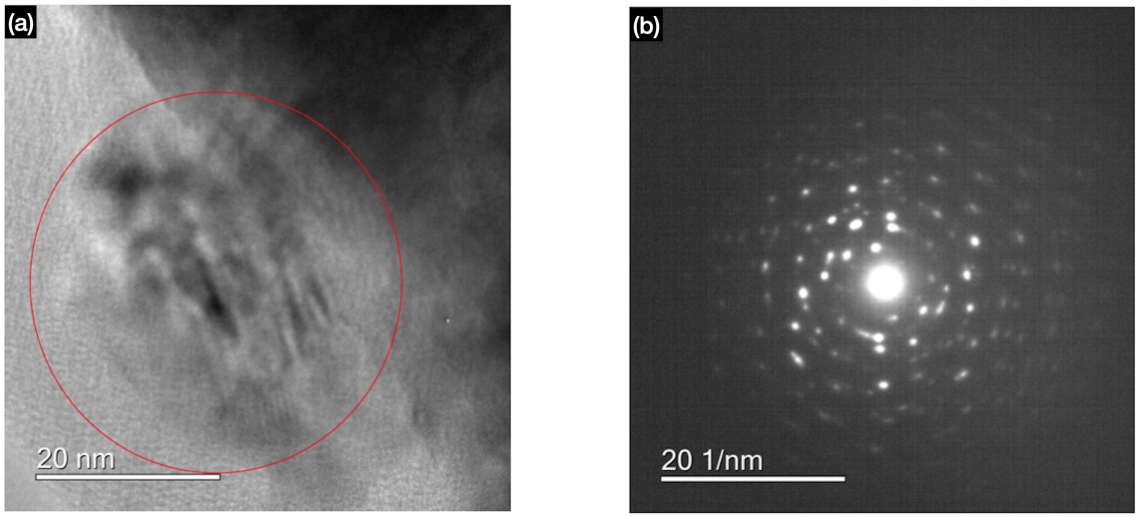

Figure 7.2: (a) TEM bright-field image showing small grain in Sample 2. (b) Selected area diffraction pattern from the outlined red circle. The tendency to form rings indicate polycrystallinity.

As it was challenging to obtain reliable EDS quantifications from Sample 1 and Sample 2, a grinded TEM sample was prepared from Sample 2. Grinded samples offer greater control of the probed regions and contributions from secondary phases are easier to avoid and thus ease the interpretation. When the grinded sample was investigated a distinct grain boundary between a vanadium-rich phase containing 33 at% vanadium and the ZnO phase was found. The vanadium-rich phase was later confirmed to be the monoclinic $Zn_4V_2O_9$ phase.In figure 7.3 a TEM bright-field image of the grain boundary between the ZnO grain and $Zn_4V_2O_9$ grain is shown. By

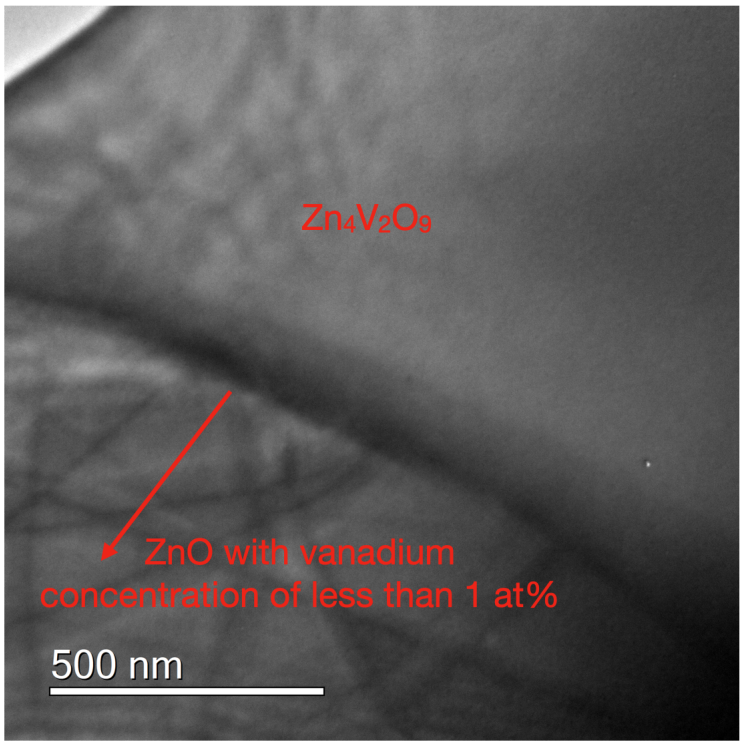

Figure 7.3: TEM bright-field image showing the grain boundary between the ZnO grain and the $Zn_4V_2O_9$ grain. The red arrow illustrate how EDS quantifications were acquired.

using the grain boundary as the starting point for the quantitative EDS measurements, and then successively measure vanadium concentration deeper into the ZnO grain as depiced by the red arrow in figure 7.3, we could acquire more reliable EDS quantifications, and also uncover any concentration gradient. The latter procedure gave consistently vanadium concentration of less than 1 at%, thus indicating that the true solubility of V is ZnO is rather small. The low vanadium solubility in ZnO in Sample 1 and Sample 2 is proposed to explain why no precipitates were found when Sample 7 and Sample 8 were investigated in the TEM.

Unit cell refinement was preformed as change of unit cell size can give an indication of solubility. The refinement was preformed with the program Unit Cell, this program calculates a least square approximation of the measured d-values obtained by the well known relation for d-spacings in hexagonal structures.

$$\frac{1}{d^2} = \frac{4}{3}\left(\frac{h^2 + hk + k^2}{a^2}\right) + \frac{l^2}{c^2} \tag{7.1}$$

where h,k,l are the Miller indices, a and c are unit cell parameters and d is planar spacing.

The analyzed sample was again Sample 2 and the results from the refinement are shown in table 7.2. The unit cell refinement gave a small but significant decrease in volume after the first high temperature heat treatment (875 °C), and a small but significant increase after the second heat treatment (450°C). Volume after the last heat treatment is not significantly different from the volume of pure ZnO. These results could indicate some change in the vanadium concentration in ZnO during the annealing procedure, but the observed difference in unit cell volume is low compared

to a claim in literature [54]. However, in this study the solubilty limit of vanadium in ZnO was also claimed to be higher.

Table 7.2: Results of unit cell refinement of ZnO with the uncertainties given in the parentheses.

Parameter	**Pure ZnO**	**1. heat treatment**	**2. heat treatment**	**Δ pure vs 1.HT**	**Δ 1HT vs 2.HT**
a-axis (Å)	3.24982(8)	3.24952(8)	3.2500(2)	0.00030(16)	-0.00040(28)
c-axis (Å)	5.2063(2)	5.2063(2)	5.2065(4)	0.0000(4)	-0.0002(6)
Volume ($Å^3$)	47.619(3)	47.610(3)	47.626(6)	0.009(6)	-0.016(9)

In Sample 3 to 6 the annealing temperature was raised to 950 °C as this temperature had been reported to give the highest solubility of vanadium in ZnO [54]. However, Sample 3 and Sample 4 were clearly segregated, and it was seen that the segregated phase reacted with the alumina crucible and the quarts ampule used as sample containers. This is shown in the optical micrograps in figure 7.4a and 7.4b. These observations are however consistent with the phase diagram shown in figure 7.1b, as a partial melting is expected. EDS measurements on Sample 3 and Sample 4 gave a lower vanadium concentration in the ZnO grains than what was measured in Sample 1 and Sample 2. As the segregated phase was rich in vanadium it was attempted to avoid the reaction with sample containers, and a synthesis route using platinum foils as crucibles was tested. Platinum is a inert element and it was assumed not to reaction with the segregated phase, and thus preserve more vanadium inside the sample. Figure 7.4c show an optical micrograp of Sample 5 which was prepared using the latter synthesis route. It was observed that the synthesis maneuver did indeed result in no reaction between the segregated phase and the platinum crucible. However, EDS measurements gave no increased vanadium solubility in ZnO for the sample prepared using platinum foils.

Figure 7.5a shows the results of powder XRD from Sample 1. It was clearly seen that Sample 1 consisted of ZnO and $Zn_4V_2O_9$, as predicted by the phase diagram. One could notice that the $Zn_4V_2O_9$ phase has many peaks, which corresponds to a structure with low symmetry. This is consistent with $Zn_4V_2O_9$ having a monoclinic unit cell, as proposed in literature [55]. The silicon peak was used for calibration of the diffractogram.

No apparent difference between Sample 1 and Sample 2 regarding phases formed nor solubility was found. That is, the initial oxidation state of vanadium is not affecting thermodynamical stability at 875 °C. In retrospect this felt obvious as the Ellingham diagram showed that oxidation to V_2O_5 will take place when samples are annealed in air. One could probably discuss the possibility of slow oxidation reactions opening up for different reaction paths, however in open air conditions oxidation reactions are often fast. However, one alternative approach to this is to anneal the sample in vacuum, by that reducing the oxygen available for the sample. This syntheses route was tested by annealing a sample with metallic vanadium as precursor in an evacuated closed quartz ampule. The metallic vanadium can be

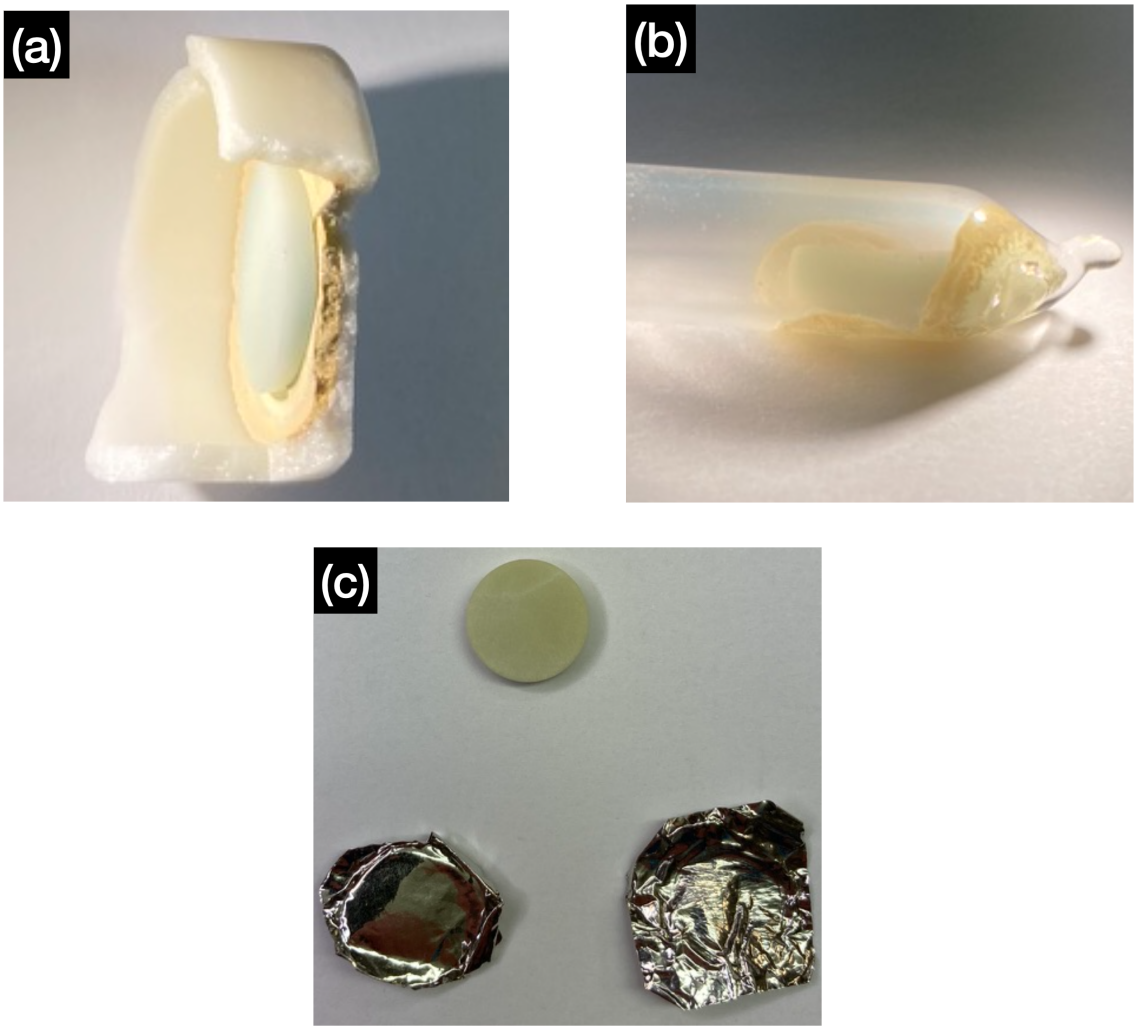

Figure 7.4: (a) Sample 3, annealed in alumina crucible. (b) Sample 4, annealed in quartz ampule.(c) Sample 5, annealed in platinum foils.

considered having zero valency, thus more oxygen is need in order to oxidize the precursor to V_2O_5, and as a limited amount of oxygen is available in the evacuated ampule one could expect that other phases become stable. The pellet was wrapped in platinum foils to inhibit reaction with the quartz ampule, and is referred to as Sample 6. This synthesis route did indeed lead to the formation of the spinel phase ZnV_2O_4, as confirmed by the XRD diffractogram shown in figure 7.5b. In the diffractogram one can notice that this structure give rise to fewer peaks compared to the $Zn_4V_2O_9$ structure, which is consistent with ZnV_2O_4 being a cubic structure with high symmetry. This sample was investigated in TEM, however solubility was still found to be low. One last attempt to promote precipitation was done by re-heat treat Sample 6 at 600 °C, however, no precipitates nor inversion domains were found after a second heat treatment.

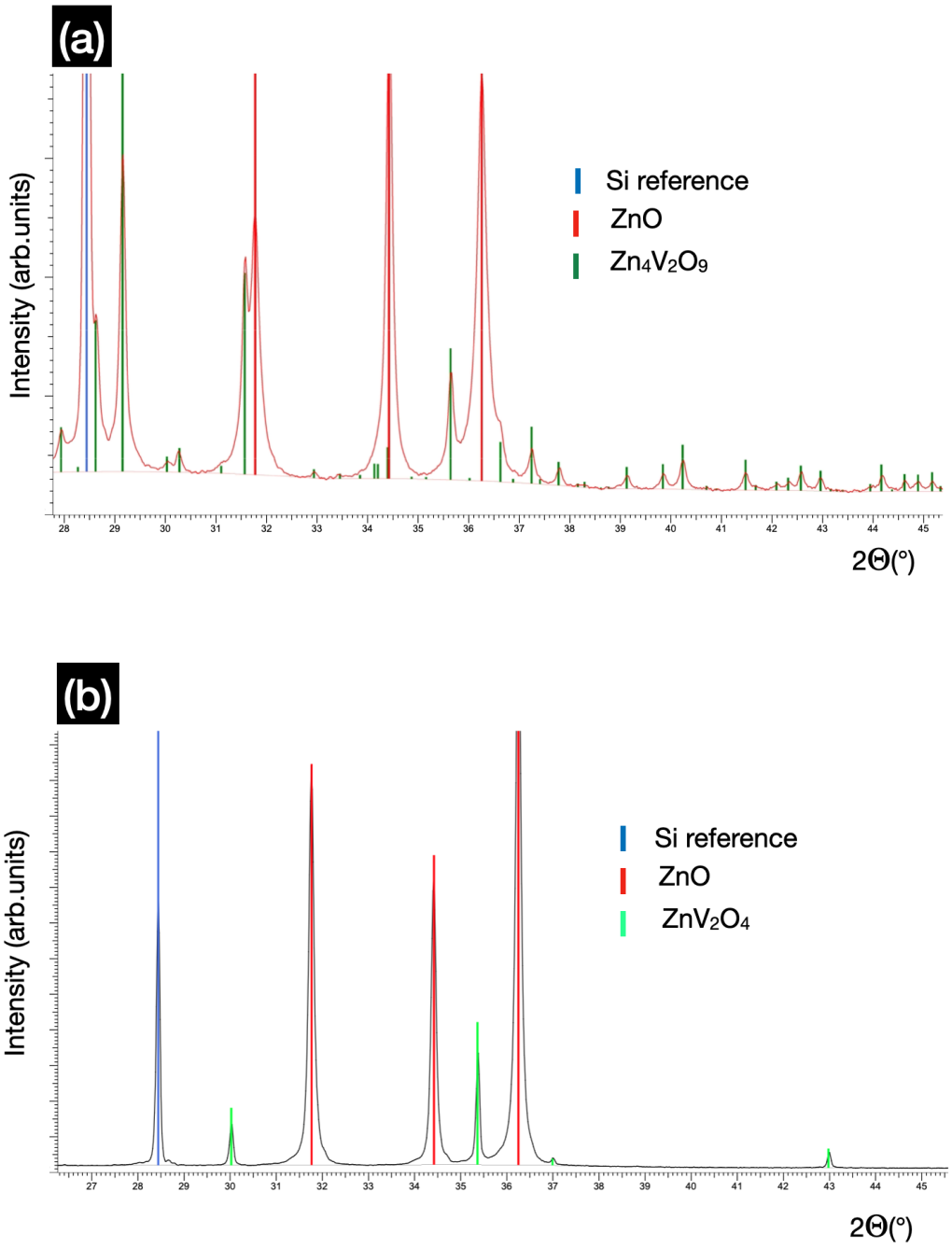

Figure 7.5: (a) XRD diffractogram from Sample 1 showing presence of monoclinic phase $Zn_4V_2O_9$. (b) XRD diffractogram from Sample 6 showing presence of cubic spinel phase ZnV_2O_4.

7.4 Conclusion

In this chapter we have investigated the properties of the ZnO - vanadium system, with vanadium concentrations of 16 at% and 6 at%. The samples were annealed at 875 °C and 950 °C, and some samples were selected for re-heat treatment at 450 °C and 600 °C. All samples that were annealed in air resulted in the formation of $Zn_4V_2O_9$ and ZnO, as predicted by the phase diagram in figure 7.1b.

Based on TEM EDS quantitative measurements and unit cell refinement the solubility of vanadium in ZnO was found to be low. Indications of slight changes in solubility with temperature was seen, but no sign of precipitates were found in TEM investigations of the samples heat treated twice.

However, it was found that the addition of vanadium gave small crystallites which could be relevant for other work. It was also found that preparation of samples in platinum foils enables annealing above the solidus temperature without a reaction with the pellet and the sample container. In addition, a synthesis route giving the cubic spinel phase ZnV_2O_4 was found. However, none of the synthesis adjustment resulted in increased solubility of vanadium in ZnO.

Chapter 8

Suggestions for further work

8.1 Iron system

This system displayed the most promising features in regard of the solid state precipitation of spinels. Future work could be on controlling the growth of the crystallization region (Area 2). A suggestion would be to use a single crystal where the a-axis of the single crystal is perpendicular to the large surface of the single crystal plate, as the crystallization is more efficient in this direction.

Future work could also be focused on investigation of the spinel precipitates formed in the second annealing step. A measure of the thickness can be done by probing the precipitates in the perpendicular to the c-axis direction. In addition, more work needs to be done in order strengthen the proposed nucleation mechanisme hypothesis. This could moreover give information about what the spots seen in the middle of the precipitates really are.

A suggestion to obtain size control of precipitates is to adjust the variables in the annealing schemes. This should be possible for the precipitates formed during cooling in the crystallization zone, and those formed in the second annealing step in the single crystal.

In addition, it would have been interesting to see electrical conductivity measurements on the ZnO single crystals with inversion domain boundaries.

However, it is known that Fe contamination in silicon solar cell can cause severe degeneration of electric properties [56]. Thus, ways to avoid problems related to this must be considered in order to make functioning devices to be implemented in silicon solar cell systems.

8.2 Antimony system

Time was to short to follow up on the synthesis route claimed to yield the $ZnSb_2O_4$ spinel phase [51], as this reference was found rather late in the process. It would however been interesting to check if this result was reproducible, and also check if the solubility of Sb in ZnO is different when a sample is prepared in an evacuated closed ampoule. This is, at least theoretically possible since the thermodynamically terms are changed. Possibly could the low oxygen atmosphere inhibit oxidation of Sb_2O_3 to Sb_2O_5, and therby preserve the +III valency. This could, based on the paper by Rečnik, Daneu and Bernik [30] instead yield an internal diffusion mechanism of

IDBs, which is characteristic for dopants with higher solubility such as Fe, Ga and In.

8.3 Vanadium system

No suggestions for further work are proposed in this system in regard of precipitating spinels in the ZnO matrix.

Chapter 9

Appendix

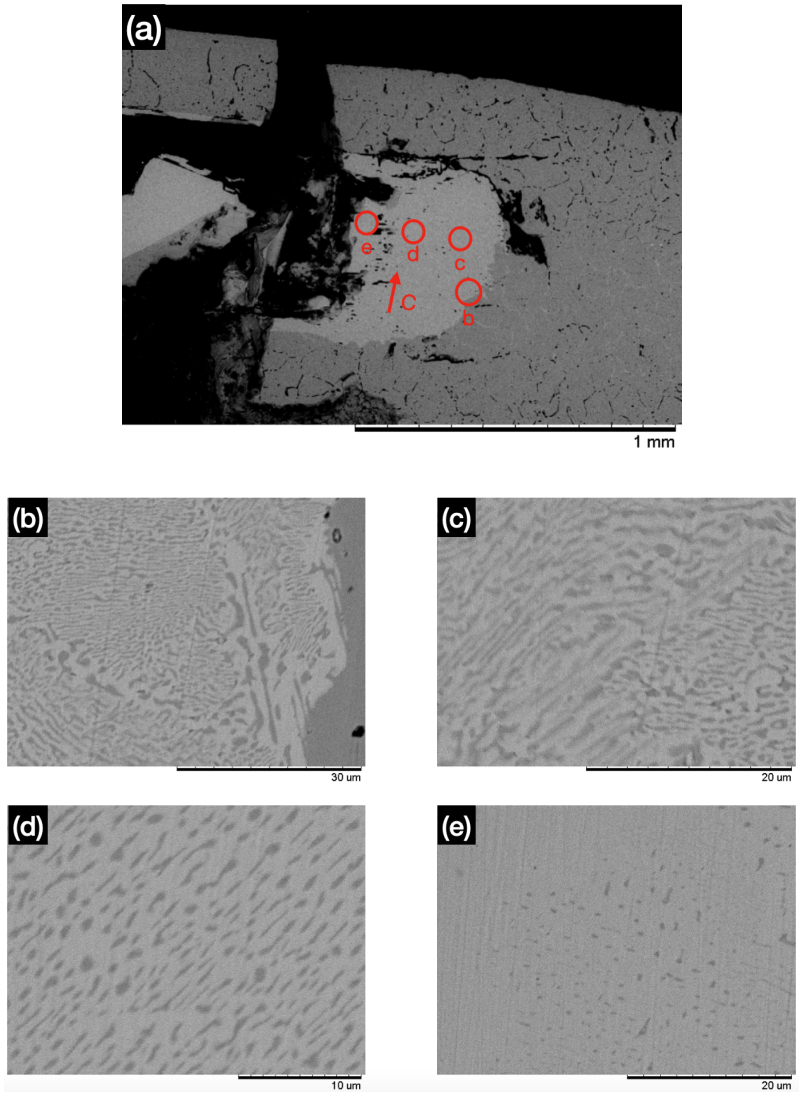

Figure 9.1: Show the outlined separated piece from the overview image 5.4a in the iron system chapter. One can clearly see spinel precipitates deep into this piece. Red circles in (a) match the image labeling.

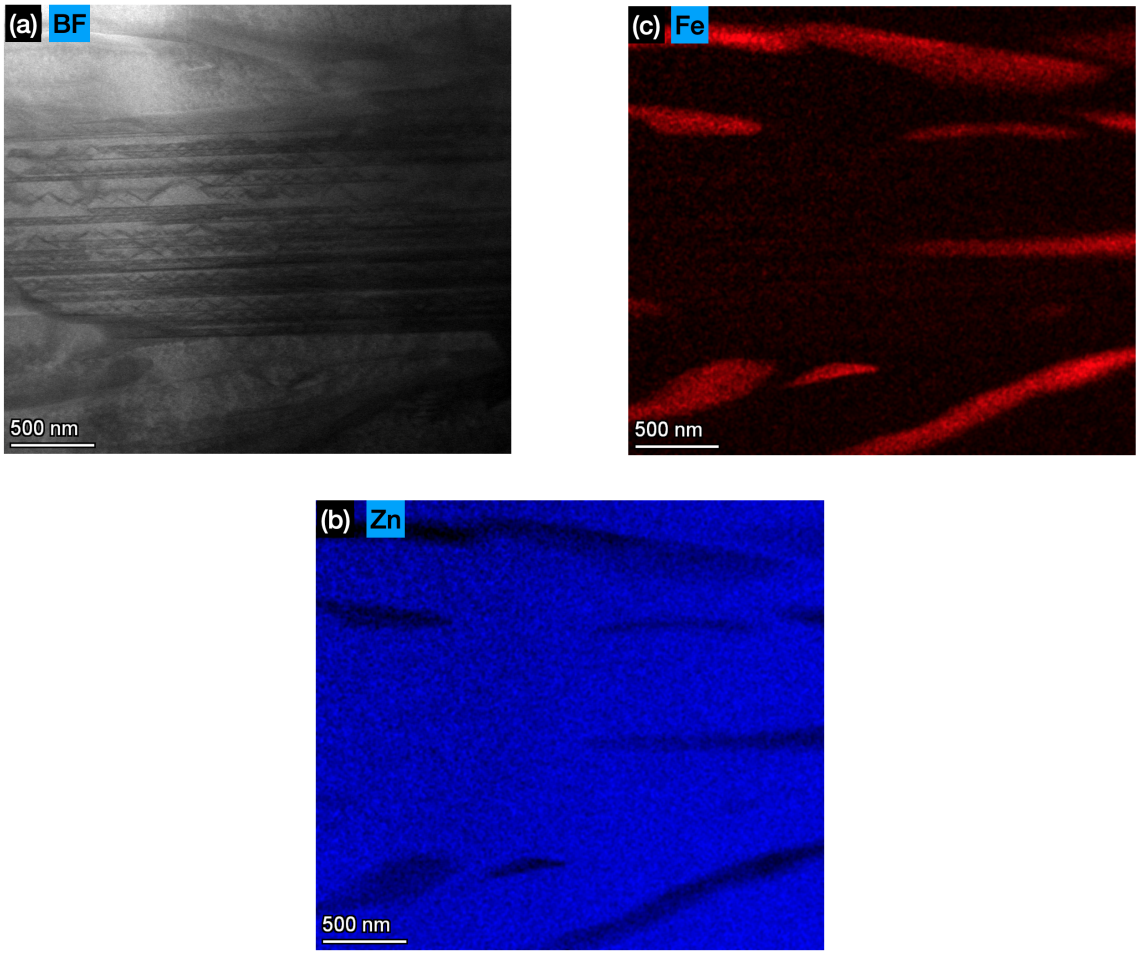

Figure 9.2: (a) Show another region from the transition between Area 2 and single crystal where spinel precipitate and IDBs are seemingly embedded. (b) and (c) show iron and zinc EDS elemental map from the corresponding area.

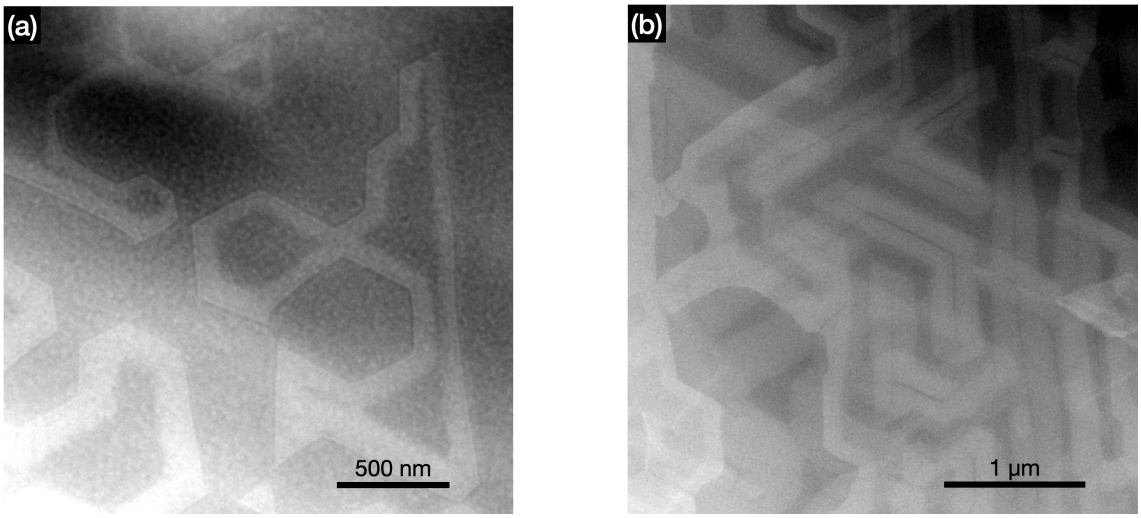

Figure 9.3: STEM ADF images of mosaic shapes on the ZnO (001) surface of DC 8 from the iron system chapter. The iron content was low in the region where the images are acquired, and iron concentration was not correlating with the contrast in the image.

Bibliography

[1] David L. Chandler. *Vast amounts of solar energy radiate to the Earth, but tapping it cost-effectively remains a challenge*. 2011. URL: `https://phys.org/news/2011-10-vast-amounts-solar-energy-earth.html` (visited on 03/03/2021).

[2] S. Agrawal, R. Rane, and S. Mukherjee. "ZnO Thin Film Deposition for TCO Application in Solar Cell". In: *Conference Papers in Energy* 2013 (2013).

[3] D.J. Rogers and F. Hosseini Teherani. "ZnO: From Transparent Conducting Oxide to Transparent Electronics". In: *Encyclopedia of Materials: Science and Technology*. 2010.

[4] William Shockley and Hans J. Queisser. "Detailed balance limit of efficiency of p-n junction solar cells". In: *Journal of Applied Physics* 32.3 (1961), pp. 510–519.

[5] C. S. Solanki and G. Beaucarne. "Advanced solar cell concepts". In: *Energy for Sustainable Development* 11.3 (2007).

[6] Andrew M. Smith and Shuming Nie. "Semiconductor nanocrystals: Structure, properties, and band gap engineering". In: *Accounts of Chemical Research* 43.2 (2010), pp. 190–200.

[7] Ephrem O. Chukwuocha, Michael C. Onyeaju, and Taylor S. T. Harry. "Theoretical Studies on the Effect of Confinement on Quantum Dots Using the Brus Equation". In: *World Journal of Condensed Matter Physics* 02.02 (2012).

[8] Ghanshyam Pilania et al. "Prediction of structure and cation ordering in an ordered normal-inverse double spinel". In: *Communications Materials* 1.1 (2020).

[9] Kristian Haug. *Functionalization of transparent conducting oxides Zinc ferrite spinel in ZnO*. Master thesis. University of Oslo, 2019.

[10] John P. Perdew. "Density functional theory and the band gap problem". In: *International Journal of Quantum Chemistry* 28.S19 (2009), pp. 497–523.

[11] Sergei A Degterov et al. *Experimental Study of Phase Equilibria and Thermodynamic Optimization of the Fe-Zn-O System*. Tech. rep.

[12] David A. Porter, Kenneth E. Easterling, and Mohamed Y. Sherif. *Phase transformations in metals and alloys, third edition*. 2009, pp. 1–59.

[13] Amy Jo Bergerud. "Phase Stability and Transformations in Vanadium Oxide Nanocrystals". PhD thesis. University of California, Berkeley, 2016.

[14] Roderick J. Hill, James R. Craig, and G. V. Gibbs. "Systematics of the spinel structure type". In: *Physics and Chemistry of Minerals* 4.4 (1979).

[15] Luis I. Granone et al. “Effect of the degree of inversion on optical properties of spinel ZnFe2O4”. In: *Physical Chemistry Chemical Physics* 20.44 (2018).

[16] Geoffrey D. Price, Sarah L. Price, and Jeremy K. Burdett. “The factors influencing cation site-preferences in spinels a new mendelyevian approach”. In: *Physics and Chemistry of Minerals* 8.2 (1982).

[17] Michal A. Borysiewicz. “ZnO as a Functional Material, a Review”. In: *Crystals* 9.10 (2019).

[18] Hadis Morkoç and Ümit Özgür. *Zinc Oxide: Fundamentals, Materials and Device Technology*. John Wiley and Sons, 2009.

[19] Martin Magnuson et al. “Electronic structure of GaN and Ga investigated by soft x-ray spectroscopy and first-principles methods”. In: *Physical Review B - Condensed Matter and Materials Physics* 81.8 (2010), p. 085125.

[20] A. Bedia et al. “Influence of the thickness on optical properties of sprayed ZnO hole-blocking layers dedicated to inverted organic solar cells”. In: *Energy Procedia*. Vol. 50. 2014.

[21] Mursal et al. “Structural and Optical Properties of Zinc Oxide (ZnO) based Thin Films Deposited by Sol-Gel Spin Coating Method”. In: *Journal of Physics: Conference Series*. Vol. 1116. 3. 2018.

[22] Gonzalo Alonso Velázquez-Nevárez et al. “Optical and electrical properties of (002)-Oriented ZnO films prepared on amorphous substrates by sol-gel spin-coating”. In: *Materials Research*. Vol. 19. 2016.

[23] Tadatsugu Minami. “New n-type transparent conducting oxides”. In: *MRS Bulletin* 25.8 (2000), pp. 38–44.

[24] S. Sadofev et al. “Growth of high-quality ZnMgO epilayers and ZnO/ZnMgO quantum well structures by radical-source molecular-beam epitaxy on sapphire”. In: *Applied Physics Letters* 87.9 (2005), p. 091903.

[25] *Available online:* URL: `https://commons.wikimedia.org/wiki/File:Wurtzite{\_}polyhedra.png` (visited on 03/23/2021).

[26] J. Geurts. “Crystal structure, chemical binding, and lattice properties”. In: *Springer Series in Materials Science*. Vol. 120. Springer Verlag, 2010, pp. 7–37.

[27] Aleksander Rečnik, Nina Daneu, and Slavko Bernik. “Nucleation and growth of basal-plane inversion boundaries in ZnO”. In: *Journal of the European Ceramic Society* 27.4 (2007).

[28] H. Schmid, E. Okunishi, and W. Mader. “Defect structures in ZnO studied by high-resolution structural and spectroscopic imaging”. In: *Ultramicroscopy* 127 (2013), pp. 76–84.

[29] Nina Daneu, Aleksander Rečnik, and Slavko Bernik. “Grain growth control in Sb2O3-doped zinc oxide”. In: *Journal of the American Ceramic Society* 86.8 (2003).

[30] Nina Daneu, Slavko Bernik, and Aleksander Renik. “Inversion boundary induced grain growth in ZnO ceramics: From atomic-scale investigations to microstructural engineering”. In: *Journal of Physics: Conference Series*. Vol. 326. 1. Institute of Physics Publishing, 2011.

[31] Gregory W. Tomlins, Jules L. Routbort, and Thomas O. Mason. "Zinc self-diffusion, electrical properties, and defect structure of undoped, single crystal zinc oxide". In: *Journal of Applied Physics* 87.1 (2000), pp. 117–123.

[32] N. Pierard et al. "Production of short carbon nanotubes with open tips by ball milling". In: *Chemical Physics Letters* 335.1-2 (2001), pp. 1–8.

[33] Takuya Tsuzuki and Paul G. McCormick. "Mechanochemical synthesis of nanoparticles". In: *Journal of Materials Science*. Vol. 39. 16-17. Springer, 2004, pp. 5143–5146.

[34] C. Tangsathitkulchai. "Acceleration of particle breakage rates in wet batch ball milling". In: *Powder Technology* 124.1-2 (2002).

[35] Lecture notes MENA 3100. *Scanning electron microscopy*. University of Oslo, 2018.

[36] Jeol Ltd. *Backscattered electron image,BSE image*. URL: `https://www.jeol.co.jp/en/words/semterms/search{\_}result.html?keyword=BSEimage` (visited on 03/26/2021).

[37] David B. Williams and C. Barry Carter. *Transmission electron microscopy: A textbook for materials science*. Springer US, 2009, p. 153.

[38] Shengqiang Zhou et al. "Fe-implanted ZnO: Magnetic precipitates versus dilution". In: *Journal of Applied Physics* 103.2 (2008).

[39] R. Hansson, P. C. Hayes, and E. Jak. "Phase equilibria in the Fe-Zn-O system at conditions relevant to zinc sintering and smelting". In: *Transactions of the Institutions of Mining and Metallurgy, Section C: Mineral Processing and Extractive Metallurgy*. Vol. 114. 3. Taylor & Francis, 2005.

[40] Shengqiang Zhou et al. "Crystallographically oriented magnetic ZnFe2O4 nanoparticles synthesized by Fe implantation into ZnO". In: *Journal of Physics D: Applied Physics* 40.4 (2007), pp. 964–969.

[41] F. Bræstrup, B. C. Hauback, and K. K. Hansen. "Temperature dependence of the cation distribution in ZnFe2 O4 measured with high temperature neutron diffraction". In: *Journal of Solid State Chemistry* 181.9 (2008), pp. 2364–2369.

[42] Doosoo Kim et al. "Formation and behavior of Kirkendall voids within intermetallic layers of solder joints". In: *Journal of Materials Science: Materials in Electronics* 22.7 (2011), pp. 703–716.

[43] T. Yamashita, R. Hansson, and P. C. Hayes. "The relationships between microstructure and crystal structure in zincite solid solutions". In: *Journal of Materials Science* 41.17 (2006), pp. 5559–5568.

[44] *The periodic table of the elements by WebElements*. URL: `https://www.webelements.com/` (visited on 04/05/2021).

[45] Minerals.net. *The spinel mineral series*. URL: `https://www.minerals.net/mineral/spinel.aspx` (visited on 03/17/2021).

[46] Tetsuya Senda and Richard C. Bradt. "Grain Growth of Zinc Oxide During the Sintering of Zinc Oxide—Antimony Oxide Ceramics". In: *Journal of the American Ceramic Society* 74.6 (1991).

[47] Aleksander Rečnik et al. “Structure and Chemistry of Basal-Plane Inversion Boundaries in Antimony Oxide-Doped Zinc Oxide”. In: *Journal of the American Ceramic Society* 84.11 (2001), pp. 2657–2668.

[48] Koji Kuramochi et al. “Quantitative structural analysis of twin boundary in α - Zn7 Sb2 O12 using HAADF STEM method”. In: *Ultramicroscopy* 109.1 (2008), pp. 96–103.

[49] Gabrielle C. Miles and Anthony R. West. “Polymorphism and thermodynamic stability of Zn7Sb 2O12”. In: *Journal of the American Ceramic Society* 88.2 (2005).

[50] D. S. Gouveia et al. “Color and structural analysis of CoxZn7-xSb2O12 pigments”. In: *Materials Research Bulletin* 41.11 (2006).

[51] E. Gutierrez Puebla et al. “Crystal growth and structure of diantimony(III) zinc oxide.” In: *Acta Crystallographica* B38.Part 7 (1982).

[52] Y. Ohno et al. “Optical properties of dislocations in wurtzite ZnO single crystals introduced at elevated temperatures”. In: *Journal of Applied Physics* 104.7 (2008), p. 073515.

[53] M. Kurzawa et al. “Reinvestigation of phase equilibria in the V2O5-ZnO system”. In: *Journal of Thermal Analysis and Calorimetry* 64.3 (2001).

[54] Hakan Çolak and Orhan Türkoğlu. “Structural and electrical properties of V-doped Zno prepared by the solid state reaction”. In: *Journal of Materials Science: Materials in Electronics* 23.9 (2012).

[55] I. Rychlowska-Himmel and A. Blonska-Tabero. “Synthesis and thermal stability of Zn4V2O9”. In: *Journal of Thermal Analysis and Calorimetry* 64.3 (2001), pp. 1121–1125.

[56] M. C. Schubert et al. “Modeling distribution and impact of efficiency limiting metallic impurities in silicon solar cells”. In: *Conference Record of the IEEE Photovoltaic Specialists Conference*. 2012, pp. 286–291.